Università degli Studi di Padova
Doctoral School of Physics
CYCLE XXIV 2009 - 2011

Plasmonic Nanostructures for Enhanced Photovoltaics

by
Gabriele Zacco

Under the supervision of
Prof. Filippo Romanato

UNIVERSITÀ
DEGLI STUDI
DI PADOVA

Università degli Studi di Padova

Consiglio Nazionale delle Ricerche - Istituto Officina dei Materiali

Dipartimento di Fisica "Galileo Galilei"

SCUOLA DI DOTTORATO DI RICERCA IN FISICA - CICLO XXIV°

Plasmonic Nanostructures for Enhanced Photovoltaics

Direttore della Scuola : Ch.mo Prof. Andrea Vitturi

Supervisore : Ch.mo Prof. Filippo Romanato

Dottorando : Gabriele Zacco

to my family

Abstract

The aim of this work is to investigate the role of optical resonances supported in different layouts of solar cells integrating metallic plasmonic gratings. A simplified ideal model was first developed in order to clarify the role and the potentialities that all the optical resonances involved in such structures have in remodulating light absorption. In a further analysis, a global optimization of both geometrical parameters of the grating (period, thickness, slit width) as well as the dielectric environment has been performed, considering different solar cell layouts, in order to obtain a gain in absorption over the widest bandwidth of solar spectrum. Following the simulation and optimization results, a nanofabrication process for the integration of metal nanostructures on top of large area c-Si solar cells has been designed. A new Laser Interference Lithography system, useful for the fabrication of large area plasmonic structures has been designed, constructed and tested. Several processes have been designed and performed and new materials have been also developed (e.g. Hybrid Organic-Inorganic solgel sinusoidal gratings). System performances are still growing toward the control of the full set of geometric parameters of the structures that can be fabricated. After nanofabrication, performances of solar cells integrating plasmonic crystals have been verified by electro-optic characterizations. Polarization resolved Specular Reflectance measurements of patterned solar cell samples were performed and results validate the model. Figures of merit of devices integrating plasmonic crystals, current density (JV) as well as External Quantum Efficiency (EQE), have been also measured. *JV* characteristics show a significant improvement in conversion efficiency for cells integrating the Ag nanostructures compared to flat reference cells. *Such improvement is mainly due to the enhancement in short circuit current due to the light trapping effect provided by the plasmonic crystals.* The EQE spectra of cells with gratings show an enhancement in near infra-red response for TM polarization, as expected from optical simulations, and also an unexpected measured improved absorption in the visible. The latter is a further indication of effectiveness of plasmonic nanostructures in light harvesting.

Sommario

Negli ultimi anni, la comunità scientifica ha largamente riconosciuto la possibilità di impiegare i fenomeni legati alle risonanze plasmoniche nei metalli, sfruttandone le particolari caratteristiche per il miglioramento delle performance di dispositivi optoelettronici. Tali soluzioni sono spesso ampiamente vantaggiose, ad esempio nel campo della sensoristica, in termini di miglioramento dell'efficienza nella rivelazione di specie chimiche e biologiche. Un altro campo di crescente attenzione è l'applicazione delle plasmonica al fotovoltaico. In tal caso, la capacità dei reticoli plasmonici di rimodulare lo spettro della radiazione solare incidente consente di migliorare l'efficienza di conversione energetica.

In questo contesto si colloca questo lavoro, incentrato nel corso di questi tre anni, nello studio, nella realizzazione e nella caratterizzazione di reticoli plasmonici con l'intento di integrarli in dispositivi più complessi, come le celle fotovoltaiche a silicio cristallino.

In primo luogo, si è proceduto sviluppando un modello semplificato di reticolo metallico, posto al di sopra di uno strato semi-infinito di silicio, al fine di chiarire il ruolo e le potenzialità delle risonanze ottiche che si generano quando il dispositivo viene irradiato dall'alto da una sorgente monocromatica polarizzata.

Successivamente, è stata condotta una ulteriore analisi di ottimizzazione globale dei parametri geometrici e dei materiali su diverse configurazioni di celle solari, al fine di individuare le caratteristiche tecniche migliori che garantissero un guadagno in assorbimento, integrato sulla più ampia porzione di spettro solare.

Le fasi di simulazione e ottimizzazione sono state infine seguite dal design di un processo di nanofabbricazione che permettesse l'integrazione delle nanostrutture metalliche ottimizzate su celle solari a silicio cristallino. Parte del lavoro è stato mirato alla progettazione e realizzazione di un sistema di litografia per la nanofabbricazione di reticoli plasmonici su grandi aree, chiamato Litografia Interferenziale che, dai primi mesi del 2010 è operativo presso l'Istituto IOM – CNR di Trieste. Mediante l'utilizzo di questa tecnica sono stati messi a punto diversi processi di nanofabbricazione, tra i quali quello per la realizzazione di reticoli con profilo sinusoidale e la loro integrazione in un biosensore per la rivelazione di DNA e lo studio delle potenzialità in termini litografici di materiali di tipo solgel ibridi organici\inorganici. Il processo per la realizzazione dei reticoli sulle celle solari è stato messo a punto e i campioni realizzati sono stati analizzati mediante misure morfologiche (SEM, AFM) e ottiche.

Infine, le celle solari ottenute sono state caratterizzate mediante le misure delle principali figure di merito, tra cui le caratteristiche di densità di corrente-tensione (JV) e l'efficienza quantica esterna (EQE). Dalle misure JV è stato riscontrato un significativo aumento di efficienza per le celle integranti i reticoli plasmonici, in confronto a quelle convenzionali usate come riferimento, principalmente dovuto all'aumento della densità di corrente di corto circuito. Gli spettri di EQE mostrano un aumento nella regione del vicino infrarosso, per luce incidente polarizzata in modo tale da eccitare anche risonanze plasmoniche, come atteso dai risultati del modello sviluppato.

I risultati raggiunti e presentati in questa tesi dimostrano l'effettiva possibilità dell'uso di nanostrutture metalliche per il rimodulazione e altresì il controllo del fenomeno di assorbimento della luce all'interno delle celle fotovoltaiche a silicio cristallino. I risultati soddisfano ampiamente le ipotesi in quanto aprono una nuova frontiera per l'applicazione anche ad altri tipologie di celle quali ad esempio quelle a film sottile o organiche. In tali dispositivi, infatti, la riduzione del materiale assorbente, al fine di massimizzare la raccolta della carica e di ridurre i costi, rende di primaria importanza la ricerca di queste nuove soluzioni per il miglioramento dell'assorbimento della luce. La direzione verso cui si stanno concentrando enormi sforzi di ricerca negli ultimi anni è quella della realizzazione di dispositivi "spessi dal punto di vista della luce incidente e sottili per la raccolta della carica generata".

Index

Abstract 7
Sommario 8
Introduction 15
1 Surface Plasmon Resonances 19
1.1 Introduction 19
1.2 Basic theory: Maxwell's equations 20
1.3 SPPs dispersion relation 22
1.4 Spatial extension and propagation lengths of SPPs 25
1.5 Multilayer systems 28
1.6 Long-Range and Short-Range Surface Plasmons 29
1.7 Excitation of SPPs by Light 29
1.7.1 Prism Coupling 29
1.7.2 Grating Coupling 31
2 Plasmonic enhanced Photovoltaics 33
2.1 Introduction 33
2.2 Principles of Photovoltaics 33
2.2.1 Solar Radiation 34
2.2.2 Ideal solar cell model 35
2.2.3 Principles of Solar Cells Physics 37
2.3 Plasmonics for Photovoltaics 50
2.3.1 Plasmonic enhanced solar cell design solutions 50
2.3.2 Light trapping using SPPs. 51
2.3.3 Incidence on solar cell performances 52
3 Laser Interference Lithography 53
3.1 Introduction to IL 53
3.2 Basic Theory of LIL 54
3.2.1 Electromagnetic waves formalism 54
3.2.2 Superposition - interference 56
3.2.3 Periodicity of Interference Fringes 58
3.2.4 Visibility of interference fringes 59
3.2.5 Polarization 60

3.2.6 Coherence 62
3.2.7 Partial coherence and fringe visibility 64
3.3 Laser Interference Lithography Systems 64
3.4 Plasmonic gratings nanofabrication processes by means of LIL 68
3.4.1 Fabrication of sinusoidal plasmonic gratings 68
3.4.2 Development of HOI Solgel based Photoresist for LIL 75
4 Absorption profile modulation by means of 1D digital plasmonic gratings 81
4.1 Introduction 81
4.2 Finite Elements model setup 81
4.3 Modal analysis of the 1D digital grating 83
4.4 Optical resonances 84
4.4.1 Cavity Mode (CM) resonances 84
4.4.2 Surface Plasmon Polariton (SPP) resonances 84
4.4.3 Wood-Rayleigh anomalies (WR) 84
4.5 Simulation Results 85
4.5.1 CM excitation 86
4.5.2 Coupled CM-SPP excitation 86
4.5.3 Coupled CM-WR excitation 87
4.5.4 The absorption profile extinction length (L) evaluation 88
4.5.5 Incidence of the gratings duty cycle 89
5 Digital 1D plasmonic gratings on bulk solar cells 91
5.1 Introduction to the ORION project 91
5.2 Optical simulation 91
5.3 Nanofabrication of plasmonic crystal on bulk solar cells 94
5.3.1 Batches of solar cells for plasmonic crystals integration 94
5.3.2 General description of the flow chart 95
5.3.3 Resist tri-layer 96
5.3.4 LIL exposures 97
5.3.5 Hard Mask evaporation and lift off 98
5.3.6 Active area definition 99
5.3.7 Dry etching 99
5.3.8 Silver evaporation and lift off 100
5.3.9 Gratings on textured solar cells 102
5.4 Characterization of solar cells integrating plasmonic crystals 104

5.4.1 Spectroscopic ellipsometry characterization 104
5.4.2 Electro-optical characterization setups 104
5.4.3 Dark and illuminated current-voltage characteristics 106
5.4.4 External Quantum Efficiency 110
Conclusions 115
References 119

Introduction

The idea of preventing the most severe impacts of climate change by drastically cutting our emissions of carbon dioxide is largely shared all over the world. This process received a strong acceleration after the agreement on the two United Nations climate treaties, the UN Framework Convention on Climate Change (UNFCCC) in 1992 and the Kyoto Protocol in 1997. Since the agreement of Kyoto Protocol, the European Union have aimed to reduce CO_2 emissions in the 2008-2012 period to 8% below 1990 levels. Furthermore, in 2007 EU leaders signed a unilateral commitment that Europe would cut its emissions by at least 20% of 1990 levels by 2020. However, although the present world economic crisis and future economic prospects remain still dramatic in the mid-term, global primary energy demand increases fast, pushing CO_2 emissions to even new high levels (a future scenario of an increase of world demand for energy by one-third is forecast until 2035[1]).

In this context, renewable energies have to play the important role of balancing the energy demand growth and to make the world energy consumption more sustainable. Although renewable energy is a relatively small portion of total energy supply, the installed global renewable energy capacity has more than quadrupled between 2000 and 2010[2]. In particular, looking at the Photovoltaic (PV) energy production, recent studies states that solar energy electricity generation has grown by a factor of over 5 for the last ten years. Global installed PV capacity increased by 16.6 GW in 2010, a 131% increase respect to the year before and nearly seven times the amount (2.4 GW) that was installed in 2007. For example, in Italy the cumulative PV installed capacity until 2011 is estimated to 3.5 GW against 17 GW in Germany, 2.5 GW in U.S.A and 3.6GW in Japan[2], [3].

Beyond the widespread development of PV, one of the future challenges is to make electricity from solar cells more and more competitive with fossil fuel technologies toward the so called grid parity. Grid parity is the point at which alternative means of generating electricity produces power at a cost that is equal to or less than the price of purchasing power from the grid. Thus solar cell performances must be enhanced and price needs to be even more reduced.

Currently, two categories of PV cells are used in most of today's commercial PV modules: crystalline Silicon (c-Si) and thin-film. The c-Si category, also called first-generation PV, includes mono-crystalline and multi-crystalline PV cells accounted for about 90% of PV produced in 2010. The efficiencies of all PV cell types have improved over the past decades. One of the last highest-efficiency cell result was achieved in 2010 in a multi-junction concentrator at 42.3% efficiency. Other research cell efficiencies range are: from 15% to 25% for crystalline silicon cells, 10% to 20% for thin film, and about 5% to 10% for the emerging PV technologies organic cells and dye-sensitized cells.

At present, most of the price of conventional c-Si solar cells is due to the cost of silicon wafers. Therefore, there is a great interest in reducing absorber material thicknesses toward thin-film devices with thickness in the range of 1μm. However, a limitation in

all thin-film solar-cell technologies is that the device thickness is lower than the absorption depth of photons over a broad wavelength range. Therefore, structuring thin-film solar cells so that light is trapped inside, in order to increase the absorbance, is a promising challenge.

Existing light trapping methods applied to wafer-based devices are achieved by texturing the device surface. Such surface corrugation allows to scatter incoming photons into the solar cell over a large angular range, thus increasing the effective path length in the cell. However, this technique is not suitable for thin-film cells since the surface roughness would exceed the film thickness and because the greater surface area would increase minority carrier recombination in the surface and junction regions.

In order to overcome the problem of absorption, a new method for achieving light trapping is the use of metallic nanostructures that support Surface Plasmons[35]. Plasmonic resonances can be excited allowing light to be guided and concentrated in the active part of the cell. Thus, solar cell designers have now the possibility to create enhanced devices that are thick from the point of view of photons and thin for electrons, towards the near-complete light absorption and maximum photocarrier current collection. Furthermore, plasmonic enhanced photovoltaic devices could be designed to depend weakly on frequency, polarization and angle of incidence thus improving the overall performance.

A particular example is that of c-Si solar cells. They are optimized in order to maximize their spectral response over the entire solar spectrum. However, there is a certain amount of energy lost, corresponding to the near infrared portion of the solar spectrum, close to the silicon bandgap, for which the absorption length is comparable or even longer than the device thickness. Metallic nanostructures could be used to overcome the problem since they feature high scattering cross section and are able to re-distribute the electromagnetic power and reduce the effective absorption depth inside the cell. Thus, the aim is to deal with the possibility to employ plasmonic nanostructures to remodulate the absorption profile distribution, decreasing the surface reflection and confining the radiation.

The investigation of plasmonic resonances of metallic nanostructures integrated on different cell layouts are therefore the main focus of the thesis. Firstly, a model of solar cell integrating plasmonic crystals has been investigated to clarify the role and the potentialities that the optical resonances of such structures have in remodulating light absorption. Three main optical features play a relevant role: Surface Plasmon Polariton (SPP) resonances, Cavity Mode (CM) resonances and Wood Rayleigh anomalies (WR). Coupling of these three features was found to be useful to enhance absorption in silicon within different depths, in the NIR part of the spectrum. In particular CM-WR coupling was demonstrated to produce a relevant IR-enhancement, since the grating has both antireflection properties and spreads light at grazing angles, incrementing the optical path length in silicon. In a further analysis, a global optimization of both geometrical parameters of the grating (period, thickness, slit width) and the dielectric environment has been performed. Different solar cell layouts have been considered in order to obtain a gain in absorption over the widest possible bandwidth of solar spectrum.

Following the simulation and optimization results, the design of a nanofabrication process for the integration of metal nanostructures on top of large area c-Si solar cells has been developed. The technique used to create these highly regular large area structures is Laser Interference Lithography (LIL) in combination with dry etching and metal evaporation in vacuum. In particular, LIL is a nanofabrication technique which employs interference fringes coming from two or more laser wavefronts to impress regular light intensity distributions on photo-sensitive substrates. The installation and assessment of a new LIL system that I have set-up at IOM-CNR in Trieste is discussed hereafter. This nanofabrication setup, is working since the first months of 2010 in our laboratory at IOM-CNR in Trieste. System performances are still growing toward the control of the full set of geometric parameters of the structures that can be fabricated. Several processes have been designed and tested and new materials (based on Hybrid Organic-Inorganic solgel) have been also developed. Fabrication results are shown in the last chapter of the thesis.

Finally, fabricated samples have been tested by electro-optic characterizations. Polarization resolved Specular Reflectance measurements of patterned solar cell samples were performed and the results validate the model. Solar cell JV figures of merit as well as External Quantum Efficiency (EQE) of devices integrating plasmonic crystals have been also measured.

In conclusion, this work aims to show how to employ the physics phenomena of plasmonics in order to take control of light absorption inside solar cells. The processes of modeling, design, fabrication and characterization of such structures have been fully explained. Basically, plasmonics allows to match two apparently opposite requirements: the realization of active layers that are seen as very thick from the photons and, at the same time, as very thin from the electrons, i.e. having both an almost-complete light absorption and the maximum photocarrier current collection. If this results is important in the bulk c-Si solar , it is even more important for the development of the thin film organic cells where the problem of lack of absorption is central.

1 Surface Plasmon Resonances

1.1 Introduction

In principle, Surface Plasmons Polaritons (SPPs) resonance occurs when an incident electromagnetic wave excites a collective oscillation of free electrons at the interface between two media with opposite signs of real part of the dielectric constant (i.e. a metal and a dielectric). The coupling between the incident electromagnetic fields with the oscillations of the conductor's electron plasma generate a propagating surface wave evanescently confined in the perpendicular direction[4], [5].

SPPs are solutions of Maxwell's equations bound to a surface: they exhibit a significant field confinement next to the interface, decaying exponentially from the surface with an extension length of the same order of the wavelength inside the dielectric and almost one order of magnitude shorter in the metal. This confinement leads to an enhancement of the fields at the interface and makes SPPs extremely sensitive to optical and geometrical characteristics of the surface such as profile, shape, roughness and refractive indices of the facing media.

The first theoretical formalization of these surface waves was introduced in the early 20^{th} Century in the context of radio waves propagating along the surface of a conductor of finite conductivity by Sommerfeld[6] in 1899, and Zenneck[7] in 1907. In the visible domain, the first observation of Surface Plasmon Polaritons as *anomalous* intensity drops in spectra produced when visible light reflects at metallic gratings was made by Wood[8] in 1902. However, only Fano[9] in 1941 connected Wood's results with the earlier theoretical work by demonstrating that these anomalies are associated with the excitation of electromagnetic surface waves on the surface of the diffraction grating. Around this years, loss phenomena associated with interactions taking place at metallic surfaces were also found via the diffraction of electron beams at thin metallic foils by Ritchie[10] in 1957. In the 1960s these results were then linked with the original work on diffraction gratings in the optical domain[11]. In 1968, a method of excitation of Sommerfeld's surface waves with visible light using prism coupling has been demonstrated by Otto[12] and Kretschmann and Raether[13]. A unified description of all these phenomena of SPPs excitation was then established by Cowan and Arakawa[14] in 1970. Recently, research discoveries in the microwave and the terahertz domain have taken place closing the circle with the original works.

These pioneering works established a convenient method for the excitation and investigation of surface polaritons before the advent of modern nanofabrication techniques that now allows the production of subwavelength diffraction gratings. Since SPPs have a non-radiative nature, the surface plasma wave cannot be excited directly by an incoming light wave, because of momentum mismatch. Therefore any SPR demonstrator needs a light coupler that allows to reach that matching condition. This momentum adjustment could be basically achieved by using attenuated total reflection in prism couplers and diffraction at the surface of gratings. Prism Coupling SPR (PCSPR) excitation method, demonstrated by Kretschmann, exploits a prism in order to

increase incident light momentum and realize SPP optical excitation. However, this configuration is not so useful since it suffers from the weighty prism alignment and it is not suitable to miniaturization and integration. A more practical and cheaper solution consists in grating coupling SPR (GCSPR), wherein a metal surface is modulated by a one-dimensional periodic pattern. Here, a plane-wave illuminating the surface is diffracted and it is possible for one of the diffracted order to couple with SPP modes of the surface. As stated above, the plasmonic behavior of such corrugated metal surfaces has been connected with Wood's anomalies and surface plasmons by the work of Cowan and Arakawa[14]. Their strong compatibility with mass production makes these grating couplers extremely attractive for fabrication of SPR devices.
The following chapter will outline the main basic framework of SPPs. Starting from Maxwell's equations, the SPPs dispersion which shows the typical non-radiative character of these surface waves and their evanescent nature was then derived together with their surface propagation characteristics.

1.2 Basic theory: Maxwell's equations

Surface plasmons polaritons resonances can be found looking for a wavelike solution of Maxwell's equations confined at the interface of two semi-infinite media by imposing the proper boundary conditions. In the absence of free charges and currents, the constitutive relations are:

$$\boldsymbol{D} = \varepsilon \boldsymbol{E} \tag{1.1}$$

$$\boldsymbol{B} = \mu \boldsymbol{H} \tag{1.2}$$

where $\varepsilon = \varepsilon_0 \varepsilon_r$ and $\mu = \mu_0 \mu_r$, ε_r and μ_r are respectively the relative dielectric permittivity and the relative magnetic permeability of the medium, ε_0 and μ_0 are dielectric permittivity and magnetic permeability in vacuum.
The well known Maxwell's equations to solve are:

$$\nabla \cdot \boldsymbol{D} = 0 \tag{1.3}$$

$$\nabla \times \boldsymbol{E} = -\frac{\partial \boldsymbol{B}}{\partial t} \tag{1.4}$$

$$\nabla \cdot \boldsymbol{B} = 0 \tag{1.5}$$

$$\nabla \times \boldsymbol{H} = -\frac{\partial \boldsymbol{D}}{\partial t} \tag{1.6}$$

Let us consider a set of time-varying harmonic plane waves as solution of Maxwell's equation in the high frequency regime. Therefore, the fields can be written in the form:

$$\begin{aligned} \boldsymbol{E}(x,y,z,t) &= \mathbf{E}(x,y,z)e^{i\omega t} \\ \boldsymbol{H}(x,y,z,t) &= \mathbf{H}(x,y,z)e^{i\omega t} \end{aligned} \tag{1.7}$$

Substituting eq.s 1.1, 1.2 and 1.7 into 1.4 and 1.6 a unique formulation for the magnetic field can be derived:

$$\nabla \times (\varepsilon_r^{-1} \nabla \times \boldsymbol{H}) - k_0^2 \boldsymbol{H} = 0 \qquad 1.8$$

where we considered only non magnetic materials, so that $\mu_r = 1$, and defined $k_0 = \omega/c$.
Equation 1.8 is typically solved separately in regions of constant ε_r and the solutions obtained have to be matched using appropriate boundary conditions. Within each of these regions using some vector identities, the equation simplifies in

$$\nabla^2 \boldsymbol{H} + k_0^2 \varepsilon_r \boldsymbol{H} = 0 \qquad 1.9$$

which is known as *Helmholtz equation*.
Let now consider the particular case in which the wave propagates along the x-direction of the Cartesian coordinate system shown in Fig. 1.1, where z = 0 coincides with the interface sustaining the propagating wave. Due to the continuous translational symmetry along the y-direction, the field of the propagating wave is invariant along the y-direction and can be rewritten as

$$\boldsymbol{H}(x, y, z) = \mathbf{H}(z) e^{i k_x x} \qquad 1.10$$

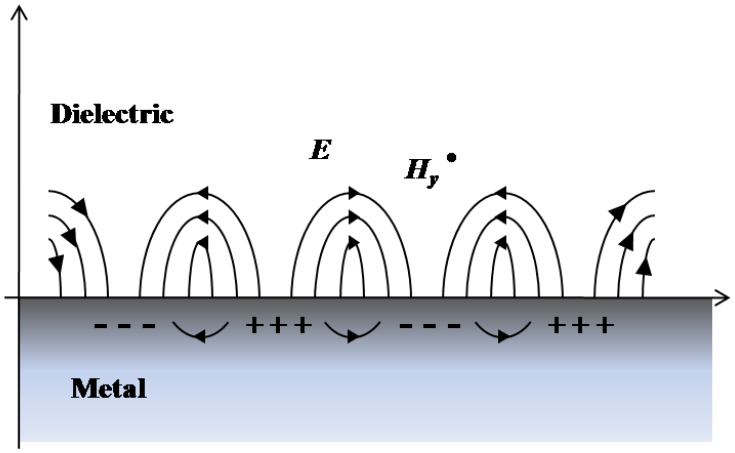

Fig. 1.1: excited SPPs at the interface between a metal and a dielectric. The figure shows the coupling between the electromagnetic wave and surface charge[15].

where k_x, called *propagation constant,* is the component of the wavevector along the direction of propagation. Inserting equation 1.10 in 1.9 we obtain:

$$\frac{\partial^2 \boldsymbol{H}(z)}{\partial z^2} + (k_0^2 \varepsilon_r - k_x) \boldsymbol{H}(z) = 0 \qquad 1.11$$

This equation, together with the similar one for the electric field $\boldsymbol{E}$, is the starting point for the study of guided electromagnetic modes in waveguides, and more specifically for the analysis of dispersion relation of SPP.

1.3 SPPs dispersion relation

The main characteristics of surface plasmons polaritons can be found considering an ideal system consisting of a dielectric material characterized by an isotropic complex relative dielectric constant $\varepsilon_2 = \varepsilon_2^{'} + i\varepsilon_2^{''}$ in the half space z > 0 , and a metal described by an isotropic, frequency-dependent, complex dielectric function $\varepsilon_1(\omega) = \varepsilon_1^{'} + i\varepsilon_1^{''}$ in z < 0. The metallic character of medium 1 requires further that $Re[\varepsilon_1] < 0$, therefore $\varepsilon_1^{'} < 0$, for metals this condition is fulfilled at frequencies below the bulk plasmon frequency ω_p. By contrast, the insulator character of medium 2 requires $\varepsilon_2^{'} > 0$.

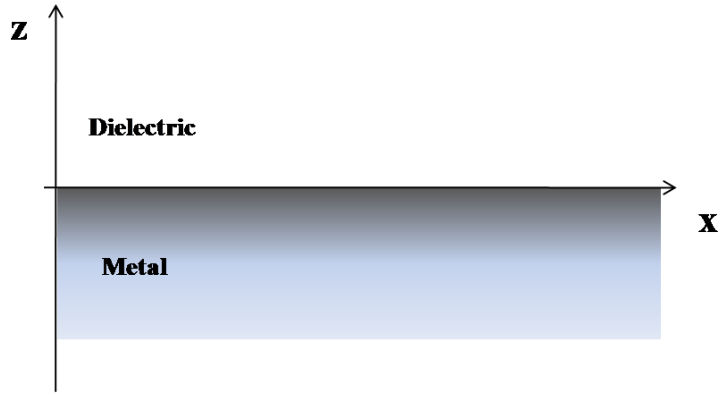

Fig. 1.2: geometry for SPP propagation at a single metal\dielectric interface.

As a consequence of Maxwell's equations, fields have to obey to the following boundary conditions at the interface

$$\begin{aligned} \boldsymbol{n} \cdot (\boldsymbol{D}_1 - \boldsymbol{D_2}) &= 0 \\ \boldsymbol{n} \times (\boldsymbol{E}_1 - \boldsymbol{E_2}) &= 0 \\ \boldsymbol{n} \cdot (\boldsymbol{B}_1 - \boldsymbol{B_2}) &= 0 \\ \boldsymbol{n} \times (\boldsymbol{H}_1 - \boldsymbol{H_2}) &= 0 \end{aligned} \qquad 1.12$$

where **n** is the versor normal to the surface. As a consequence of these relations the electric field tangential component $\boldsymbol{E}_{\parallel}$ is continuous while the normal one is not, since it is the normal displacement vector component $\boldsymbol{D}_{\perp}$ that must be continuous.
Thus we have:

$$\begin{aligned} \boldsymbol{E}_{1,\parallel} &= \boldsymbol{E}_{2,\parallel} \\ \varepsilon_1 \boldsymbol{E}_{1,\perp} &= \varepsilon_2 \boldsymbol{E}_{2,\perp} \\ \boldsymbol{H}_{1,\parallel} &= \boldsymbol{H}_{2,\parallel} \\ \mu_1 \boldsymbol{H}_{1,\perp} &= \mu_2 \boldsymbol{H}_{2,\perp} \end{aligned} \qquad 1.13$$

Let us now consider two independent solutions of Maxwell's equations TM and TE polarized. We want to look for propagating wave solutions confined to the interface, i.e. with evanescent decay in the perpendicular z-direction.
The guess field evaluated for TM modes is in the form:

for z $>$ 0
(dielectric - medium #2)

$$\boldsymbol{H}_2 = \left(0, H_{2,y,}, 0\right)e^{i(k_{2,x}x + k_{2,z}z - \omega t)}$$
$$\boldsymbol{E}_2 = \left(E_{2,x}, 0, E_{2,z}\right)e^{i(k_{2,x}x + k_{2,z}z - \omega t)} \qquad 1.14$$

for z $<$ 0
(metal - medium #1)

$$\boldsymbol{H}_1 = \left(0, H_{1,y}, 0\right)e^{i(k_{1,x}x - k_{1,z}z - \omega t)}$$
$$\boldsymbol{E}_1 = \left(E_{1,x}, 0, E_{1,z}\right)e^{i(k_{1,x}x - k_{1,z}z - \omega t)} \qquad 1.15$$

If we further assume that k_z is purely imaginary, we can obtain surface waves characterized by an exponentially decaying behavior in the z direction both on the z > 0 and z < 0 half spaces. Applying the boundary conditions 1.13 then follows:

$$k_{1,x} = k_{2,x} \equiv k_x \qquad 1.16$$

Now let us test if eq.s 1.14 and 1.15 are solutions of the Maxwell's equations calculating the curl and noting that the expressions are synthesized by the notation j=1,2 respectively for z $<$ 0 and z $>$ 0:

$$\nabla \times \boldsymbol{H} = \begin{pmatrix} \mp H_{j,y} i k_{j,z} \exp i\left(k_x x \pm k_{j,z} z - \omega t\right) \\ 0 \\ H_{j,y} i k_x \exp i\left(k_x x \pm k_{j,z} z - \omega t\right) \end{pmatrix} \qquad 1.17$$

and

$$\varepsilon_j \frac{\partial \boldsymbol{E_j}}{\partial t} = \begin{pmatrix} -i\varepsilon_j \omega E_{j,x} \exp i\left(k_x x \pm k_{j,z} z - \omega t\right) \\ 0 \\ -i\varepsilon_j \omega E_{j,z} \exp i\left(k_x x \pm k_{j,z} z - \omega t\right) \end{pmatrix} \qquad 1.18$$

Considering first the x- components 1.17 and 1.18 in eq. 1.6, results:

$$\mp H_{j,y} i k_{j,z} \exp i\left(k_x x \pm k_{j,z} z - \omega t\right) = -i\varepsilon_j \omega E_{j,x} \exp i\left(k_x x \pm k_{j,z} z - \omega t\right) \qquad 1.19$$

then
for z $>$ 0
(dielectric - medium #2)

$$\frac{k_{2,z}}{\varepsilon_2} H_{2,y} = -\omega E_{2,x} \qquad 1.20$$

and

for z $<$ 0
(metal - medium #1)

$$\frac{k_{1,z}}{\varepsilon_1} H_{1,y} = \omega E_{1,x} \qquad 1.21$$

Applying now the boundary conditions 1.13:

$$\begin{cases} \frac{k_{1,z}}{\varepsilon_1} H_{1,y} + \frac{k_{2,z}}{\varepsilon_2} H_{2,y} = 0 \\ H_{1,y} = H_{2,y} \end{cases} \quad 1.22$$

which admits solution only if the determinant vanishes, i.e.

$$\frac{k_{1,z}}{\varepsilon_1} + \frac{k_{2,z}}{\varepsilon_2} = 0 \quad 1.23$$

and applying the *Helmholtz equation* 1.11:

$$k_{j,z}^2 + k_x^2 = \varepsilon_j \left(\frac{\omega}{c}\right)^2 \quad 1.24$$

Together 1.23and 1.24 determines the SPPs dispersion Relation:

$$k_x = \frac{\omega}{c} \sqrt{\frac{\varepsilon_1 \varepsilon_2}{\varepsilon_1 + \varepsilon_2}} \quad 1.25$$

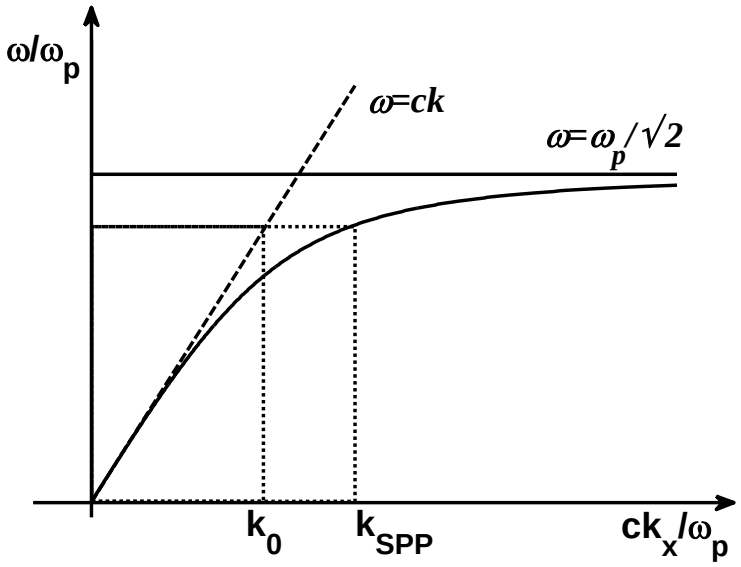

Fig. 1.3: SPP dispersion curve for a non absorbing Drude metal\air interface. Figure shows the problem of the momentum mismatch that must be overcome in order to couple light and excite SPP modes, the SPP mode always lies beyond the light line[15].

Now remember the dielectric function of an undamped free electron plasma for $\omega < \omega_p$:

$$\varepsilon(\omega) = 1 - \frac{{\omega_p}^2}{\omega^2} \quad 1.26$$

Substituting eq. 1.26 into 1.25 considering vacuum ($\varepsilon_2 = 1$) as dielectric interfaced with a Drude metal, we obtain the curve plotted in Fig. 1.3. As can be seen, the dispersion curve of a SPP lies always on the right side of the dispersion relation of light in vacuum and so SPPs are non radiative waves that cannot be excited directly by incident light. Additional momentum must be provided. At large k_x, the group velocity goes to zero, since the derivative of the dispersion relation tends to zero, and the phase velocity goes to zero as well. In this limit therefore SP resembles a localized fluctuation of the electron plasma. The characteristic frequency $\omega_{sp} = \omega_{plasma} / \sqrt{1 + \varepsilon_2}$ is called the *surface plasmon frequency*.
For small wavevectors, corresponding to low (mid-infrared or lower) frequencies, the SPP propagation constant is close to k_0 at the light line, and the wave extends over many wavelengths into the dielectric space. In this regime, SPPs therefore acquire the nature of grazing-incidence light field, and are also known as *Sommerfeld-Zennek waves*[16].

Now, let us briefly analyze the possibility of TE surface modes. In this case we will see that there are no modes supported at the metal-dielectric interface. This can be easily proved considering a TE mode as a guess solution of the wave equation:

for $z > 0$ (dielectric - medium #2)

$$\boldsymbol{E}_2 = \left(0, E_{2,y}, 0\right) e^{i(k_{2,x}x - k_{2,z}z - \omega t)}$$
$$\boldsymbol{H}_2 = \left(H_{2,x}, 0, H_{2,z}\right) e^{i(k_{2,x}x - k_{2,z}z - \omega t)} \qquad 1.27$$

for $z < 0$ (metal - medium #1)

$$\boldsymbol{E}_1 = \left(0, E_{1,y}, 0\right) e^{i(k_{1,x}x + k_{1,z}z - \omega t)}$$
$$\boldsymbol{H}_1 = \left(H_{1,x}, 0, H_{1,z}\right) e^{i(k_{1,x}x + k_{1,z}z - \omega t)} \qquad 1.28$$

Continuity of E_y and H_x at the interface leads to the condition:

$$\left(k_{1,z} + k_{2,z}\right) E = 0 \qquad 1.29$$

However, since the real parts of $k_{1,z}$ and $k_{2,z}$ must be positive in order to have a localized wave, the only solutions is $E = 0$. Thus an s-polarized surface plasmon polariton cannot propagate along the planar dielectric-metal interface and no surface modes exist for TE polarization. *Surface plasmon polaritons only exist for TM polarization*[5].

1.4 Spatial extension and propagation lengths of SPPs

As we mentioned above, surface plasmons polaritons are surface waves localized at the dielectric-metal interface. The field amplitude decreases exponentially in media #1 and #2 along the z direction normal to the surface as $\exp\left(-\left|k_{j,z} z\right|\right)$, since $k_{j,z}$ is purely imaginary.

The values of the skin depths at which the field falls to 1/e are:

$$d_{j,z} = \frac{1}{|k_{j,z}|} \tag{1.30}$$

and can be obtained using 1.24 and 1.25 (we assume here $\varepsilon_2^{''} = 0$).

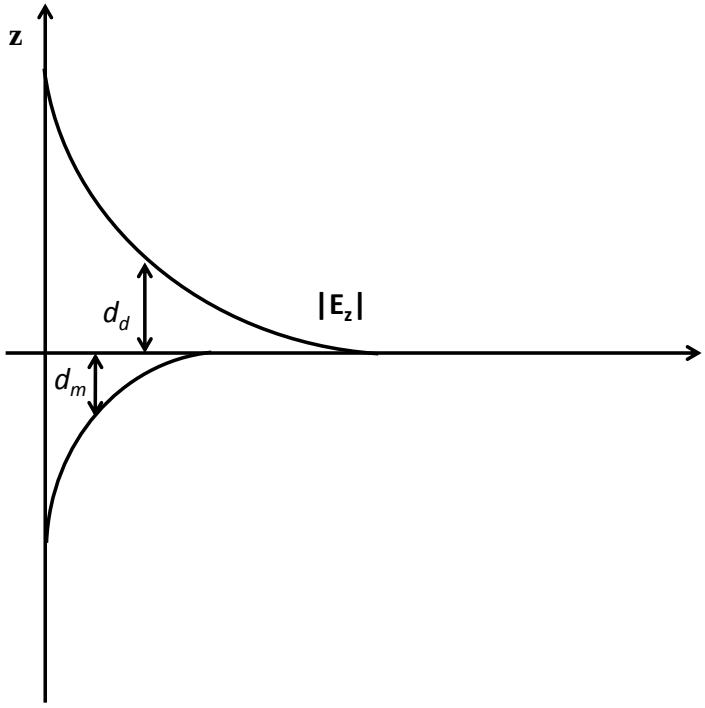

Fig. 1.4: SPP field components decrease exponentially going away from the interface. The evanescent field is related to the non-radiative nature of SPPs. It prevents power from propagating away from the surface [15].

$$d_{1,z} = \frac{\lambda}{2\pi}\sqrt{-\frac{\varepsilon_1^{'} + \varepsilon_2}{\varepsilon_1^{'2}}}$$
$$d_{2,z} = \frac{\lambda}{2\pi}\sqrt{-\frac{\varepsilon_1^{'} + \varepsilon_2}{\varepsilon_2^{2}}} \tag{1.31}$$

Let us consider for example SPPs propagating at the interface between air/water and a noble metal (Au or Ag), for λ = 633nm. We have the following spatial extension values:

Metal\Dielectric field depths (nm) ($\lambda = 633\text{nm}$)	air $\varepsilon_{air} = 1$	water $\varepsilon_{water} = 1.78$
$\varepsilon_{Au} = -12.1 + 1.3i$	$d_{Au,z} = 28$ $d_{air,z} = 336$	$d_{Au,z} = 27$ $d_{water,z} = 181$
$\varepsilon_{Ag} = -17 + 0.7i$	$d_{Ag,z} = 24$ $d_{Air,z} = 403$	$d_{Ag,z} = 23$ $d_{water,z} = 221$

Table 1: field penetration depths for SPPs excited at different metal\dielectric interfaces. In the dielectric medium above the metal, e.g. air or glass, the decay length of the field is of the order of half the wavelength of light involved, whereas the decay length into the metal is one order smaller[15].

From dispersion relation 1.25, if the dielectric function of the metal is complex, the wavevector k_x of the surface wave is complex. In the approximation that $|Re[\varepsilon_{dielectric}]| \gg Im[\varepsilon_{dielectric}]$ we have that the x-component of the plasmonic wavevector is a complex number:

$$k_x = \frac{\omega}{c}\sqrt{\frac{\varepsilon_1'\varepsilon_2}{\varepsilon_1' + \varepsilon_2}} + i\frac{\omega}{c}\left(\frac{\varepsilon_1'\varepsilon_2}{\varepsilon_1' + \varepsilon_2}\right)^{\frac{3}{2}}\frac{\varepsilon_1''}{2\varepsilon_1'^2} \qquad 1.32$$

The intensity of a SPP along the direction of propagation decreases as $\exp(-2x\, Im[k_x])$ and the *propagation length* of the SPPs can be defined as

$$L = \frac{1}{2k_x''} \qquad 1.33$$

If we consider again an SPP propagating at the interface between air or water and silver or gold, for an a TM wave at $\lambda = 633\text{nm}$, we get the following propagation lengths:

Metal\Dielectric propagation length (μm) ($\lambda = 633\text{nm}$)	air $\varepsilon_{air} = 1$	water $\varepsilon_{water} = 1.78$
$\varepsilon_{Au} = -12 + 1.3i$	10	4
$\varepsilon_{Ag} = -1.7 + 0.7i$	38	15

Table 2: field propagation length for SPPs excited at different metal\dielectric interfaces.

1.5 Multilayer systems

Multilayer systems consisting of alternating conducting and dielectric films can show a plasmonic behavior. In such systems, each single interface can sustain bound SPPs. When the separation between adjacent interfaces is comparable or smaller than the decay length *d* of the interface mode, interactions between SPPs give rise to *coupled modes*[5].

In order to explain the general properties of coupled SPPs, we will focus in particular to the simple geometry depicted in Fig. 1.5 consisting of a thin insulator core layer sandwiched between two semi-infinite metal slabs (MIM heterostructure).

Fig. 1.5: schematic representation of a Metal Insulator Metal (MIM) interface.

The magnetic field in the three regions will then be of the form:

$$H_y(x,z) = \begin{cases} H_{III}\exp i\left(k_x x + k_{III,z} z\right) & z > \text{a} \\ H_{I,1}\exp i\left(k_x x - k_{I,z} z\right) + H_{I,2}\exp i\left(k_x x + k_{I,z} z\right) & -a < z < \text{a} \\ H_{II}\exp i\left(k_x x - k_{II,z} z\right) & z < -a \end{cases} \qquad 1.34$$

while the other components of the field are zero. The z-components of the wavevectors are supposed to be purely imaginary and positive in order to give rise to evanescent waves in z-direction. In region II we have taken into account that the modes localized at the top and at the bottom interface couple. Similar considerations could be done for the electric field by using eq. 1.6.

Restricting now to the special symmetric case where the sub- and superstrates (II) and (III) are equal in terms of their dielectric constants, so that $\varepsilon_{II} = \varepsilon_{III}$ and $k_{II,z} = k_{III,z}$, and applying the requirement of continuity of H_y and E_x at the interfaces $z = \pm a$ we get:

$$\tanh\left(k_{I,z} a\right) = -\frac{k_{II,z}\varepsilon_I}{k_{I,z}\varepsilon_{II}} \qquad 1.35$$

$$\tanh(k_{I,z}a) = -\frac{k_{II,z}\varepsilon_I}{k_{I,z}\varepsilon_{II}}$$

It can be shown that the first equation 1.35 describes modes of odd vector parity while the second describes modes of even vector parity.

1.6 Long-Range and Short-Range Surface Plasmons

Consider now a planar structure consisting of a thick metal film sandwiched between two semi-infinite dielectrics that supports two independent surface plasmons at the opposite boundaries of the metal film[17]. If the metal film is enough thin, coupling between the surface plasmons at opposite boundaries of the metal film can occur, giving rise to mixed modes with definite symmetry. In such case the symmetric surface plasmon exhibits a propagation constant and attenuation, which both increase with increasing metal film thickness. On the contrary, propagation constant and attenuation of the antisymmetric surface plasmon decrease with increasing thickness of the metal film. The symmetric surface plasmon exhibits a lower attenuation than its antisymmetric counterpart, and therefore it is referred to as a long-range surface plasmon, whereas the antisymmetric mode is referred to as a short-range surface plasmon.

1.7 Excitation of SPPs by Light

SPPs propagating on a flat metal\dielectric interface can be considered as two-dimensional electromagnetic waves leading to evanescent decay on both sides of the interface. This is possible because SPPs dispersion curve lies to the right of the light line of the dielectric (given by $\omega = ck$). The projection along the interface of the momentum $k_x = k \sin\theta$ of photons impinging under an angle θ to the surface normal is always smaller than the SPP propagation constant β, even at grazing incidence, prohibiting phase-matching. Therefore SPPs excitation onto a smooth metal surface by three-dimensional light beams is not possible unless special techniques for phase-matching are employed. The x-component of the wavevector of light can be increased to match that of the surface plasmons exploiting the attenuated total reflection or diffraction, by using prisms or gratings.

1.7.1 Prism Coupling

The most common approach to excitation of surface plasmons is by means of a prism coupler and the attenuated total reflection method (ATR). There are two configurations of the ATR method – Kretschmann geometry [13] and Otto geometry[12].

In the Kretschmann configuration, a high refractive index prism with permittivity ε_p is interfaced with a metal–dielectric waveguide consisting of a thin metal film with permittivity ε_m and thickness q, and a semi-infinite dielectric with $\varepsilon_d(\varepsilon_d < \varepsilon_p)$, Fig. 1.6.

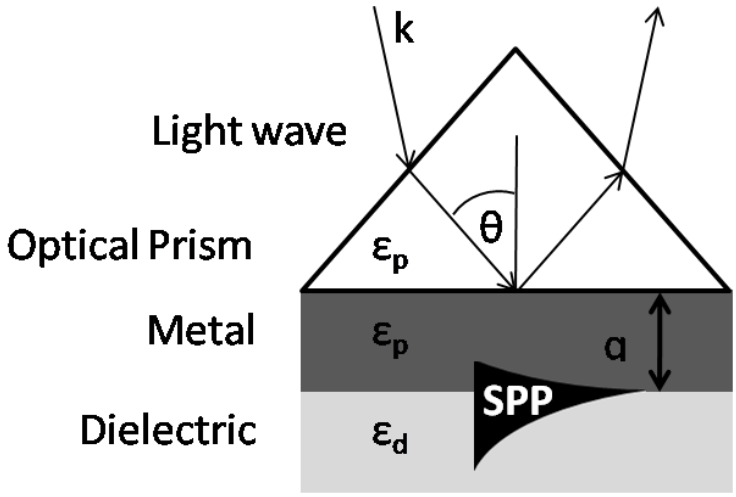

Fig. 1.6: Excitation of SPPs in the Kretschmann geometry: attenuated total reflection (ATR) method.

When a light wave propagating in the prism reaches the metal film a part of the light is reflected back into the prism and a part propagates in the metal in the form of an inhomogeneous electromagnetic wave [18], [19]. This inhomogeneous wave decays exponentially in the direction perpendicular to the prism–metal interface and is therefore referred as to an evanescent wave. If the metal film is sufficiently thin (less than 100 nm for light in visible and near IR), the evanescent wave penetrates through the metal film and couples with a surface plasmon at the outer boundary of the metal film.

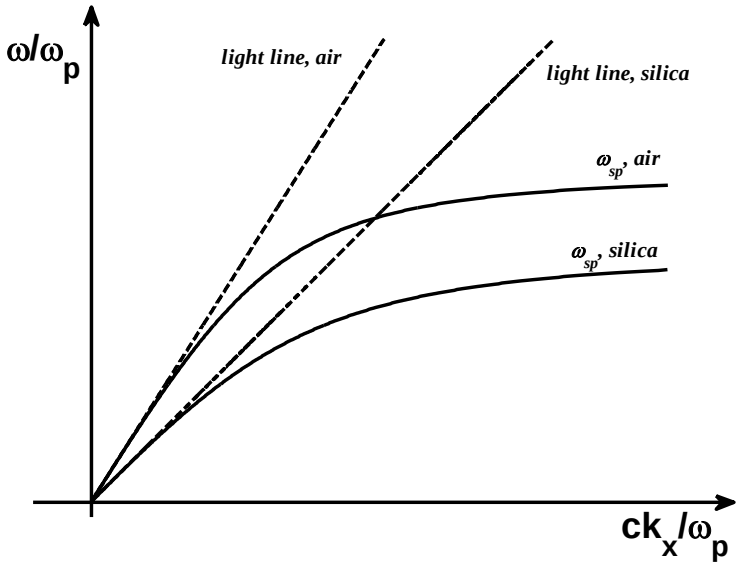

Fig. 1.7: dispersion relation of SPPs at the interface between a Drude metal and air or fused silica. This configuration shows the allowed region of wavevector for the excitation of SPPs. This is because the SP excited at the metal\air interface now lies above the light line of light passing across the prism.

The x-component of the momentum of light impinging on the metal-prism surface is $k_x = k_0\sqrt{\varepsilon_p}\sin\theta$. This momentum is not enough to excite a SPP on the *metal-prism*

interface for the same reasons explained before, i.e. SPP dispersion relation is now right from light line for light propagating in the prism (Fig. 1.7). However, it can be sufficient to excite a SPP at the *metal-dielectric* interface, so that we get:

$$k_0\sqrt{\varepsilon_p}\sin\theta = k_0\sqrt{\frac{\varepsilon_d\varepsilon_m^{'}}{\varepsilon_d+\varepsilon_m^{'}}} \qquad 1.36$$

Surface plasmon polaritons excited using prism based phase-matching are *leaky waves*[5], since they lose energy not only due to the inherent absorption inside the metal, but also due to leakage of radiation into the prism. The minimum in the intensity of the reflected beam is due to destructive interference between this leakage radiation and the reflected part of the excitation beam. For an optimum metal film thickness, the destructive interference can be perfect, providing a zero in the reflected beam intensity, so that leakage radiation cannot be detected.

In the Otto geometry, a high refractive index prism with permittivity ε_p is interfaced with a dielectric–metal waveguide consisting of a thin dielectric film, typically air, with $\varepsilon_d\left(\varepsilon_d < \varepsilon_p\right)$ and a semi-infinite metal with permittivity ε_m. Total internal reflection takes place at the prism/air interface, exciting SPPs via Near Field coupling to the air/metal interface. This configuration is preferable when direct contact with the metal surface is undesirable, for example for studies of surface quality.

1.7.2 Grating Coupling

A different approach used to overcome the mismatch in wavevector between the in-plane momentum $k_0\sin\theta$ of impinging photons and k_x can be also that of corrugating the metal surface by lithographically patterning a shallow grating with period Λ. Phase-matching happens if the momentum of the diffracted light parallel to the surface equals the propagation constant of the SPP:

$$k_{SPP} = \frac{\omega}{c}\sqrt{\frac{\varepsilon_m^{'}\varepsilon_d}{\varepsilon_m^{'}+\varepsilon_d}} = k_0 N_d\sin\theta + n\frac{2\pi}{\Lambda} = k_{x,n} \;\; and\; n = 1,2.. \qquad 1.37$$

where N_d is the refractive index of the dielectric, θ is the light incidence angle and Λ denotes the grating period.

When this resonance condition is satisfied by the n-th diffraction order its power is delivered to the SPP. Experimentally, a minimum in the reflectance spectrum is detected. The reverse process can also be considered: SPPs propagating along a grating can couple to light and thus radiate.

The gratings can be patterned onto the metal or onto the dielectric material. By designing the shape of the grating, the propagation direction of SPPs can be influenced and even focusing can be achieved, which was shown by Offerhaus and colleagues using non-collinear phase-matching[20]. For one-dimensional gratings, significant

changes to the SPP dispersion relation occur if the gratings are sufficiently deep so that the modulation can no longer be treated as a small perturbation of the flat interface.

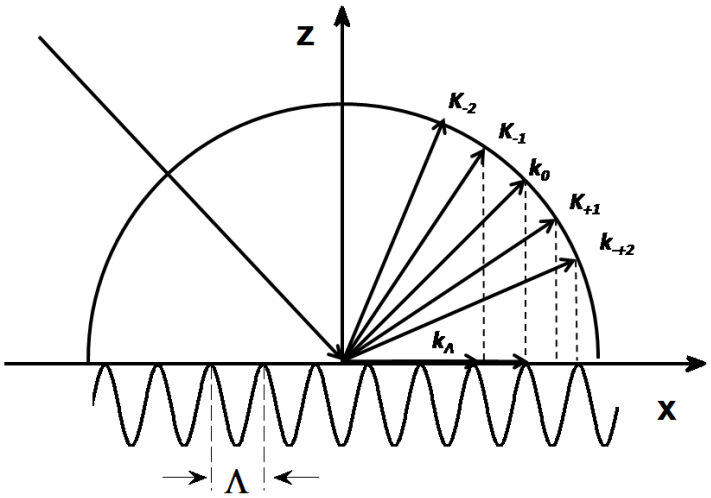

Fig. 1.8: SPP excitation by using the grating coupling method.

Appreciable band gaps, that is frequency regions over which the propagation of SPP modes is forbidden in particular directions, appear already for a groove depth on the order of 20 nm for metallic gratings. For even larger depths, localized modes inside the grooves lead to distortions of the first higher-order band folded back at the Brillouin zone boundary, enabling coupling even for short pitches $\Lambda < \lambda/2$ upon normal incidence due to a lowering in frequency of the modified SPP dispersion curve[21].
More generally, SPPs can also be excited on films in areas with random surface roughness or manufactured localized scatterers[5]. Momentum components Δk_x are provided via scattering.

2 Plasmonic enhanced Photovoltaics

2.1 Introduction

Development of energy production by means of Photovoltaics has the potential to give a large contribution to solve the problem of climate change. As the worldwide demand increases energy production could led to an unsustainable level of pollution and carbon dioxide emissions. Therefore, we must develop and use alternative and renewable energy resources, especially our only long-term natural resource, the sun. Solar cell are considered a major candidate for obtaining energy from the sun.

In principle, a photovoltaic solar cell is a semiconductor device that directly converts sunlight into electricity with high conversion efficiency. As long as light is shining on solar cells they generate DC electrical power by producing couples of free charge carriers of opposite signs that flow in an external circuit biased by the device. Therefore, they can provide nearly permanent power at low operating costs. However, solar cell performances must be enhanced and price needs to be reduced in order to make this technology competitive with fossil fuels and to reach the so called grid parity. Recently, research and development have made use of many innovative concepts (such as nanotechnology, and plasmonics) that have increased solar cells performances and have reduced their cost reaching today the level of economic feasible competition with other energy sources.

In this chapter, we will outline the basic concepts of semiconductor devices physics focusing the attention on the effect that the light absorption profile have on the short circuit current produced by the cell. The book: "Handbook of Photovoltaic Science and Engineering", by A. Luque and S. Hegedus is taken as the main reference[22].

2.2 Principles of Photovoltaics

Solar cells are devices having semiconductor materials as light absorbing media. These materials are characterized by the presence of a forbidden energy range in which allowed states cannot exist. Energy states or energy bands are permitted above and below this energy bandgap. The upper bands are called the conduction bands; the lower bands, the valence bands.

When energy exceeding the band gap threshold is obtained by the absorption of one photon a valence electron is promoted to a state in the conduction band. There, a specially made selective contact that collects conduction-band electrons drives such electrons to the external circuit. The electrons lose their energy by doing work in the external circuit and are restored to the solar cell by the other contact of the circuit.

The photovoltaic effect was discovered by Becquerel in 1839, in a junction formed between an electrode and an electrolyte[23] and observed by Ohl on a silicon p-n junction in 1940[24]. The photovoltaic effect on Ge was reported by Benzer in 1946 and by Pantchechnikoff in 1952[25], [26]. However, it was not until 1954 that the solar cell received much increased interest, initiated by the works of Chapin et al. on single-crystal silicon cells and of Reynolds et al. on cadmium sulfide cells[27], [28]. To date,

solar cells have been made in many other inorganic and organic semiconductors, using various device configurations, and employing mono-crystalline, poly-crystalline and amorphous materials.

2.2.1 Solar Radiation

Just above the Earth's atmosphere, the radiation intensity, or Solar Constant, is about 1353 W/m^2 and the spectral distribution is referred to as Air Mass zero (AM0) radiation spectrum. However, the atmosphere attenuates the sunlight before it reaches the earth's surface, mainly due to water-vapor absorption in the infrared, ozone absorption in the ultraviolet, and scattering by airborne dust and aerosols. The degree to which earth's atmosphere attenuates sunlight radiation is quantified by the AM value. For a path length L through the atmosphere, for solar radiation incident at angle θ relative to the normal to the Earth's surface (zenith), the air mass coefficient is:

$$AM = \frac{L}{L_0} \approx \sec\theta \qquad 2.1$$

defined as the secant of the angle between the sun and the zenith $(\sec\theta)$.

Fig. 2.1 shows the solar spectrums at AM1.5 condition and the black body radiation spectrum at T=5800 K [29]. Thus AM0 represents the solar spectrum outside the earth's atmosphere and can be approximated by a black-body spectrum. The AM1 spectrum represents the sunlight at the earth's surface when the sun is at zenith. The AM2 spectrum is for θ= 60°. Although AM0 spectrum is the relevant one for satellite and space-vehicle applications, the AM1.5 condition (with sun at 48.2° above the horizon) represents the reference for terrestrial applications. Thus, the standard spectrum at the earth's surface is called AM1.5G. This spectrum accounts for the direct and diffuse parts of solar radiation. In clear days the diffuse part of solar intensity is almost 10% of the direct component I_D. Therefore, the global intensity I_G follows the relation:

$$I_G = 1.1 \cdot I_D \qquad 2.2$$

Due to the convenience of the round number and the fact that there are inherently variations in incident solar radiation, the standard AM1.5G spectrum has been normalized to give 1kW/m^2.

Solar intensity reduces with increasing AM number, but, due to the complex and variable atmospheric factors involved, not in a linear behavior. One approximate model for solar intensity versus AM is given by:

$$I = 1.1 \cdot I_0 \cdot 0.7^{(AM^{0.678})} \qquad 2.3$$

where solar intensity external to the earth's atmosphere is I_o = 1.353 kW/m^2.

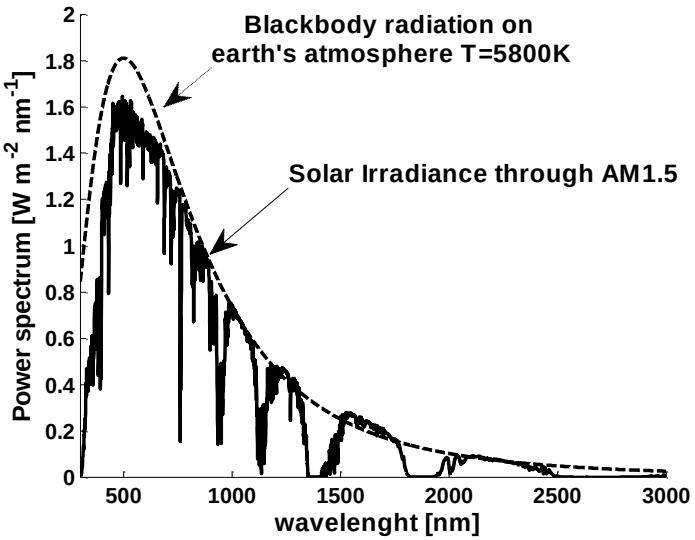

Fig. 2.1: AM1.5 solar Irradiance. Dashed line refer to the black body radiation spectrum corresponding at the earth's atmosphere, T=5800 K.

2.2.2 Ideal solar cell model

When a conventional single bandgap solar cell is exposed to sunlight, only photons with energy greater than E_g contributes with an electric charge to the cell output; the excess energy over E_g is wasted as heat. Ideally, the electric behavior of a solar cell is similar to a semiconductor diode that efficiently absorb and convert light energy from the sun into electrical energy by separating and conducting the carriers towards an exclusive direction.

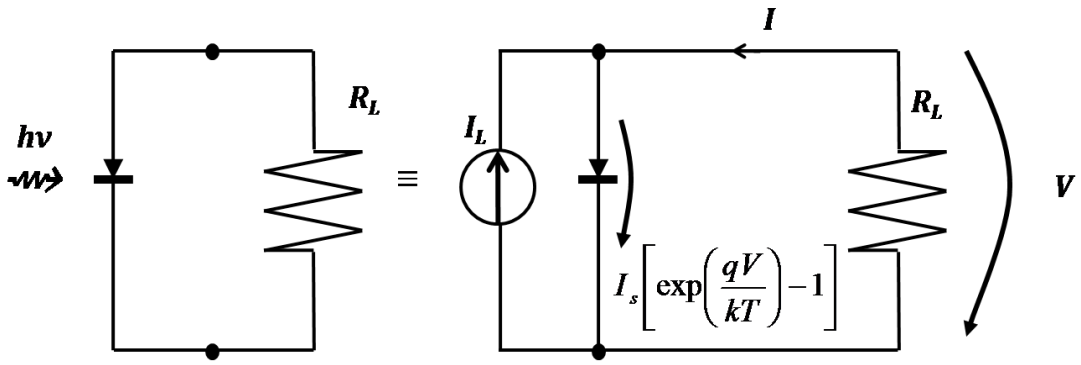

Fig. 2.2: Idealized equivalent circuit of solar cell under illumination.

Fig. 2.2 shows an idealized equivalent electric circuit of solar cell operating as a DC source of photocurrent in parallel with the *pn* junction. The source I_{L} results from excess carriers due to solar radiation; I_S is the diode saturation which follows an exponential behavior with respect to the energy gap[29].

$$I_S \propto \exp\left(\frac{-E_g}{kT}\right) \qquad 2.4$$

and R_L is the load resistance.
In order to obtain the photocurrent I_L, assuming total absorption, we need to integrate the total area under the graph shown in Fig. 2.1, that is,

$$I_L(E_g) = Aq \int_{h\nu=E_g}^{\infty} \frac{d\phi_{ph}}{dh\nu} d(h\nu) \qquad 2.5$$

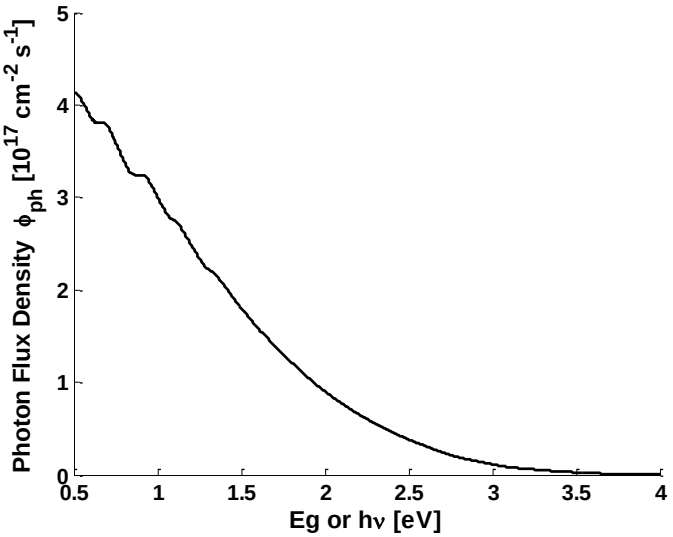

Fig. 2.3: Total number of photons in the AM1.5 solar spectrum above an energy value, contributing to the maximum photocurrent for a solar cell made with a specific E_g.

As can be seen, in Fig. 2.3 is depicted the value of photocurrent as a function of the bandgap of the semiconductor. For a smaller bandgap $I_L(E_g)$ increases because more photons are collected.
Thus, referring to the equivalent circuit of Fig. 2.2, the I-V characteristics under illumination is obtained by a sum of the dark current $I_s\left[\exp\left(\frac{qV}{kT}\right)-1\right]$ and the photocurrent I_L(see section 2.2.3.5 and Fig. 2.10 for more details):

$$I = I_s\left[\exp\left(\frac{qV}{kT}\right)-1\right] - I_L \qquad 2.6$$

When $I = 0$ the circuit is open and the corresponding value of voltage V_{OC} is

$$V_{OC} = \frac{kT}{q}\ln\left(\frac{I_L}{I_s}+1\right) \approx \frac{kT}{q}\ln\left(\frac{I_L}{I_s}\right) \qquad 2.7$$

Notice that, for a fixed photocurrent I_L, the open-circuit voltage logarithmically increases its value with decreasing saturation current I_s and, for a regular p-n junction, the ideal saturation current I_s decreases exponentially with E_g. So to obtain a large V_{OC},

a large E_g is required. When $V = 0$ the device current I_{sc} equals the photo-generated one.

Summarizing, the photocurrent increases with smaller E_g and, on the other hand, the voltage increases with E_g by having a small saturation current. So to maximize the power, there exists an optimum value for the bandgap Eg.

2.2.3 Principles of Solar Cells Physics

A simple conventional mono-crystalline silicon solar cell structure is illustrated in Fig. 2.4: schematic conventional silicon solar cell and generation of a electron-hole pair. Sunlight is incident from the top on the front of the solar cell.

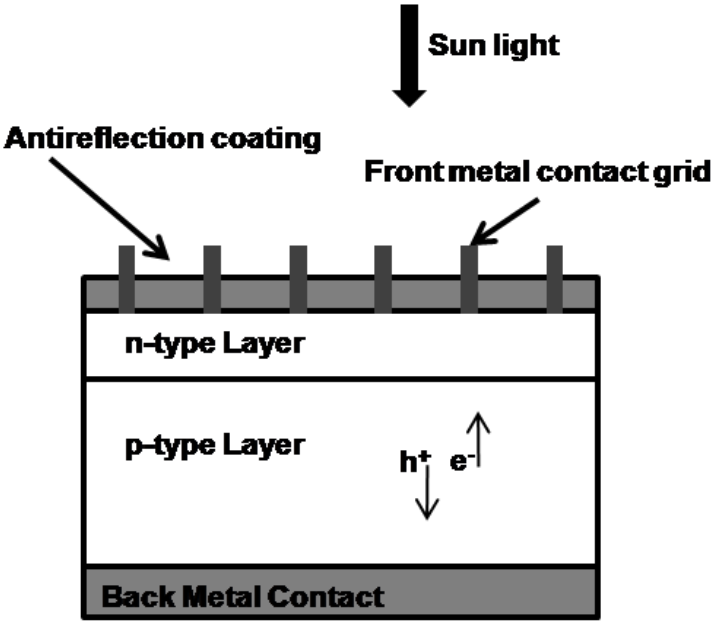

Fig. 2.4: schematic conventional silicon solar cell and generation of a electron-hole pair.

A transparent insulating dielectric layer coats the front surface with two aims: it passivates the surface reducing surface recombination of generated carriers; the optical thickness is designed to get an anti-reflection coating for light incident on the device. A metallic grid of electrical contacts is realized on the front surface in order to collect the photo-current trying to minimize the shading effect and ohmic losses. A flat metal layer on the other surface is realized as back contact.

2.2.3.1 Mechanisms related to light absorption on semiconductors

The mechanism of creation of electron–hole pairs by the absorption of sunlight is fundamental to the operation of solar cells. Both the total energy and momentum of all particles involved in the absorption process must be conserved. Since the sunlight photon momentum, $p_{ph} = h/\lambda$, is very small compared to the range of the crystal momentum, $p_C = h/\mathrm{l}$, the conservation law that must be followed is only for the momentum of the electron. In case of direct and indirect gap transitions the conservation laws are expressed in eq.s 2.8 and 2.9.

$$p_{el,f} = p_{el,i} + p_{ph} \approx p_{el,i} \quad 2.8$$

$$p_{el,f} = p_{el,i} + p_{ph} + p_{phonon} \approx p_{el,i} + p_{phonon} \quad 2.9$$

On the other side, the conservation of energy dictates that the energy of the absorbed photon is:

$$E_f - E_i = h\nu \quad 2.10$$

2.2.3.2 Generation

Let us define now an absorption coefficient for a given photon, hν, that is proportional to the probability of transition between different electronic states ($P_{1,2}$), the density of electrons in the initial state, $g_v(E_i)$, and the density of available allowed final states $g_c(E_f)$, and is then summed over all possible transitions between states where $E_f - E_i$:

$$\alpha(h\nu) \propto \sum P_{1,2} g_v(E_i) g_c(E_f) \quad 2.11$$

assuming that the valence-band is full and the conduction-band is empty. Absorption results in creation of an electron-hole pair since a valence electron is excited to the conduction band leaving a free hole in the valence band.

Assuming parabolic bands, the absorption coefficient for direct transitions is proportional to:

$$\alpha(h\nu) \propto A^*(h\nu - E_g)^{1/2} \quad 2.12$$

where A^* is a constant.

In indirect band gap semiconductors like Si and Ge, conservation of electron momentum necessitates that the photon absorption process involves an additional particle. Thus, light absorption could exist if either phonon absorption or phonon emission happens and the absorption coefficient could be obtained by the sum of the term that accounts for phonon absorption and that for phonon emission

$$\alpha(h\nu) = \alpha(h\nu)_e + \alpha(h\nu)_a \quad 2.13$$

where

$$\alpha(h\nu)_{a,e} = \frac{A(h\nu - E_g \pm E_{phonon})^2}{\pm\left(\exp\left(\frac{E_{phonon}}{kT}\right) - 1\right)} \quad 2.14$$

An interesting consideration could be done for the absorption phenomena related direct and indirect gap semiconductors. Since the indirect gap absorption coefficient depends not only on the density of full initial electron states and empty final electron states but

also on the availability of phonons, its value is smaller than that of direct transitions. Thus, light penetrates more deeply into indirect band gap semiconductors than direct band gap semiconductors.
A number of different absorption mechanism could also occur. One of such phenomena is the free-carrier absorption, in which electrons move "inside" the conduction band absorbing the energy of a photon and reaching an empty state higher in the conduction band. However, this mechanism is only significant for photons with energy smaller than E_g , therefore it does not affect the creation of electron–hole pairs and can be ignored. However, free-carrier absorption has to be considered in tandem solar cell systems in which a wide band gap solar cell is stacked on top of a solar cell of smaller band gap.

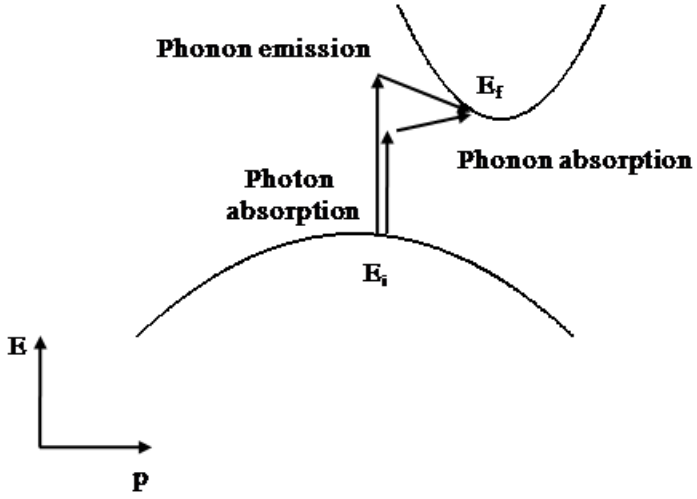

Fig. 2.5: light absorption in an indirect band gap semiconductor for a photon with energy $h\nu < E_f - E_i$ and a photon with energy $h\nu > E_f - E_i$. Energy and momentum in each case are conserved by the absorption and emission of a phonon.

The absorption coefficient, described above, is closely related to the rate of generation of electron–hole pairs inside the absorber. Let us first consider the well known Lambert-Beer equation that, given an incident light intensity I_0 and an absorption coefficient α, neglecting reflections, gives the intensity inside the device at any distance x from the surface: $I = I_0 e^{-\alpha x}$. This equation is closely related to the rate of electron-holes pair being generated in a solar cell:

$$G(x) = (1 - s) \int \big(1 - r(\lambda)\big) f(\lambda) \alpha(\lambda) e^{-\alpha x} d\lambda \qquad 2.15$$

where s is the grid-shadowing factor, r (λ) is the reflectance, α(λ) is the absorption coefficient, f (λ) is the incident photon flux and $x = 0$ is assumed as the position of the front absorbing layer surface.
The generation of electron-hole pairs within the semiconductor absorber follows an exponential decrease. The rate is different at each wavelength since the absorption

coefficient depends on both the material and the wavelength of incident light and exhibit a sharp edge for that part of solar spectrum which has energy below the band gap.

2.2.3.3 Recombination

The generation of electron-hole pairs inside a solar cell is balanced by a number of different mechanisms by which electrons and holes tend to relax back toward their equilibrium values through a process called recombination. There are several recombination mechanisms important to the operation of solar cells: recombination through defects in the forbidden gap, radiative (band-to-band) recombination, and Auger recombination[22], [30] (Fig. 2.6).

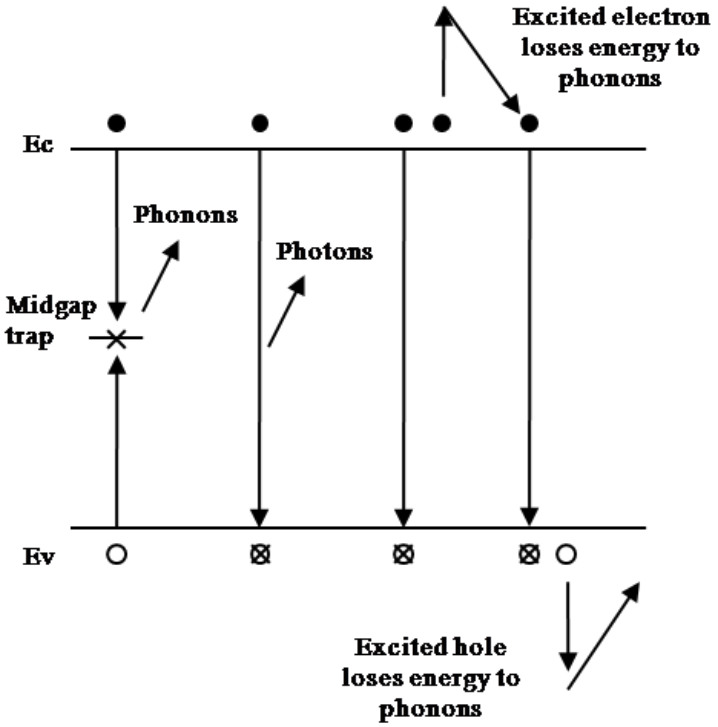

Fig. 2.6: Recombination processes in semiconductors

The net recombination rate per unit volume per second (the same units of G) related to the different recombination mechanisms could be expressed as:

$$R = K(np - n_i^2) \qquad 2.16$$

where K is an expression characteristic of the different mechanism, n_i is the intrinsic carrier density, n and p are respectively the electron and hole concentrations.

Notice that the recombination rate is solely dependent on the minority carrier (also called the limiting carrier). This is reasonable since there are far fewer minority carriers than majority carriers and one of each is necessary to have a recombination event. Thus

assuming that the material is in a low injection condition, i.e. for a p type doped semiconductor where $p \approx p_0 \gg n_0$ means that $n_0 \leq n \ll p_0$, eq. 2.16 results in

$$R_p = \frac{n - n_0}{\tau} \qquad 2.17$$

and for n type doped semiconductors:

$$R_n = \frac{p - p_0}{\tau} \qquad 2.18$$

where n_0 and $p_0$are the charge concentrations at equilibrium.

Recombination mechanisms	**Minority carrier lifetime τ**	
	minority carrier type	
	n	p
Radiative	$\frac{1}{p_0 B_R}$	$\frac{1}{n_0 B_R}$
Auger	$\frac{1}{p_0^2 B_A}$	$\frac{1}{n_0^2 B_A}$
Shockley-Read-Hall	$\frac{1}{\sigma v_{th,n} N_T}$	$\frac{1}{\sigma v_{th,p} N_T}$
B_A B_R: Auger and Radiative recombination constants $v_{th,n}$: Thermal carrier velocity N_T σ : trap concentration and trap cross section		

Table 3: Minority carrier lifetime τ of carriers due to the different recombination mechanisms. See eq.s 2.17 and 2.20[22], [31].

Each of these recombination processes occurs in parallel, thus the total recombination rate is the sum of rates due to each process:

$$R_{tot} = R_{radiative} + R_{SRH} + R_{Auger} \qquad 2.19$$

and the total lifetime is:

$$\tau_{tot} = \tau_{radiative}^{-1} + \tau_{SRH}^{-1} + \tau_{Auger}^{-1} \qquad 2.20$$

Finally, interfaces between two dissimilar materials, such as, those that occur at the front surface of a solar cell, have a high concentration of defects due to the abrupt termination of the crystal lattice. These manifest themselves as a continuum of traps within the forbidden gap at the surface; electrons and holes can recombine through them just as with bulk traps.

Rather than giving a recombination rate per unit volume per second, surface traps give a recombination rate per unit area per second. A general expression for surface recombination for p type materials is:

$$R_{surface\ ,p} = S_p(n - n_0) \tag{2.21}$$

and for n type semiconductors:

$$R_{surface\ ,n} = S_n(p - p_0) \tag{2.22}$$

S_p and S_n are effective surface recombination velocities. It should be mentioned that these effective recombination velocities are not necessarily constants, although they are usually treated as such.

2.2.3.4 Carrier transport

When electron-hole pairs are subject to an electric field they move like free particles of the same electronic charge with effective masses of m_n^* and m_p^* respectively. Electrons in the conduction band, being negatively charged, move in the opposite direction of the applied field and holes in the valence band, being positively charged, move in the same direction of the applied field. However, their motion is subjected to scattering events thus, on average, carriers travel with a constant mean speed v_{drift} such that $m_n^* v_{drift}$ equals the momentum variation due to electric field in the time τ_c between two collisions. This result in

$$m_n^* v_{drift} = -eE\tau_c \tag{2.23}$$

and

$$J_n^{drift} = -nev_{drift} = \frac{ne^2\tau_c}{m_n^*}E = e\mu_n nE = \sigma_n E \tag{2.24}$$

where we have defined the electron mobility $\mu_n = \frac{q\tau_c}{m_n^*}$ and the electronic conductivity $\sigma_n = e\mu_n n$. Notice that, since σ_n is proportional to n in n-doped semiconductors the (electronic) conductivity is much higher than in intrinsic ones.

The most significant scattering mechanisms in solar cells are lattice vibrations (phonon) and ionized impurity scattering. These component mobilities at first approximation can be written for lattice scattering as

$$\mu_L \propto T^{-3/2} \tag{2.25}$$

and

$$\mu_I \propto \frac{T^{3/2}}{N_I} \qquad 2.26$$

where T is the temperature and N_I is the concentration of ionized impurities. These can then be combined using Mathiessen's rule to give the first order total carrier mobility[22]:

$$\frac{1}{\mu} = \frac{1}{\mu_L} + \frac{1}{\mu_I} \qquad 2.27$$

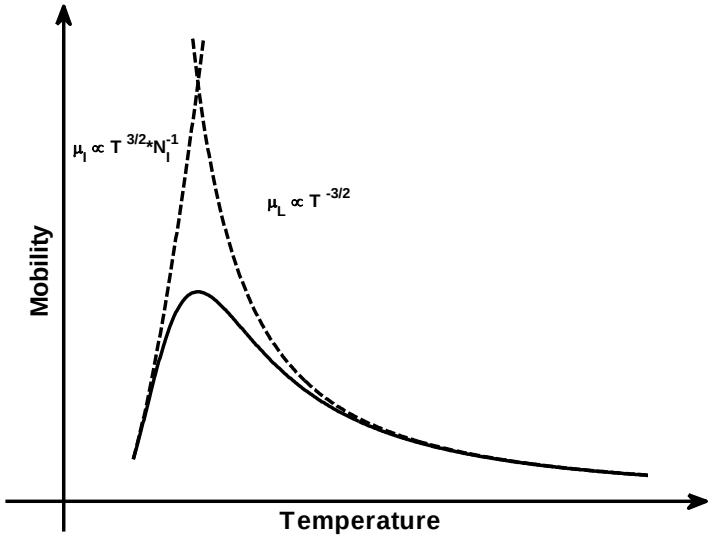

Fig. 2.7: carrier mobility behavior versus temperature using Mathiessen's rule[22].

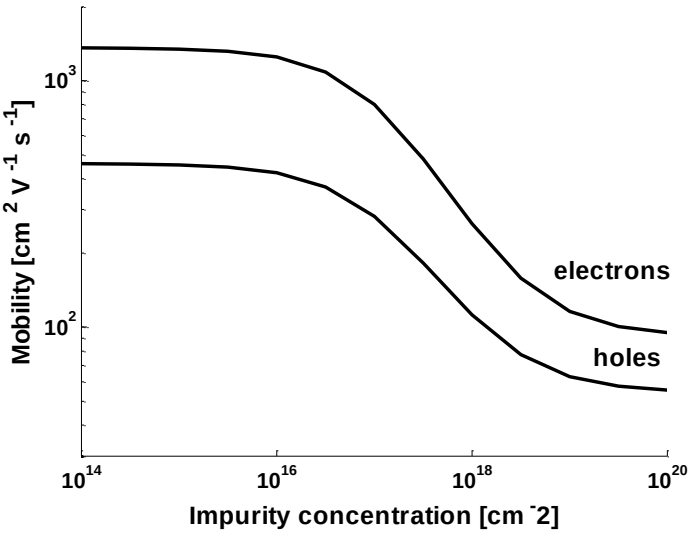

Fig. 2.8: Electron and hole mobilities in silicon for T = 300 K

When modeling solar cells, it is more convenient to use measured data or empirical formulas. Carrier mobilities in Si at 300 K are well approximated by [32]

$$\mu_n = 92 + \frac{1268}{1 + \left(\frac{N_I}{1.3E17}\right)^{0.91}} cm^2 V^{-1} s^{-1} \quad 2.28$$

and

$$\mu_p = 54.3 + \frac{406.9}{1 + \left(\frac{N_I}{2.35E17}\right)^{0.88}} cm^2 V^{-1} s^{-1} \quad 2.29$$

Electrons and holes in semiconductors tend, as a result of their random thermal motion, to diffuse from regions of high concentration to regions of low concentration. Thus:

$$J_n^{diff} = qD_n \nabla \mathrm{n} \quad 2.30$$

$$J_p^{diff} = -qD_p \nabla \mathrm{p} \quad 2.31$$

where D_p and D_n are the hole and electron diffusion coefficients, respectively.
Diffusion coefficients are fundamental quantities in the physics of a solar cell, since, together with lifetimes of carriers, they determine the diffusion length L of the carriers, on which the cell efficiency crucially depends. The lifetime of carriers τ is defined as the mean lifetime of a carrier before recombining with a carrier of the opposite sign.
For electrons, the relation among τ_n, L_n, D_n is found combining eq. 2.30 with the equation of conservation of number of particles (consider for simplicity a mono-dimensional problem).

$$\frac{\partial n}{\partial t} + \frac{\partial J_n}{\partial x} = 0 \quad 2.32$$

that results in:

$$\frac{\partial n}{\partial t} = D_n \frac{\partial^2 n}{\partial x^2} \quad 2.33$$

Let us consider now as boundary conditions a Dirac's δ concentration in $x = 0$ at $t = 0$, the solution turns out to be

$$n(x,t) = \frac{1}{\sqrt{4\pi D_n t}} e^{\frac{-x^2}{4D_n t}} \quad 2.34$$

which is a Gaussian that spreads out with time. If we consider now the mean square diffusion length at time *t* , we find

$$\langle x^2 \rangle = \int x^2 n(x,t) dx = 2D_n t \quad 2.35$$

Therefore, if a conduction electron (of course the same discussion for holes) lives for a time τ_n and then recombines, it will travel for a typical diffusion length given by:

$$L_n \sim \sqrt{D_n \tau_n} \tag{2.36}$$

Finally, we can derive the total current flowing in a solar cell:

$$J = J_p + J_n \tag{2.37}$$

where

$$\begin{aligned} J_n &= J_n^{drift} + J_n^{diff} = q\mu_n nE + qD_n \nabla n \\ J_p &= J_p^{drift} + J_p^{diff} = q\mu_p pE + qD_p \nabla p \end{aligned} \tag{2.38}$$

2.2.3.5 I-V characteristics

The idealized eq. 2.6 that represent the I-V behavior of a typical solar cell will be now presented more in depth. Let us consider the expression of the total current that is valid everywhere within the solar cell (note that A is the area normal section of the solar cell)

$$I = A\left[J_p(x) + J_n(x)\right] \tag{2.39}$$

Compared to eq. 2.6, a more advanced model of the current voltage characteristic of a solar cell is represented by the two diodes model:

$$I = I_{SC} - I_{01}\left(e^{qV/kT} - 1\right) - I_{02}\left(e^{qV/2kT} - 1\right) \tag{2.40}$$

where I_{SC} is the short circuit current and is the sum of the contributions from each of the three regions: the n-type region (I_{SCN}), the depletion region ($I_{SCD} = AJ_D$), and the p-type region (I_{SCP}) so that

$$I_{SC} = I_{SCN} + I_{SCD} + I_{SCP} \tag{2.41}$$

and I_{01} is the dark saturation current due to recombination in the quasi-neutral regions,

$$I_{01} = I_{01,p} + I_{01,n} \tag{2.42}$$

I_{02} is the dark saturation current due to recombination in the space-charge region

$$I_{02} = qA\frac{W_D n_i}{\tau} \qquad 2.43$$

Notice that, I_{02} is bias-dependent since the depletion width, WD, is a function of the applied voltage.

The short-circuit current and dark saturation currents are given by rather complex expressions that depend on the solar cell structure, material properties and the operating conditions. However we can now simplify the discussion by modeling the cell by introducing an equivalent electric circuit just like that of Fig. 2.2. In this case an ideal current source (I_{SC}) is in parallel with two diodes – one with an ideality factor of "1" and the other with an ideality factor of "2", as shown in Fig. 2.9.

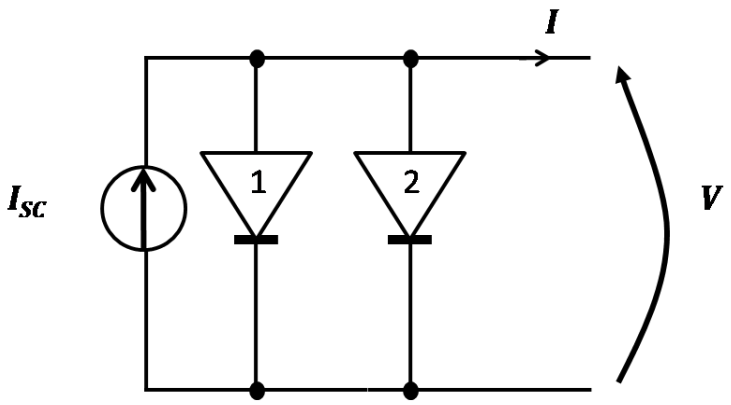

Fig. 2.9: simple solar cell model. I_{SC} is the short circuit current and the two diodes have as saturation current respectively I_{01}, due to recombination in the quasi-neutral regions, and I_{02}, due to recombination in the space-charge region.

Let us consider now a set of typical parameters for a solar cell (Table 4).

Si solar cell common parameters	
A	100 cm^2
W_n	0.35 µm
N_D	1E20 cm^{-3}
D_p	1.5 $cm^2 V^{-1} s^{-1}$
$S_{F,eff}$	3E4 cm s^{-1}
τ_p	1 µs
L_p	12 µm
W_p	300 µm
N_A	1E15 cm^{-3}
D_n	35 $cm^2 V^{-1} s^{-1}$
S_{BSF}	100 cm s^{-1}
τ_n	350 µs
L_n	1100 µm

Table 4: typical Si solar cell parameters used here for the development of the model.

These values are used to draw an example of I –V characteristic (Fig. 2.10) where, for simplicity we have neglected the dark current I_{02} due to the depletion region (diode 2).

2.2.3.6 Solar cell figures of merit

The graph of Fig. 2.10 allows us to clarify the fundamental figures of merit by which one can describe the macroscopic behavior of any solar cell. These are: the short-circuit current I_{SC}, the open-circuit voltage V_{OC}, and the fill factor FF.

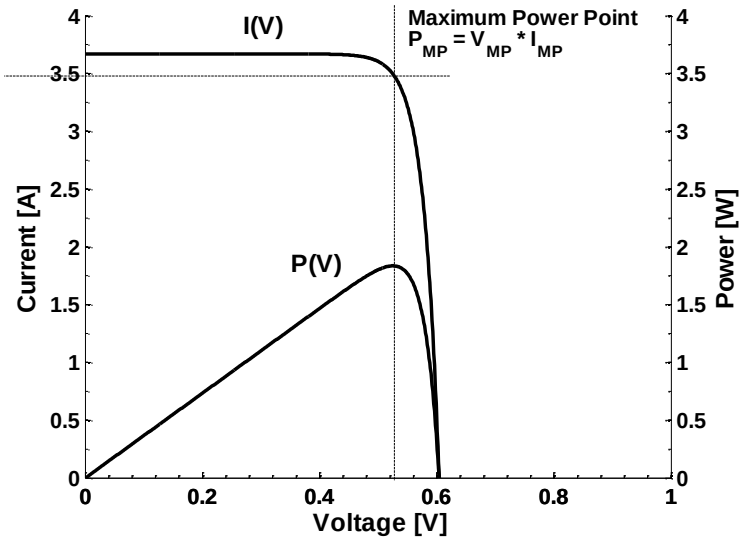

Fig. 2.10: I-V characteristic of the silicon solar cell model (see Table 4) and the corresponding power characteristic. Here the I_{SC} value is equal to 3.67A and $V_{OC} = 0.604V$. From the plot of $P(V)$ we can derive the value of P_{MP} and therefore the corresponding I_{MP} and V_{MP}.

At small voltages, the diode current is small and $I \sim I_{SC}$. When the voltage is high enough so that the diode current (recombination current) becomes significant, the solar cell current drops quickly. Therefore, at open circuit, all the light-generated current is flowing through diode 1 so the open-circuit voltage can be written as

$$V_{OC} = \frac{kT}{q} \ln \frac{I_{SC} + I_{01}}{I_{01}} \approx \frac{kT}{q} \ln \frac{I_{SC}}{I_{01}} \qquad 2.44$$

valid for $I_{SC} \gg I_{01}$.

From the plot of $P(V)$ we can derive the value of P_{MP} and therefore the corresponding I_{MP} and V_{MP} that, together whit I_{SC} and V_{OC} are useful for the determination of the fill factor FF and η.

$$FF = \frac{I_{MP} V_{MP}}{I_{SC} V_{OC}} \qquad 2.45$$

and

$$\eta = \frac{I_{MP} V_{MP}}{P_{in}} \qquad 2.46$$

Another fundamental figure of merit is the external collection efficiency, which takes into account both optical and recombination losses:

$$\eta_C^{ext} = \frac{I_{SC}}{I_{ph}} \qquad 2.47$$

where

$$I_{ph} = qA \int_{\lambda<\lambda_{gap}} f(\lambda) d\lambda \qquad 2.48$$

is the maximum possible ideal photocurrent that could be generated.
Summarizing, one could affirm that an ideal solar cell must have a high short-circuit current, a high open-circuit voltage, and a fill factor, *FF*, as close as possible to 1. This can be achieved by minimizing the recombination rates throughout the device (the objective is to collect the minority carriers before they are lost due to recombination) and by maximizing the absorption of photons with $E > E_{gap}$.

2.2.3.7 Real solar cell I-V characteristic: parasitic resistance effects

The real solar cells behavior is subjected to a number of different parasitic terms, namely series (R_s) and shunt resistances (R_{sh}), that have to be considered inside the eq. 2.40, thus

$$I = I_{SC}^{'} - I_{01}\left(e^{q(V+IR_S)/kT} - 1\right) - I_{02}\left(e^{q(V+IR_S)/2kT} - 1\right) - \frac{V + IR_S}{R_{Sh}} \qquad 2.49$$

where $I_{SC}^{'}$ is the short-circuit current when there are no parasitic resistances.

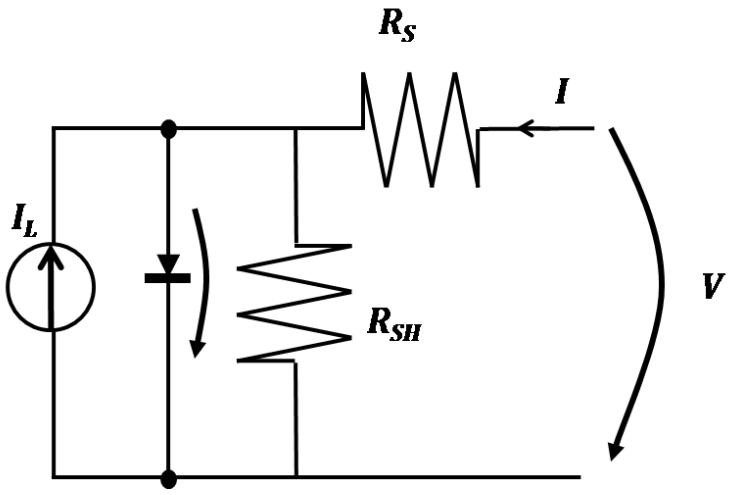

Fig. 2.11: parasitic series and shunt resistances.

The major contributors to the series resistance (Rs) are the bulk resistance of the semiconductor material, the metallic contacts and interconnections, carrier transport through the top diffused layer, and contact resistance between the metallic contacts and the semiconductor. The effect of series resistance is shown in Fig. 2.12.

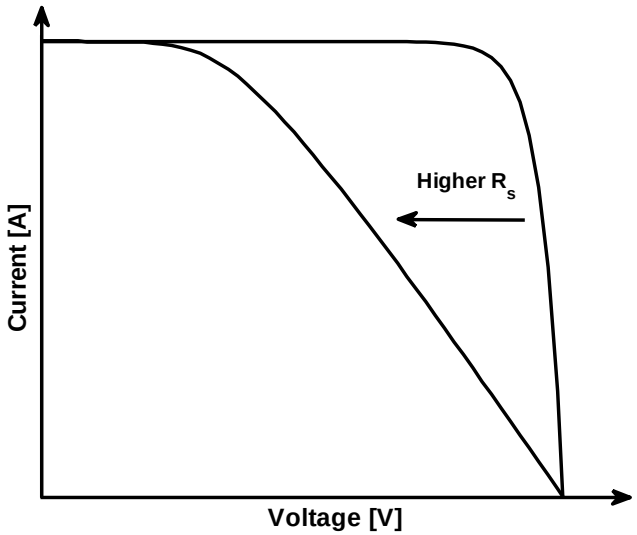

Fig. 2.12: the effect of R_s on IV characteristic.

The shunt resistance (Rsh) is due to *p*-*n* junction non-idealities and impurities near the junction, which cause partial shorting of the junction, particularly near cell edges. The effect of shunt resistance is shown in Fig. 2.13.

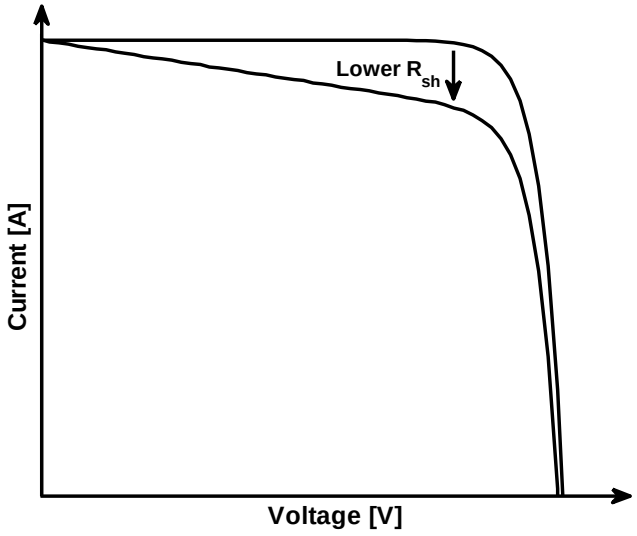

Fig. 2.13: the effect of R_{sh} on IV characteristic.

2.3 Plasmonics for Photovoltaics

Recently, the emerging knowledge related to Plasmonics applied to Photovoltaics is giving a relevant number of breakthroughs in defining new design strategies that can be used to maximize and concentrate the absorption of light[33], [34]. Thus permitting a considerable reduction in the physical thickness of solar photovoltaic absorber layers. At present most of the price of conventional solar cells is due to the cost of silicon wafers. Therefore, there is a great interest in reducing absorber material thicknesses toward thin-film devices with thickness in the range of 1μm. Thin-film solar cells are made from a variety of semiconductors including amorphous and polycrystalline Si, GaAs, CdTe and $CuInSe_2$, as well as organic semiconductors. A limitation in all thin-film solar-cell technologies is that the device thickness is lower than the absorption depth of photons over a broad wavelength range, in particular for the indirect-bandgap semiconductor Si. Therefore, structuring thin-film solar cells so that light is trapped inside in order to increase the absorbance is very important. A light trapping method applied on conventional wafer-based devices is achieved using a surface texturing, e.g. by employing the anisotropic etching of Si by KOH. Surface texturing scatters incoming photons into the solar cell over a large angular range, thus increasing the effective path length in the cell. However, this is not suitable for thin-film cells since the surface roughness would exceed the film thickness and because the greater surface area would increase minority carrier recombination in the surface and junction regions. A new method for achieving light trapping in thin-film solar cells is the use of metallic nanostructures that support surface plasmons[35] by which light can be concentrated and guided into the active layer to increase the absorption. Both localized surface plasmons excited in metal nanoparticles and surface plasmon polaritons (SPPs) propagating at the metal/semiconductor interface are of interest. However the main focus of the thesis is on the latter excitation.

2.3.1 Plasmonic enhanced solar cell design solutions

One of the first aims of a solar cell designer is to realize devices that are optically thick and thin for electrons. This is to achieve at the same time almost-complete light absorption and maximum photocarrier current collection. In order to solve such trade-off, one can employ plasmonic nanostructures at least in three ways (Fig. 2.14). First, a corrugated metallic film that can couple sunlight into SPP modes supported at the metal/semiconductor interface as well as guided modes in the semiconductor slab. Second, metallic nanoparticles can be used as subwavelength scattering elements to couple and trap light into an absorbing semiconductor thin film. Third, metallic nanoparticles can be used as subwavelength antennas enhancing the effective absorption cross-section. These three light-trapping techniques may allow considerable reduction of the photovoltaic layer thickness, while keeping the optical absorption (and thus efficiency) constant [35]. A fundamental characteristic of plasmon light-trapping concepts relying on scattering using localized modes is that they are relatively insensitive to the angle of incidence. This is an advantage for solar cell designs made for areas where incident sunlight is mostly diffuse rather than direct.

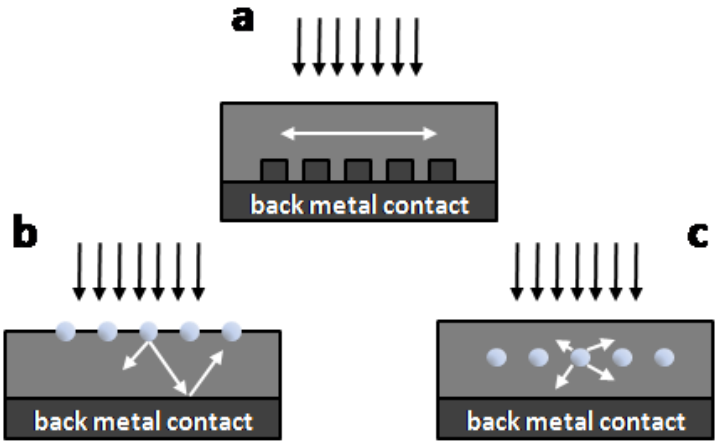

Fig. 2.14: Different plasmonic light trapping geometries. a) Light trapping by the excitation of SPPs at the metal/semiconductor interface. A corrugated metal back surface couples light to SPPs or photonic modes that propagate in the plane of the semiconductor layer. b) Light trapping by scattering from metal nanoparticles at the solar cell surface. Light is preferentially scattered and trapped into the semiconductor thin film by multiple and high-angle scattering, causing an increase in the effective optical path length in the cell. c) Light trapping by the excitation of localized surface plasmons in metal nanoparticles embedded in the semiconductor.

Plasmonic structures can be employed to improve the efficiency of many different solar cell designs with the constant aim of increasing absorption by light confinement and scattering.

Plasmonic solutions for tandem solar cells may be made by structuring each metal contact interlayer with a plasmonic nanostructure that couples different spectral bands in the solar spectrum into the corresponding semiconductor layer. Coupling sunlight into SPPs could also solve the problem of light absorption in quantum-dot solar cells. In general, field concentration in plasmonic nanostructures is likely to be useful in any type of solar cell where light concentration is beneficial.

2.3.2 Light trapping using SPPs.

One of the possible plasmonic light-trapping mechanism is that of employing SPPs traveling along the interface between the metal back contact and the semiconductor absorber layer (see Fig. 2.14a). Excited SPP fields could be confined at the metal/semiconductor interface at dimensions much smaller than the wavelength thus efficiently trapping and guiding light in the semiconductor layer. Therefore, the incident solar flux can be absorbed along the lateral direction of the solar cell, which has dimensions that are orders of magnitude larger than the optical absorption length.

Notice that, the SPP coupling mechanism is useful only if absorption in the semiconductor overcome power dissipation in the metal. This is illustrated in Fig. 2.15, which shows a calculation of the fraction of SPP that penetrates in the semiconductor Si or the organic blend P3HT:PCBM film in contact with either Ag or Al. Notice in particular the computation of the relative absorption in case of organic semiconductor interface with either aluminum or silver. In such case, the penetration is higher in the semiconductor compared to the metal over the entire spectral range of interest.

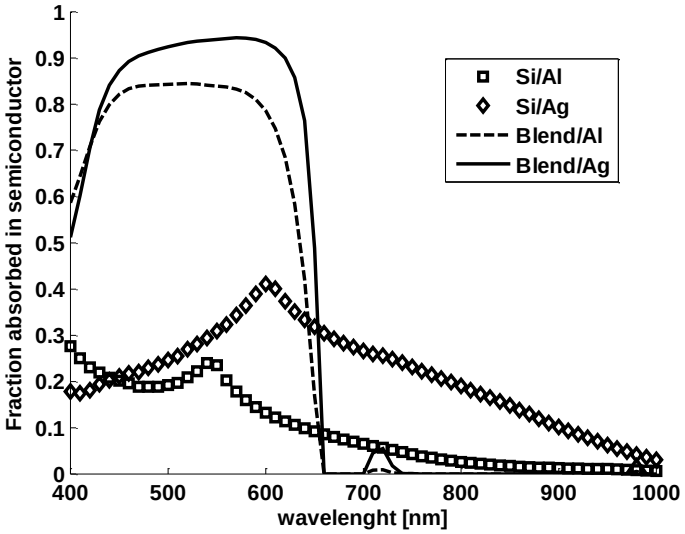

Fig. 2.15: relative penetration depth into the semiconductor for different metal\semiconductor interfaces.

Due to the momentum mismatch between the incident light and the in-plane SPPs a light-coupler structure must be integrated in the metal/dielectric interface. Thus, an interesting nanofabrication challenge is to engineer coupling structures that could be done by using an intermediate layer or the metal contact itself. A further fundamental challenge is to realize plasmonic assisted photovoltaic devices that depend weakly on frequency, polarization and angle of incidence. This could be faced by using two-dimensional mesh structures with features much smaller than the wavelength.

2.3.3 Incidence on solar cell performances

Reducing the active-layer thickness by plasmonic light trapping not only reduces costs but also improves the electrical characteristics of the solar cell. First of all, reducing the cell thickness reduces the dark current (I_{01}), causing the open-circuit voltage V_{oc} to increase, as eq. 2.44. Consequently, the cell efficiency rises in logarithmic proportion to the decrease in thickness, and is ultimately limited by surface recombination.

3 Laser Interference Lithography

3.1 Introduction to IL

Depending on structure type (1D/2D/3D) and dimensions, large area plasmonic gratings can be employed in different biological and optoelectronic devices such as biosensors[17], photodetectors[36] or solar cells[35] to satisfy the effort in reaching ever increasing performances. The method of choice to fabricate these highly regular large area structures is Laser Interference Lithography (LIL): interference fringes coming from two or more laser wavefronts pattern periodic geometries on photo-sensitive substrates.

Because of its nature, related to the interference of coherent optical beams, LIL could generate only a limited number of periodic structures. Arbitrary patterns are impossible using interference lithography. For example, the interference of two beams ideally produces a pattern which is periodic in only one dimension, whereas periodicity in more than one dimension requires either more than two interfering beams or more than one exposure. Notwithstanding the limitations, interference lithography is usually the one of the most convenient lithographic option for applications in which periodic patterns are desirable. In this context interference lithography can play its important role in investigating many fundamental problems of nanotechnology avant-gardes: feature sizes possible with LIL (without using masks) are significantly smaller than most other techniques, rivaling techniques that requires a multi-million dollar investment in lithography systems and mask (e.g. EBL or EUV Projection Lithography). A similar discussion could be done in the field of creation of materials and molecules with a precise atomic structure, which has been the domain of chemists for several decades. Only recently, however, an increasing number of bottom-up nanofabrication techniques, e.g. Self Assembling Monolayer, have been applied towards building devices at the molecular scale. However, self-assembled structures, while capable of molecular or even atomic level precision, are incapable of the high-level organization necessary to interact with other systems. The bridge between the molecular scale and the need of long-range order can be made lithographically. For example, combining self-assembly methods with long-range ordering LIL capability would allow nanostructures to be lithographically fabricated in precise positions on a substrate[37], [38]. Furthermore, in the last decade, several methods have been proposed to reduce periodicity variations of interferometric patters to the level of picometers, which could form the basis of a metrology system necessary to any serious nanotechnology endeavor[39], [40].

Thus, IL provides an ideal tool, not just for certain devices, but for investigating current and future lithographic processes. Following the Fourier theory applied to optics, sinusoidal components of different periodicity, or spatial frequencies, are the building blocks of any image[41]. An arbitrary optical imaging systems, such as projection lithography tools, can be characterized by the Fourier formalism understanding how the frequency content of an image is altered from the original input. In addition, photoresist behavior, as well as process parameters such as etch rates of the pattern transfer techniques, often have a marked dependence on spatial frequency (feature size). In this

context, LIL offers a way to simply input single spatial-frequencies, the elementary functions of imaging, so that the lithography process can be learned and understood in a far more general sense than is possible with other techniques. In this regard, LIL is considered a very useful tool for characterizing the lithography processes related to the production of all devices[42].

3.2 Basic Theory of LIL

This chapter will outline the theoretical background on which Laser Interference Lithography is based. However, the theory outlined below starts from very basic considerations about fundamentals of electromagnetism[18], [43].

3.2.1 Electromagnetic waves formalism

The most general form of a travelling wave can be described considering a one-dimensional wave pulse of arbitrary shape from the point of view of a stationary coordinate system. The moving pulse has the mathematical form:

$$y = f(x \pm vt) \tag{3.1}$$

The original shape of the pulse does not vary but is found simply translated along the x-direction by the amount *vt* at time *t*, where *v* is the velocity.
The partial differential equation that is satisfied by all the wave equations 3.1 is obtained employing the chain rule. The equation is:

$$\frac{\partial^2 y}{\partial x^2} = \frac{1}{v^2}\frac{\partial^2 y}{\partial t^2} \tag{3.2}$$

noting that the general form of the wave pulse could be $y = f(\acute{x})$ where $\acute{x} = x \pm vt$.
Thus a general function of t and x is a travelling wave if it is in the form of eq. 3.1 and satisfies eq.3.2.
A particular set of travelling waves are harmonic waves:

$$y = A_{cos}^{sin}[k(x \pm vt)] \tag{3.3}$$

where k and A are constants. *k* is defined as propagation constant.
Where the argument of the sine or cosine, an angle that depends on space and time, is called phase:

$$\varphi = k(x \pm vt) \tag{3.4}$$

These are periodic waves generated by undamped oscillators. The sum of sine and cosine wave functions forms a complete set that can represent, by a linear combination, any actual periodic wave form. Thus combinations of harmonic waves, also called Fourier series, can represent any complicated wave forms, even a series of rectangular pulses or square waves.

Because of the spatial periodicity, all *x* could be increased by the wavelength λ still reproducing the same wave. This is because the argument of the sine function is advanced by 2π

$$A \sin k[(x + \lambda) + vt] = A \sin[k(x + vt) + 2\pi]$$

Thus the propagation constant is defined as:

$$k = \frac{2\pi}{\lambda} \qquad 3.5$$

And, if the wave is viewed from a fixed point, $kvt = 2\pi$ and:

$$v = \lambda \upsilon \qquad 3.6$$

When x and t change together in such a way that φ is constant, the displacement $y = A \sin \varphi$ is also constant. Thus, the condition of constant phase describes the motion of a fixed point on the wave form, which moves with the velocity of the wave. If φ is constant, $d\varphi = 0 = k(dx \pm vdt)$ and $\frac{dx}{dt} = \mp v$ confirming that *v* is the wave velocity, positive (dx direction) when $\varphi = k(x - vt)$. Furthermore, using Euler's formula the harmonic wave could be expressed as:

$$y = Ae^{-i(kx - \omega t)} \qquad 3.7$$

where

$$\begin{aligned} Re(y) &= A \cos(kx - \omega t) \\ Im(y) &= A \sin(kx - \omega t) \end{aligned} \qquad 3.8$$

Eq. 3.7 describes a general set of periodic waves propagating along the x-direction. The harmonic wave equation could further represent a propagation along any direction in space. In the case of plane waves, for a fixed direction, the surfaces of constant phase are family of planes, planar wavefronts.

$$\boldsymbol{\psi} = \boldsymbol{A}e^{-i(\boldsymbol{k}\cdot\boldsymbol{r} - \omega t)} \qquad 3.9$$

Harmonic waves emanating from a point source with spherical wavefronts are described as:

$$\boldsymbol{\psi} = \frac{\boldsymbol{A}}{\boldsymbol{r}} e^{-i(\boldsymbol{k}\cdot\boldsymbol{r} - \omega t)} \qquad 3.10$$

The partial differential equation satisfied by such three dimensional waves is:

$$\frac{\partial^2 \boldsymbol{\psi}}{\partial x^2} + \frac{\partial^2 \boldsymbol{\psi}}{\partial y^2} + \frac{\partial^2 \boldsymbol{\psi}}{\partial z^2} = \frac{1}{v^2}\frac{\partial^2 \boldsymbol{\psi}}{\partial t^2} \qquad 3.11$$

or

$$\nabla^2 \boldsymbol{\psi} = \frac{1}{v^2}\frac{\partial^2 \boldsymbol{\psi}}{\partial t^2} \qquad 3.12$$

The general set of harmonic wave equations can represent the propagation of light. In this case the physical significance of the displacement ψ stands for either the varying of the electric or magnetic fields that together constitute the wave. Therefore, considering that a plane electromagnetic wave is described by harmonic variations of electric and magnetic fields always perpendicular to one another and to the traveling direction $\boldsymbol{k}$, the eq. 3.12 gives the following solutions:

$$\begin{aligned} \boldsymbol{E} &= \boldsymbol{E_0} e^{-i(\boldsymbol{k}\cdot\boldsymbol{r}-\omega t)} \\ \boldsymbol{B} &= \boldsymbol{B_0} e^{-i(\boldsymbol{k}\cdot\boldsymbol{r}-\omega t)} \end{aligned} \qquad 3.13$$

3.2.2 Superposition - interference

Equation 3.13 defines the displacements of the electric and magnetic fields of a plane wavefront having a spatially uniform intensity distribution. However, during Laser Interference exposures each point of the sample sees the overlapping of two of more waves coming from a (stable and coherent) continuous wave laser. In other words, a superposition of plane waves that arrives at any points of the exposure field. In such situation, the evaluation of the resulting electric field displacement is obtained by the sum of the components considering the well known superposition principle.

Let us consider $\boldsymbol{\psi}_1$ and $\boldsymbol{\psi}_2$ as two independent solutions of equation 3.12, then the linear combination $\boldsymbol{\psi} = a\boldsymbol{\psi}_1 + b\boldsymbol{\psi}_2$, where a and b are constants, is also a solution. Thus, the superposition of electromagnetic waves may be expressed in terms of linear combination vectors:

$$\boldsymbol{E} = \sum_{\boldsymbol{i}} \boldsymbol{E}_i \qquad 3.14$$

and the same is valid for magnetic fields.

Considering now two overlapping monochromatic plane waves $\boldsymbol{E}_1$ and $\boldsymbol{E}_2$ directed as explained in Fig. 3.1 that differ by the phase term $\Delta\phi = \pi_2 - \pi_1$:

$$\begin{aligned} \boldsymbol{E}_1(\boldsymbol{r}) &= \boldsymbol{E}_1 e^{j(\boldsymbol{k}\cdot\boldsymbol{r}-\omega t + \pi_1)} \\ \boldsymbol{E}_2(\boldsymbol{r}) &= \boldsymbol{E}_2 e^{j(\boldsymbol{k}\cdot\boldsymbol{r}-\omega t + \pi_2)} \end{aligned} \qquad 3.15$$

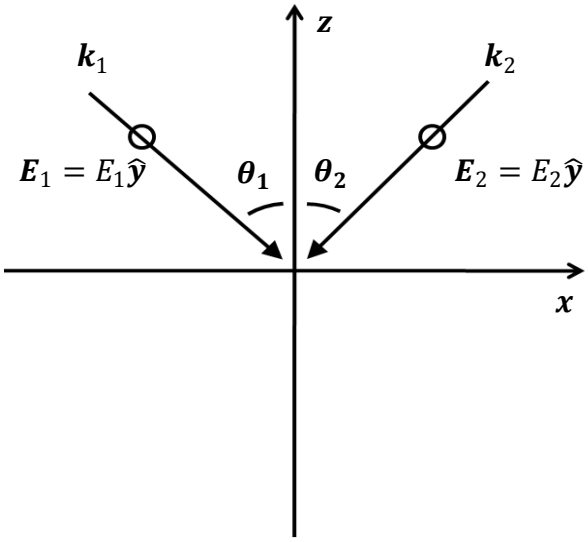

Fig. 3.1: scheme of two overlapping monochromatic TE plane waves $\boldsymbol{E}_1$ and $\boldsymbol{E}_2$.

The electric field for both waves is oriented along the $\hat{\boldsymbol{y}}$ direction, and has magnitude E_0. The phase offset of each wavefront (π_1, π_2) is specified with respect to the origin. At the surface of the sample ($z = 0$) the waves intersect to produce a regular interference pattern. Thus, the total field is given by:

$$\begin{aligned}\boldsymbol{E} = \boldsymbol{E}_1 + \boldsymbol{E}_2 &= E_0\hat{\boldsymbol{y}}e^{j(\boldsymbol{k}_1\cdot\boldsymbol{r} - \omega t + \pi_1)} + E_0\hat{\boldsymbol{y}}e^{j(\boldsymbol{k}_2\cdot\boldsymbol{r} - \omega t + \pi_2)} \\ &= 2E_0\hat{y}e^{\frac{j}{2}(\boldsymbol{k}_1\cdot\boldsymbol{r} + \boldsymbol{k}_2\cdot\boldsymbol{r} + \pi_1 + \pi_2 - 2\omega t)} \cdot \\ &\cdot \cos\left(\frac{1}{2}(\boldsymbol{k}_1\cdot\boldsymbol{r} - \boldsymbol{k}_2\cdot\boldsymbol{r} + \pi_1 - \pi_2)\right) \\ &= 2E_0\hat{y}\left[e^{\frac{j}{2}(k_{x1}x + k_{y1}y - k_{z1}z - k_{x2}x + k_{y2}y - k_{z2}z + \pi_1 + \pi_2 - 2\omega t)}\right] \cdot \\ &\cdot \cos\left(\frac{1}{2}\left(k_{x1}x + k_{y1}y - k_{z1}z - k_{x2}x - k_{y2}y + k_{z2}z + \pi_1\right.\right. \\ &\left.\left. - \pi_2\right)\right)\end{aligned} \qquad 3.16$$

The resulting intensity at a given spatial point $\boldsymbol{P}$, which is related to the image recorded by the resist in a lithographic exposure, is proportional to $|\boldsymbol{E}|^2$ and follows the eq. 3.17 [18]:

$$I = |\boldsymbol{E}|^2 = \boldsymbol{E}_1^2 + \boldsymbol{E}_2^2 + 2\boldsymbol{E}_1 \cdot \boldsymbol{E}_2^* \qquad 3.17$$

thus results:

$$I = I_1 + I_2 + [(\boldsymbol{E}_1(r) \cdot \boldsymbol{E}_2{}^*(r)) + (\boldsymbol{E}_2(r) \cdot \boldsymbol{E}_1{}^*(r))] \\ = I_1 + I_2 + 2\sqrt{I_1 I_2}(\hat{\boldsymbol{e}}_1 \cdot \hat{\boldsymbol{e}}_2)\cos[(\boldsymbol{k}_1 - \boldsymbol{k}_2) \cdot \boldsymbol{r} + \Delta\phi] \quad 3.18$$

and

$$I = 2\sqrt{I_1 I_2} \cdot \\ \cdot \left[1 + \cos\left((k_{x1} + k_{x2})x + (k_{y1} - k_{y2})y + (-k_{z1} + k_{z2})z + \pi_1 - \pi_2\right)\right] \quad 3.19$$

Since the average energy dose released to substrate can be varied by changing the exposure time, the additive term $\sqrt{I_1 I_2}$ could be neglected in our case. Furthermore, note that the phase difference between the interfering beams, $\Delta\phi = \pi_1 - \pi_2$, simply shifts the pattern and could be neglected for simplicity.
Both incident waves propagate on the x-z plane, then $k_{1y} = k_{2y} = 0$; referring to the figure, $k_{x1} = k\ sin\ \theta_1$ and $k_{x2} = k\ sin\ \theta_2$, where $k = {}^{2\pi}/_{\lambda}$.
Thus, at the plane $z = 0$, the aerial image is described by:

$$I = 2\sqrt{I_1 I_2}\cos[k(sin\ \theta_1 + sin\ \theta_2)x \quad 3.20$$

Eq. 3.18 reveals one of the most important consequences of the simultaneous propagation of two electromagnetic plane waves with same frequency in the same material. The intensity of the total wave is not only equal to the sum of the intensities of the individual waves but consists also of one additional trigonometric component called interference term. This term cause the intensity to depend from the position ***r***. In conclusion, the superposition of electromagnetic plane waves creates a non homogeneous distribution of energy in space.

3.2.3 Periodicity of Interference Fringes

From eq. 3.18, we know that the interference pattern for two plane-waves is sinusoidal. The maxima and minima of this sinusoidal pattern are called *fringes*. Let the difference between the wavevectors of the two interfering beams be called the fringe-vector, $\vec{k}_f$.

$$\boldsymbol{k}_f = \boldsymbol{k}_1 - \boldsymbol{k}_2 = k_{fx}\hat{x} + k_{fy}\hat{y} + k_{fz}\hat{z} \quad 3.21$$

If we define the direction of $\boldsymbol{r}$ parallel to the fringe vector, then the spatial-phase is:

$$\Phi = |\mathbf{k}_\mathrm{f}|\mathrm{r} \quad 3.22$$

The spatial periodicity P_f of the interference fringes can now be defined eq. 3.23.

$$\mathrm{P_f} = \frac{2\pi}{|\boldsymbol{k}_f|} \quad 3.23$$

Consider the case where the coordinate axes are defined such that the fringe vector $\boldsymbol{k}_f$, and hence the direction $\boldsymbol{r}$, are parallel to one of the unit axes, for example the $\hat{\boldsymbol{x}}$ axis. This is shown in Fig. 3.2. Under the monochromatic condition of $|\vec{k}_1| = |\vec{k}_2|$, the vector components are defined $k_{1x} = -k_{2x}$, $k_{1y} = k_{2y} = 0$ and $k_{1z} = k_{2z}$. Therefore $\vec{k}_f = 2k_{1x}\hat{x}$. Substituting this result, along with $k = |\boldsymbol{k}| = \frac{2\pi}{\lambda}$, into eq. 3.23, we get

$$\mathrm{P_f} = \frac{\lambda|\mathrm{k_1}|}{2k_{1x}} \qquad 3.24$$

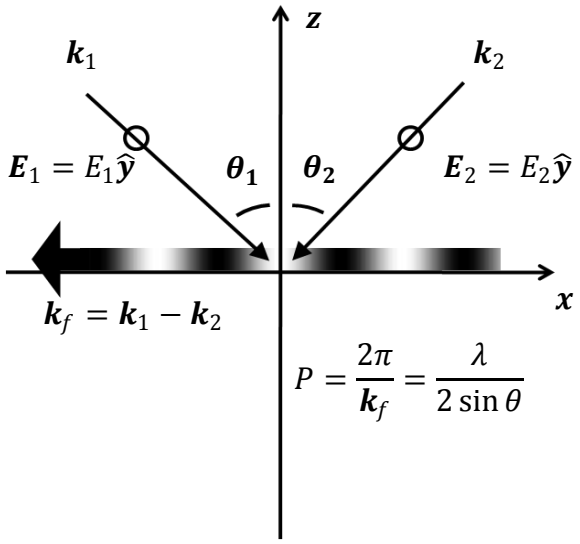

Fig. 3.2: fringe periodicity of an interference pattern formed by two monochromatic TE plane waves $\boldsymbol{E}_1$, $\boldsymbol{E_2}$ along the direction of the fringe vector $\boldsymbol{k}_f$. When $\theta_1 = \theta_2$ the grating pitch is $P = \frac{2\pi}{k_f} = \frac{\lambda}{2\sin\theta}$.

Defining the angle between the vectors $\vec{k}_1$ and $\vec{k}_2$ as 2θ, it can be shown that $\sin(\theta) = \frac{k_{1x}}{|\vec{k}_1|}$. Thus, the periodicity P_f of the interference fringes can be defined in terms of the half-angle between the interfering beams.

$$\mathrm{P_f} = \frac{\lambda}{2\sin(\theta)} \qquad 3.25$$

Eq. 3.25 represents the well known formula for the periodicity of the fringe pattern of two interfering beams. Although the coordinate axes were defined in a specific way, eq. 3.25 is valid for any arbitrary coordinate system.

3.2.4 Visibility of interference fringes

The ability to distinguish the high and low intensity regions can be quantified with a parameter V known as contrast, or visibility, defined in eq. 3.26.

$$V = \frac{I_{max} - I_{min}}{I_{max} + I_{min}} \tag{3.26}$$

When two coherent plane-waves interfere, the maximum and minimum intensities can be found by setting the value of the cosine term in eq. 3.18 to 1 (or -1), respectively.

$$\begin{aligned} I_{max} &= I_1 + I_2 + 2\sqrt{I_1 I_2} \\ I_{min} &= I_1 + I_2 - 2\sqrt{I_1 I_2} \end{aligned} \tag{3.27}$$

Destructive and Constructive interference is complete when $I_1 = I_2 = I_0$. In this case eq.s 3.27 give $I_{max} = 4I_0$ and $I_{min} = 0$. In all the cases when the two interfering beams have different intensities there is not complete dark and bright fringes. This behavior could be evaluated by substituting the above equations back into eq. 3.26 and plotting it versus the relative intensity ratio I_1/I_2 (or mismatch):

$$V = \frac{2\sqrt{I_1 I_2}}{I_1 + I_2} \tag{3.28}$$

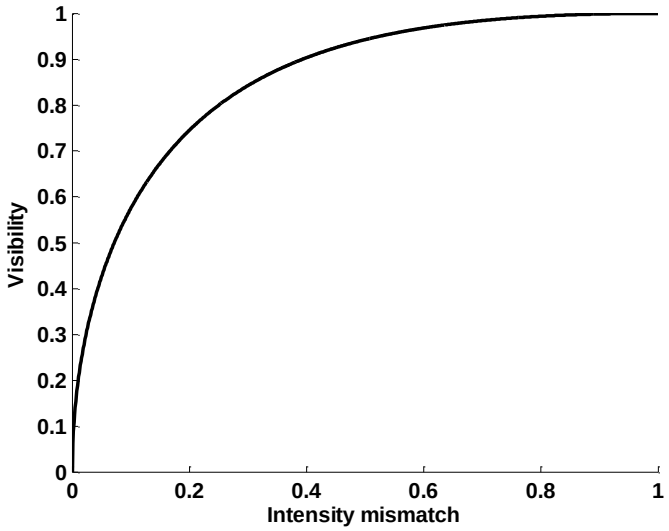

Fig. 3.3: Fringe visibility as a function of the intensity mismatch of the two interfering beams.

Fig. 3.3 shows how the fringe visibility reaches its maximum when the intensity of the two beams is equal. However, almost perfect contrast can still be achieved for beams with a moderate intensity mismatch.

3.2.5 Polarization

Fringe visibility is markedly affected by the two interfering beam polarization. Previous considerations have been done assuming that considering that the electric fields of the two interfering waves were parallel and perpendicular to the plane defined by the two beams, TE polarization. This is the optimal configuration for achieving high-contrast

interference fringes, as the dot-product $\hat{e}_1 \cdot \hat{e}_2$ in eq. 3.18 is always equal to unity and can be dropped from the analysis. A more complex situation occurs for the TM (transverse-magnetic) polarization, when the electric field vectors are parallel to the plane-of-incidence.

Let us consider two TM polarized beams with intensity $I_1 = I_2 = I_0$ and no phase mismatches. Thus, eq. 3.18 can be simplified as:

$$\mathrm{I} = 2I_0[1 + (\hat{\boldsymbol{e}}_1 \cdot \hat{\boldsymbol{e}}_2)\cos(\boldsymbol{k}_\mathrm{f} \cdot \mathbf{r})] \qquad 3.29$$

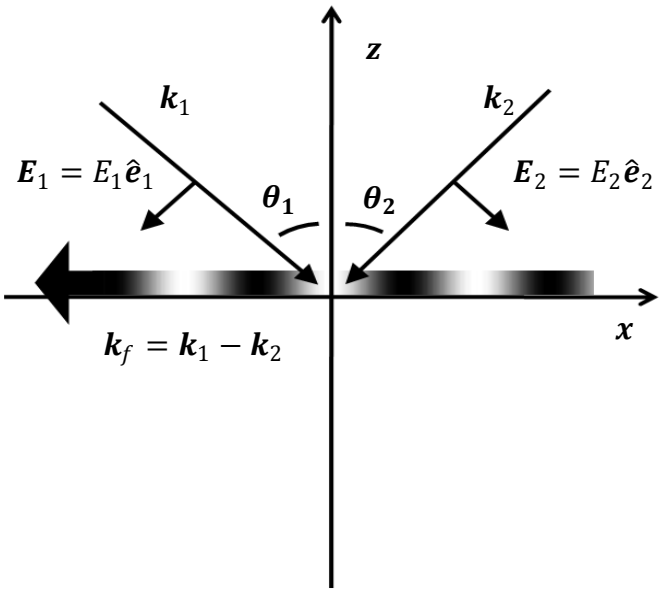

Fig. 3.4: Interference of TM polarized plane-waves. The electric field vector is parallel to the plane defined by the interfering beams.

Note that when interfering beams have orthogonal polarizations, the sinusoidal modulating term goes to zero and the intensity is constant and equal to the sum intensity of the two beams. In general, when the interfering plane waves have polarizations that differ by an angle of 2θ the product of versors is

$$\hat{\boldsymbol{e}}_1 \cdot \hat{\boldsymbol{e}}_2 = (-\cos\theta i - sin\theta j)(\cos\theta i - sin\theta j) = -\cos 2\theta \qquad 3.30$$

Then $I_{max\,,TM}$ and $I_{min\,,TM}$ are found by setting the spatial phase argument $|\mathbf{k}_\mathrm{f}|\mathrm{r} = \pm\pi$.

$$\begin{aligned} I_{max\,,TM} &= 2I_0(1 + |\cos 2\theta|) \\ I_{min\,,TM} &= 2I_0(1 - |\cos 2\theta|) \end{aligned} \qquad 3.31$$

Thus the visibility is:

$$\mathrm{V_{TM}} = |\cos 2\theta| \qquad 3.32$$

In practical situations, considering two monochromatic waves of equal intensity, following eq.s 3.28 and 3.32: $V_{TM} \leq V_{TE}$.

3.2.6 Coherence

Consider the electric field of an electromagnetic wave at a given point P, at times t and $t + \tau$. If the phase difference of the field sampled with a time delay τ remains the same for any time t, there is a time coherence over a time τ. If this occur for any value of τ the electromagnetic wave is said to have perfect temporal coherence. If this occur for a time delay τ such that $0 < \tau < \tau_0$, the wave is said to have partial temporal coherence, with coherence time equal to τ_0. Fig. 3.5 shows a sinusoidal electric field undergoing phase jumps at time intervals equal to τ_0.

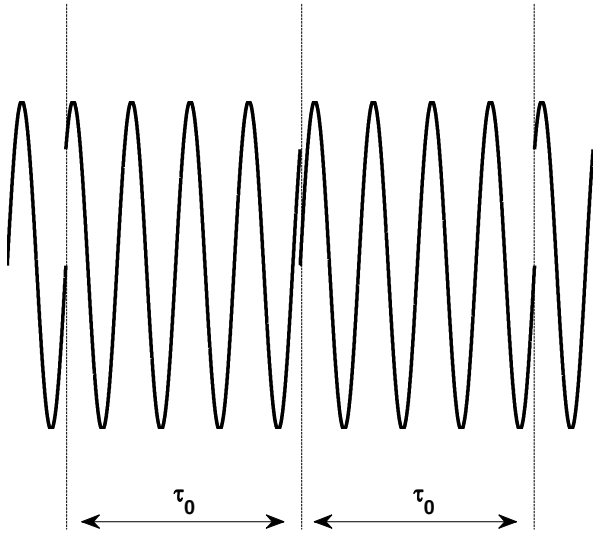

Fig. 3.5: example of an electromagnetic wave having a coherence time of τ_0

Following a more analytic formalism, suppose that an electromagnetic wave is measured at some point $\boldsymbol{r}_1$ in a time interval from 0 to T. The product of the fields at the same point r1 at time t_1 and t_2 is

$$E(\boldsymbol{r}_1, t_1)\, E^*(\boldsymbol{r}_1, t_2) \qquad 3.33$$

Trying to measure the product of eq. 3.33 several times, the ensemble average can be calculated as the first order correlation function:

$$\Gamma'(\boldsymbol{r}_1, \boldsymbol{r}_1, t_1, t_2) = \langle E(\boldsymbol{r}_1, t_1)\, E^*(\boldsymbol{r}_1, t_2) \rangle \qquad 3.34$$

Note that eq. 3.33 is expressed in a general form since it can be applied to stationary or non stationary beams. However, considering the basic condition of cw laser, the light source is stationary, thus the ensemble average depends only on the time interval $\tau = t_2 - t_1$and not on particular times.

$$\Gamma'(\boldsymbol{r}_1, \boldsymbol{r}_1, t_1, t_2) = \Gamma(\boldsymbol{r}_1, \boldsymbol{r}_1, \tau) = \langle E(\boldsymbol{r}_1, t+\tau)\, E^*(\boldsymbol{r}_1, t)\rangle \qquad 3.35$$

If, besides being stationary, the beam is also ergodic, then the ensemble average is equal to the time average:

$$\Gamma'(\boldsymbol{r}_1, \boldsymbol{r}_1, \tau) = \lim_{T\to\infty} \frac{1}{T}\int_0^T E(\boldsymbol{r}_1, t+\tau)\, E^*(\boldsymbol{r}_1, t)dt \qquad 3.36$$

The first-order correlation function Γ' can be normalized representing the degree of correlation between fields:

$$\gamma'_\tau = \frac{\langle E(\boldsymbol{r}_1, t+\tau)\, E^*(\boldsymbol{r}_1, t)\rangle}{\langle E(\boldsymbol{r}_1, t)\, E^*(\boldsymbol{r}_1, t)\rangle^{1/2}\langle E(\boldsymbol{r}_1, t+\tau)\, E^*(\boldsymbol{r}_1, t+\tau)\rangle^{1/2}} \qquad 3.37$$

For a stationary beam the two ensemble averages in the denominator are equal. γ' and $|\gamma'|$ are called respectively *complex degree of temporal coherence* and *degree of temporal coherence*, giving the degree of correlation between of fields evaluated at the same point $\boldsymbol{r}_1$ at two instants separated by the time interval τ. The function γ' has the following properties: (1) $|\gamma'(\boldsymbol{r}_1, \boldsymbol{r}_1, \tau)| \leq 1$ and $\gamma' = 1$ when $\tau = 0$; (2) $\gamma'(\boldsymbol{r}_1, \boldsymbol{r}_1, -\tau) = \gamma'^*(\boldsymbol{r}_1, \boldsymbol{r}_1, \tau)$. Thus a beam has perfect temporal coherence when $|\gamma'(\boldsymbol{r}_1, \boldsymbol{r}_1, \tau)| = 1$ for any τ (for a cw beam this happens when both amplitude and phase has no fluctuations). The complete absence of temporal coherence occurs when $|\gamma'(\boldsymbol{r}_1, \boldsymbol{r}_1, \tau)| \to 0$ for $\tau > 0$ (this is the case of thermal light sources with very large bandwidth). In more common situations, $|\gamma'(\boldsymbol{r}_1, \boldsymbol{r}_1, \tau)|$ is a decreasing symmetric function of τ.

The delay for which $|\gamma'(\boldsymbol{r}_1, \boldsymbol{r}_1, \tau)| = 1/2$ can be defined as the coherence time τ_{co}. For a perfectly coherent wave $\tau_{co} = \infty$ and for the opposite case of totally incoherent beam $\tau_{co} = 0$. The coherence length is $L_c = c\tau_{co}$.

A similar discussion can be done for the description of the concept of spatial coherence. Consider two points P_1 and P_2 of the same wavefront at time $t_0 = 0$ and the corresponding electric fields at these two points. The difference between phases of $E_1(P_1, t_0)$ and $E_2(P_2, t_0)$ is zero by definition. If, fixed P_1 and P_2, $\Delta\varphi = 0$ at any time there is perfect coherence between the two points. If this happens for any point of the wavefront there is a perfect spatial coherence. Actually, defined a point P_1, only the locus of points that lies in some finite area around it have good phase correlation. In this case there is a partial spatial coherence and an area of coherence $S_c(P)$ can be defined.

We can also define the corresponding normalized function:

$$\gamma'_s = \frac{\langle E(\boldsymbol{r}_1, t)\, E^*(\boldsymbol{r}_2, t)\rangle}{\langle E(\boldsymbol{r}_1, t)\, E^*(\boldsymbol{r}_1, t)\rangle^{1/2}\langle E(\boldsymbol{r}_2, t)\, E^*(\boldsymbol{r}_2, t)\rangle^{1/2}} \qquad 3.38$$

3.2.7 Partial coherence and fringe visibility

In real situation, two monochromatic waves interfere with a finite coherence time if compared to Optical Path Difference (OPD). In order to evaluate what is the relation between coherence time and OPD it is useful to re-formulate equation 3.18 in a different way taking into account the electric fields at the same point P and the definition of complex degree of coherence:

$$\begin{aligned} I &= I_1 + I_2 + \langle \boldsymbol{E}_1(t) \cdot \boldsymbol{E}_2{}^*(t+\tau)\rangle + \langle \boldsymbol{E}_1{}^*(t) \cdot \boldsymbol{E}_2(t+\tau)\rangle \\ &= I_1 + I_2 + 2Re\{\langle \boldsymbol{E}_1{}^*(t) \cdot \boldsymbol{E}_2(t+\tau)\rangle\} \\ &= I_1 + I_2 + 2\sqrt{I_1 I_2}Re\{\gamma'(\tau)\} \end{aligned} \qquad 3.39$$

The function $\gamma'(\tau)$ is now the core of the interference term. It is a function of τ. In a further step the term $Re\{\gamma'(\tau)\}$ could be expanded by separating the mutual coherence function into its magnitude and phase components, where ϕ is the phase argument. Thus the above equation simplifies to

$$I = I_1 + I_2 + 2\sqrt{I_1 I_2}|\gamma'(\tau)|\cos(\phi) \qquad 3.40$$

According to the assumptions of beams of equal intensity, we can compute the values of I_{max} and $I_{\min}$ and therefore the value of fringe visibility that is equal to the magnitude of the correlation function as a measure of the degree of coherence:

$$V = |\gamma'(\tau)| \qquad 3.41$$

3.3 Laser Interference Lithography Systems

We have seen before that the superposition of electromagnetic plane waves generates a non homogeneous distribution of energy in space. Laser Interference Lithography is basically the method in which such energy distributions are registered in a photoresist material and usually transferred to the substrate. Different kinds of experimental setups that makes use of reflective or diffractive optics have been proposed in order to pattern nanostructures by means of Interference Lithography. However, the most intuitive way to generate interference patterns consists in splitting a laser beam in two branches of almost the same intensity and then recombine the two arms in the so called Mach-Zehnder configuration.

Before each beam of light reaches the substrate they pass through a spatial filter to eliminate aberrations due to imperfect, dirty, or damaged optics, or due to variations in the laser gain medium. However, accurate positioning and precise alignment of optics other than fringe stabilization electronics are required to produce a single grating structure by this interferometer. Furthermore, when the grating periodicity has to be changed, a complete and time-consuming re-adjustment of the whole optical setup has to be pursued, which limits the usability of Mach-Zehnder configuration in many cases.

A simpler configuration, known as Lloyd's-Mirror Interferometer, was introduced in the 1830's by Humphrey Lloyd (1800-1881) under the assumption that direct interference

might be shown by the mutual action of direct and reflected light. He was the first that introduced the use of a mirror to generate interference [44]. In 1967 P.H Langenbeck [45] was one of the first that used a laser as source of Lloyd's interferometer for flatness testing over a large surfaces. In the last 40 years, the high-coherence and stability of a modern laser allow to use the Lloyd's interferometer system to produce large areas gratings of the finest possible fringes to be employed in many applications like optics, plasmonics, magnetism, SAM .

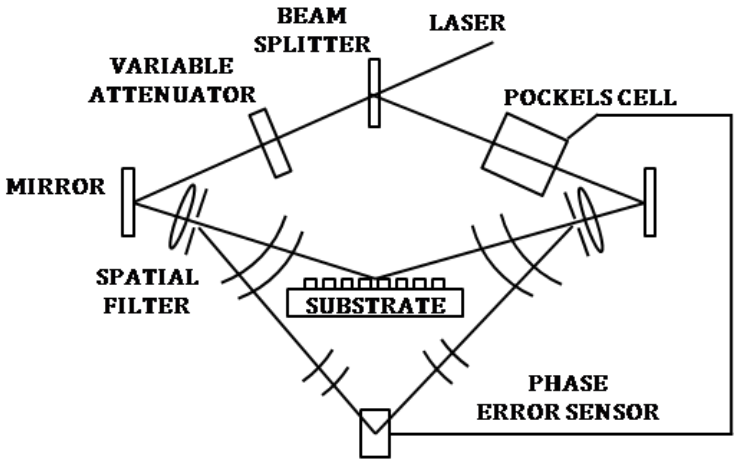

Fig. 3.6: Mach-Zehnder interferometer schematic. The laser beam is split into two arms, spatially filtered and expanded. The two arms interfere on a resist coated substrate. The system has a fringe locking feedback system.

The system that was developed by me in our laboratory is a LIL setup based on Lloyd's mirror configuration (Fig. 3.7). A cw 50mW Helium Cadmium (HeCd) laser emitting a TEM_{00} single mode at 325nm was used as light source. This laser has a 30 cm long coherence length in the near-UV wavelength range in a more usable and robust package and at a lower cost than other cw options, such as argon-ion lasers. Although the HeCd has a relatively weak output power, this does not limit important parameters such as the minimum pitch of the fringes or the size of the exposed area, while throughput is not an important specification in the research environment. Furthermore, as stated above, in any interference scheme, the TE polarization will produce higher contrast fringes than the TM. This implies that all the steering mirrors between the laser and the Lloyd's stage must be arranged to ensure that the polarization incident on the substrate is TE (electric field parallel to the substrate).

Following the optical path, after the steering mirrors, the beam reaches a spatial-filter that allows high spatial frequency noise to be removed from the original one. After a 2 m long free-space propagation, the expanded laser beam illuminates both the sample and a mirror perpendicular to it. Thus, interference between the light coming from the spatial filter and its mirror image forms a standing wave pattern on the photosensitive substrate. Fig. 3.8 shows the working principle schematic view of a Lloyd's mirror interferometer used for lithography. It simply consists in a mirror placed perpendicular to a sample holder and illuminated with a single beam. Thus, the beam splitter is

replaced by a mirror that becomes the plane of symmetry and the unique light source is duplicated by a virtual one.

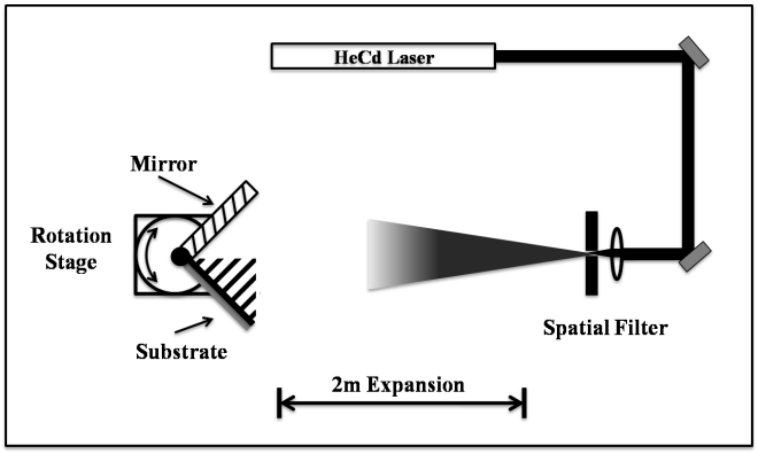

Fig. 3.7: Schematic design of a Lloyd's mirror Laser Interference Lithography setup. The laser beam is spatially filtered and expanded and, when the wavefront could be approximated to that of a pure propagating plane wave, it reaches both the mirror and sample stage. The superposition of the direct and reflected beams generate the desired interference pattern. By rotating the interferometer it is possible to control the angle of incidence and therefore the fringe periodicity.

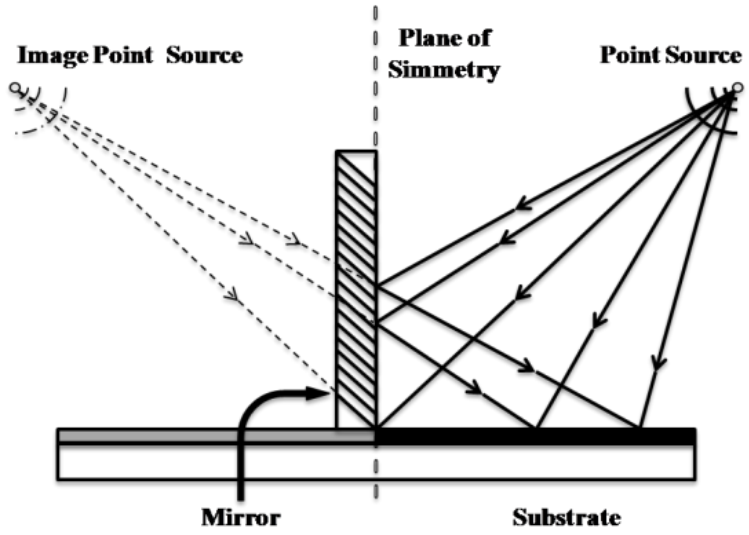

Fig. 3.8: Lloyd's mirror interferometric lithography working principle. The surface of the mirror becomes the plane of symmetry with one image source as virtual source.

The need of a large beam expansion is a sort of compromise (a trade-off solution) [42]. As a Gaussian beam expands, it changes in three ways. The irradiance of the beam decreases resulting in increased exposure times, thus increasing the incidence of system vibrations and beam instabilities on the final result. The diameter of the beam increases, creating a more uniform intensity distribution over the exposed area. Fig. 3.9 shows a beam width of 43.5 cm ($1/e^2$) at the sample holder position guaranties that a 10 cm wafer could be illuminated with a maximum exposure dose variation of 10%. Finally, the radius of the phase front increases. This means that the beam could be more closely

approximated to a plane-wave over the exposure area. Thus, maximizing the beam expansion, the exposed grating will have a more linear spatial phase and a more uniform linewidth over the sample surface, at the expense of a longer exposure time.
The Lloyd's system we have designed allows to hold up to 10 cm diameter samples (4" wafers). The wafer chuck can also rotate around the sample normal allowing multiple exposure at different angles. The system has been designed to allow also fine optical alignments with respect to the optical axis. In particular, both the mirror and the sample are held together in a system having translational and rotational degrees of freedom while a rigid mechanical connection between the mirror and the wafer chuck prevents phase distortions and instabilities. Furthermore, the possibility to translate the sample stage in two directions allows a fine positioning of the system where the Gaussian beam distribution reaches its maximum, giving the best condition in terms of beam intensity and uniformity. On the other hand, the sample stage rotation around the vertical axis (8mrad resolution) allows a fine setting of the fringes periodicity.

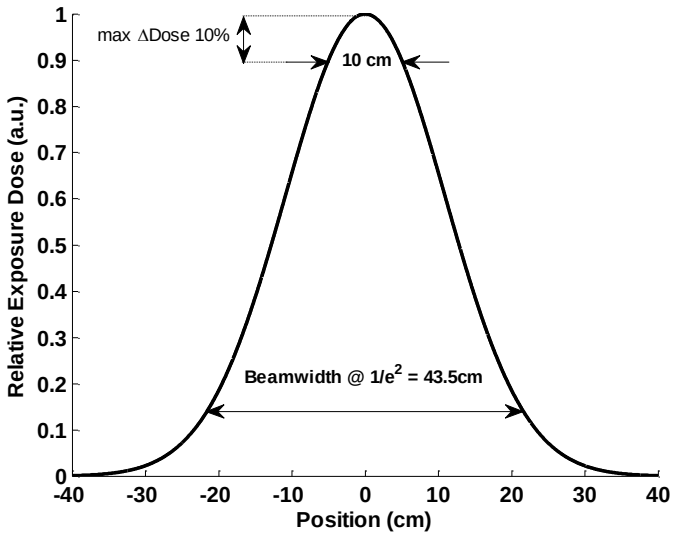

Fig. 3.9: Gaussian beam expansion needed in order to illuminate a 10cm large sample with <10% of dose variation.

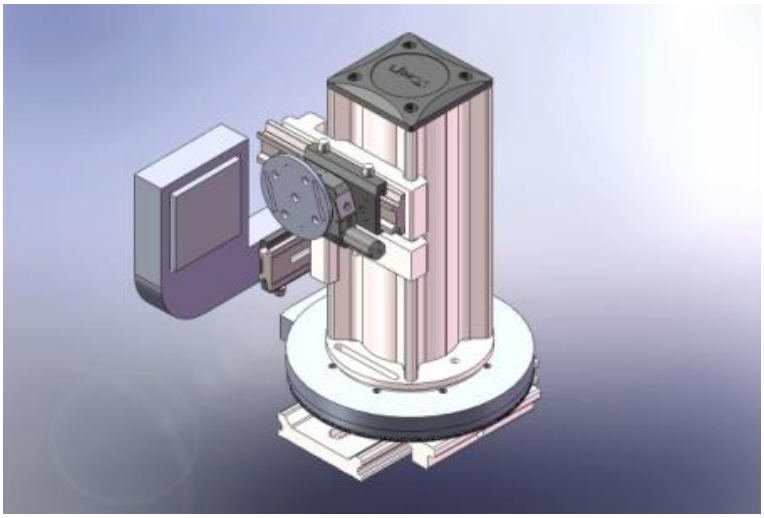

Fig. 3.10: Lloyd's mirror interferometer design.

3.4 Plasmonic gratings nanofabrication processes by means of LIL

3.4.1 Fabrication of sinusoidal plasmonic gratings

The aim of this paragraph is to outline the main aspects involved in the fabrication of sinusoidal shaped plasmonic gratings by means of LIL and their scientific function. This particular surface patterning method has been employed to fabricate SPP optical couplers and, at the same time, to integrate them in large area SPP devices as biodetectors or solar cells[46].

In order to understand the basic principles of this method, we are going to describe the particular fabrication process of a biosensitive architecture which was made by nanopatterning a metal substrate and by tethering on top of the surface an analyte-specific probe (biorecognizing or sensing element). A simple schematic picture of the device is drawn in Fig. 3.11.

Surface patterning has been realized by using LIL over large area samples (typically 2x2 cm^2 large). An accurate optimization of the exposure parameters has been performed in order to reach a fine control of any geometric parameter[47]. A tandem exposure method[48] has been here adopted to obtain an accurate control of the amplitude of the sinusoidal profile.

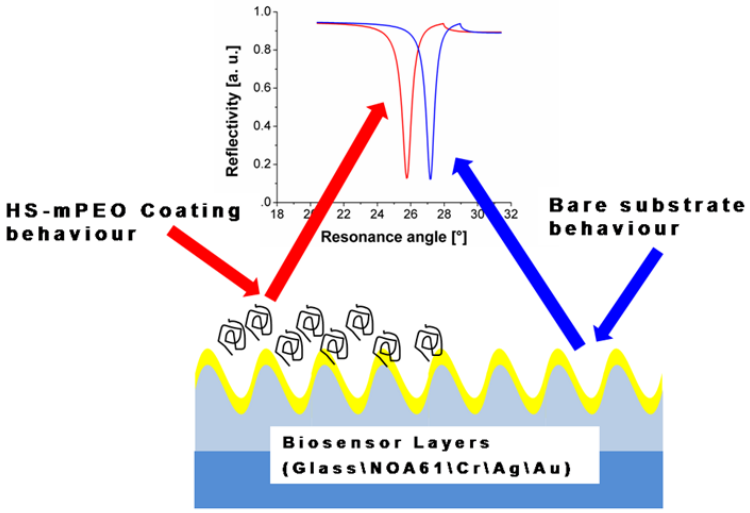

Fig. 3.11: biodevice scheme. When any molecular species binds on the metal surface of the sensor, a change of the refractive index next to the surface induces an angular shift of the reflectivity dip.

Different samples have been realized and their morphological characterization has been performed by Atomic Force Microscopy (AFM). A lot of care have been posed to achieve a nearly perfect sinusoidal profile in order to maximize the SPP coupling.

3.4.1.1 Process design

In principle, a plasmonic biosensor could be obtained simply by coating the nanopatterned photoresist gratings with specific noble metals, such as silver and gold, over a few nanometers of chromium or titanium as adhesion layer, followed by a

suitable biomolecular probe surface functionalization. Unfortunately many biomolecular surface functionalization methods involve the use of organic solvents that degrade the photoresist resin. To avoid this problem we have adopted an approach based on the (double) replica of a mold to produce thiolene resin copies of the gratings by using intermediate PDMS molds. Commercial thiolene resin NOA61 was used (Norland Optical Adhesives) exploiting its relatively good resistance to organic solvents. Surface patterning is finally followed by the metal deposition processes. Thus, a bilayer of Au/Ag is evaporated over a few nanometers of Cr used as adhesion layer. The bio-recognizing layer is further obtained by the deposition of a single monolayer of thiolated polyethylene oxide (M_w 2000).

The optical response of multilayer metallic gratings strictly depends on the geometrical and physical properties of the plasmonic stack: period and amplitude of the sinusoidal modulation, dielectric constants and thickness of each layer. A numerical code, based on Chandezon's method[49], has been implemented in order to compute the optical response of metallic gratings and to provide proper windows of process for the design and nanofabrication of optimized structures. Reflectivity dip amplitude and FWHM have been considered as parameters for the estimation of grating quality and performance: a deeper and narrower resonance dip corresponds to a better coupling of the incident light with SPP modes and it assures a greater sensitivity in sensing applications.

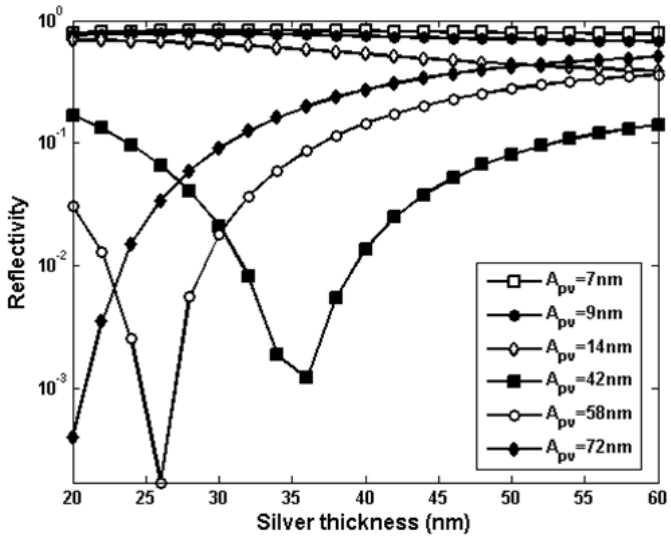

Fig. 3.12: design analysis for the device geometric parameter optimization. Simulation of reflectivity minima as a function of silver layer thickness for different grating amplitudes (7 - 9- 14 - 42 - 58 - 72 nm), fixed period λ = 500 nm and coating gold layer 7 nm-thick, incident wavelength λ = 675 nm.

For a fixed 500 nm period of the sinusoidal modulation, reflectivity minimum has been studied as a function of the silver thickness for different values of grating amplitude. A gold coating layer of 7 nm and an underlying chromium layer of 5 nm have been considered thick enough to respectively prevent silver oxidation and promote the adhesion to the substrate: their thickness has been kept fixed during silver layer

optimization. Some results of the optimization analysis are collected in Fig. 3.12: simulated reflectivity minima as a function of silver thickness in the range 20-60 nm are reported for several grating amplitude values: (A_{pv}) 7 - 9 - 14 - 42 - 58 - 72 nm. These values come from a (20%-40%-60%-80%-85%-100%) 2-beams/total dose partitioning according to the tandem exposure LIL method[48] (see the section below for details). As Fig. 3.12 shows, for grating amplitudes beyond a critical limit, a silver thickness that optimizes the reflectivity depth exists. In our case, we decided to set and calibrate the lithographic process in order to pattern the resist surface with a modulation of 42 nm (80% of 2-beams dose). This choice establishes an optimized silver thickness around 37 nm and assures a good tolerance in silver evaporation since the reflectivity minimum does not rise above 0.01 for almost the whole range 30-40 nm.

3.4.1.2 The control of periodicity

The ability to accurately set the periodicity of the exposed grating is dependent on the accuracy and repeatability of the whole system. Two conditions must be fulfilled to guarantee the right alignment. One is that the mirror is truly mounted perpendicular to the substrate[50]. The other is that the interferometer axis defined by the intersection of the mirror surface and the substrate surface coincides with the axis of rotation. In a Lloyd's mirror interferometer, when the angle between the mirror and the wafer chuck is not 90°, the expected symmetry is broken[42].

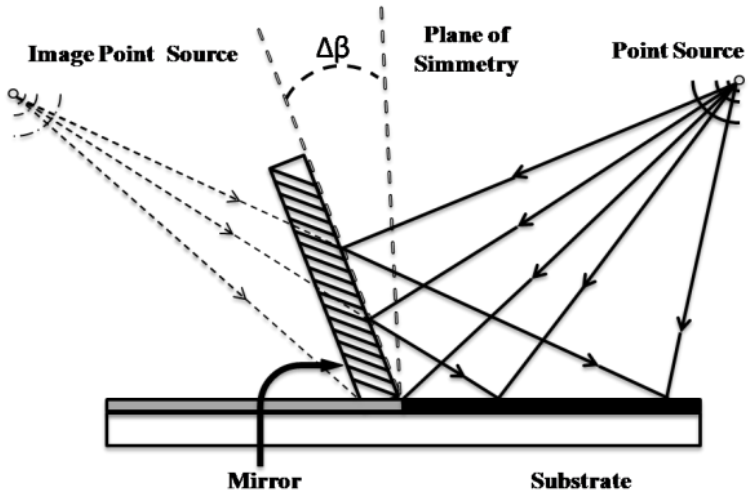

Fig. 3.13: Lloyd's interferometer working principle when the mirror is misaligned.

The consequence is that the virtual source is placed in a different position relative to the substrate than the real source, i.e. a different angle of incidence on the substrate for the reflected beam while the direct beam remains unchanged. The fringes will not form perpendicular to the substrate, and their periodicity will change. The fringe period recorded on the substrate P_s will be the projection of the new fringe period $P_{\theta+\Delta\beta}$ into the substrate plane. For a mirror angle which is equal to $\beta = 90° + \Delta\beta$, the angle of inclination of the fringes will also be $\Delta\beta$.

$$P_s = P_{\theta+\Delta\beta}\frac{1}{cos(\Delta\beta)} = \frac{\lambda}{2\sin(\theta+\Delta\beta)cos(\Delta\beta)} \quad 3.42$$

For small deviations Δβ of the mirror from normal, the cosine term can be approximated as unity, leaving the effect of the mirror misalignment as equivalent to a calibration error. That is, the actual interference angle will be slightly different from the expected interference angle by a constant amount. In practical terms, this means that the angle Δβ should be somewhat less than the angular accuracy of the stage Δθ.

$$\Delta\beta < \frac{\Delta\theta}{\mathbf{2}} \quad 3.43$$

Large values of mirror misalignment, $\Delta\beta > 1°$, cause a larger offset that has to be taken into account.

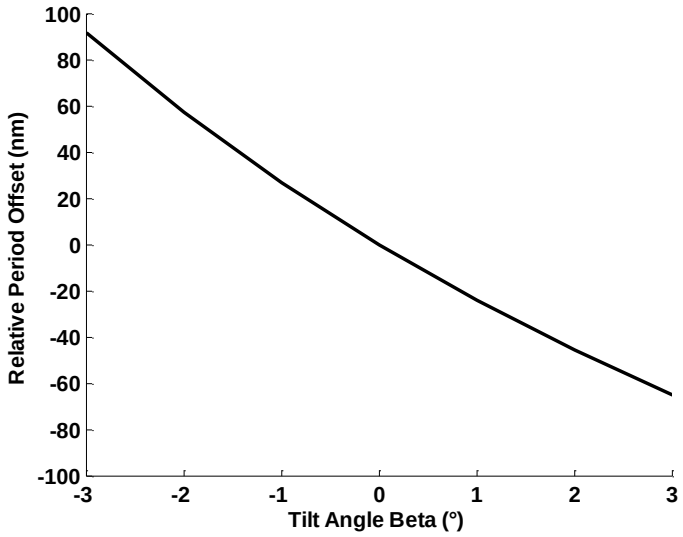

Fig. 3.14: mirror misalignment effect on a grating with 500nm of fringe period.

In order to evaluate the alignment of the overall setup, we have fabricated a set of different gratings varying the period of interference fringes. Fig. 3.15 shows the grating periodicity dependence from the beam incidence angle. As can be seen experimental data (dot) follow the expected behavior (solid line).

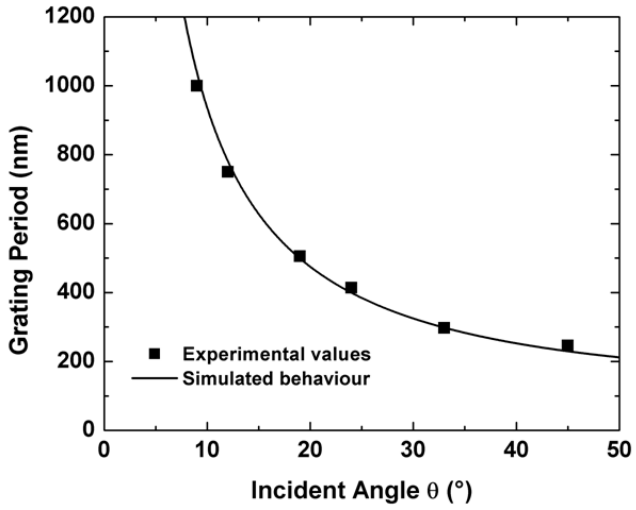

Fig. 3.15: correspondence between gratings period and laser beam incidence angle. Experimental values (dot) follow the theoretic behavior (solid line).

3.4.1.3 System noise reduction

Many sources of laser beam disturbances over the duration of a lithographic exposure could lead to a blurring or loss of resolution on the exposed image. Some examples are the intrinsic laser pointing instability, and environmental vibrations causing mechanical vibrations of optical components. All these effects induce vibration modes which can affect the fringes in two different ways: fringe drifting and pitch blurring. In the case of the Lloyd's mirror interferometer, small vibrations of the assembly does not cause fringe drift (phase shift), as the image source created by the mirror will automatically compensate the noise[42], [51]. However, a relative motion of the point-source and the interferometer (laser pointing tilt) induces pattern distortions. Since a change in incident angle between beam and interferometer is related to a change in the periodicity, the fluctuation of the fringe period during the exposure causes contrast and resolution losses. The pin hole vibration, that could induce a laser beam drift of several microns after 1m of beam propagation, is mainly caused by clean room air flux that impinge on the optical table. For this reason the whole LIL setup area has been enclosed in damping boxes that are set closed only when the system is running and kept open during the rest of the time.

3.4.1.4 Profile control

One convenient way to vary the effective image modulation (the sinusoidal profile amplitude A_{pv}) is to carry out a tandem exposure sequence[48], where each point of the sample is exposed in succession once with 2-beams interferometric exposure and once with a flood exposure using a single beam (without the mirror). The image contrast can be controlled by selecting the proper mixing of the two doses.

A surface profile modulation study has been conducted by tandem exposures over 2x2 cm^2 silicon samples, over which Bottom Anti-Reflection Coating (BARC) and S1805 resist layers had been spun. Samples were then exposed at constant pitch of 500 nm (i.

e. with a light incidence angle of 19°) and at a constant integrated dose of 80 mJ/cm^2 (resist sensitivity). The total integrated dose was systematically varied between a 2-beams imaging exposure and a single-beam flood exposure as shown in Table 5. Fig. 3.16 shows how the A_{pv} varies as a function of the 2-beams/total dose fraction.

Sample ID	D $_{2\text{-BEAMS}}$ [%]	D $_{FLOOD}$ [%]	D $_{2\text{-BEAMS}}$ [mJ/cm^2]	D $_{FLOOD}$ [mJ/cm^2]	A_{pv} [nm]
a	100	0	80	0	72
b	85	15	68	12	58
c	80	20	64	16	42
d	60	40	48	32	14
e	40	60	32	48	9
f	20	80	16	64	7

Table 5: tandem exposure LIL experiment data. 500 nm gratings are exposed by a constant integrated dose of 80 mJ/cm^2 (resist sensitivity). The total integrated dose was systematically varied between a 2-beams imaging exposure and a single-beam flood exposure.

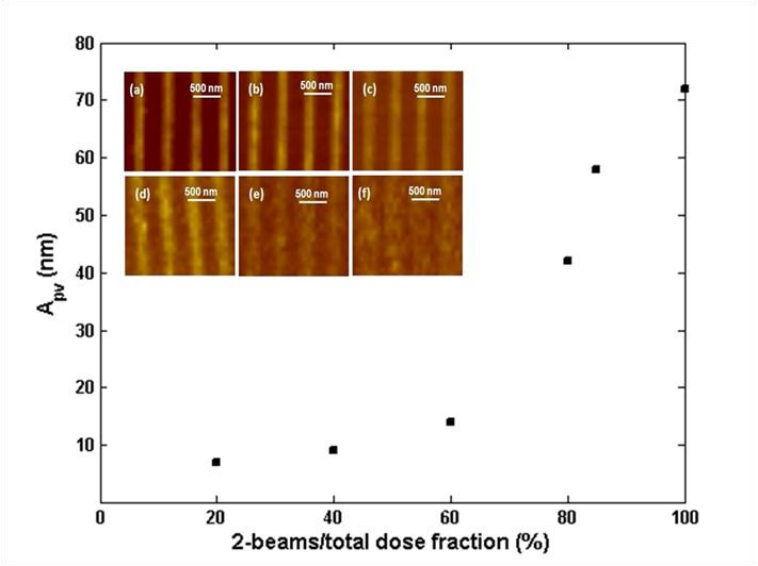

Fig. 3.16: A_{pv} values plotted as a function of the 2-beams/total dose fraction. Inset: AFM profiles of the samples a, b, c, d, e, f obtained with different partitioning of the integrated dose between a 2-beams imaging exposure and a single-beam flood exposure (see Table 5).

3.4.1.5 Process details and results

LIL exposures were conducted over samples of 2x2 cm^2 surface area. Silicon wafers were pre-baked for 20-30 minutes at 120°C and a 100nm thick film of Photoresist S1805 (Microposit®, Shipley European Limited, U.K.) and Propylene glycol monomethyl ether-1,2-acetate (PGMEA) solution (ratio 2:3) was spun at 3000 RPM for 30 seconds over a 100nm thick layer of Brewer Science XHRiC bottom anti reflection coating (BARC). Samples were then baked for 1min at 115°C. After the exposure, a developing solution of MICROPOSIT MF-319 and water in ratio 10:1 was used.

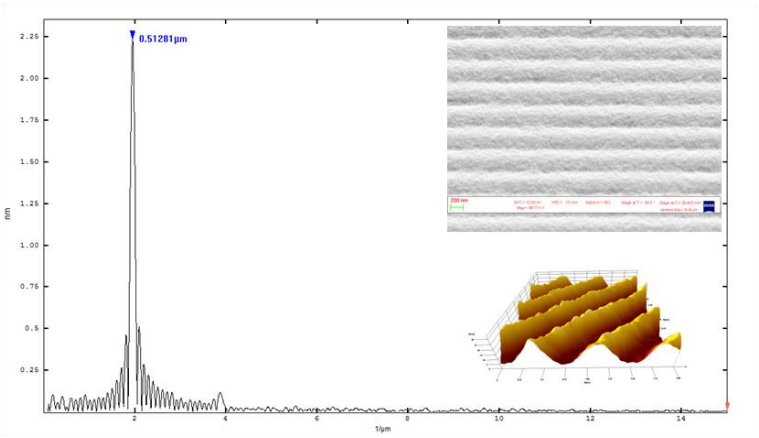

Fig. 3.17: Fourier spectrum of the grating profile. The Insets show a SEM image of the grating (tilt 45°) and the AFM-3D reconstruction of the sinusoidal modulation.

AFM and SEM measures are employed to characterize the surface profile. With a post-processing of AFM measurements, the Fourier spectrum of the grating profile was also calculated (Fig. 3.17). As can be seen, the spectrum is markedly peaked on a single spatial frequency with narrow bandwidth, indicating that the profile could be well approximated by a single sinusoidal component. The insets in Fig. 3.17 show the SEM surface topography (with a 45° tilt) and the 3D AFM reconstruction.

Resist grating pattern was replicated onto a thiolene resin film (Norland optical adhesive NOA61) supported on microscope glass slides using PDMS (polydimethylsiloxane) molds. The latter were obtained by replicating the resist grating masters using RTV615 silicone. Base and catalyst of the two-component silicone were mixed in 10:1 ratio and degassed under vacuum. The PDMS was then cast against the resist masters and cured at 60°C, well below the resist post-exposure bake temperature (115°C) to avoid distortion of the resist pattern and after 2 hours the PDMS was peel off from the resist master. In order to obtain rigid and stable stamps the PDMS molds were bonded to glass slides by exposing the flat backside of the PDMS mold and the glass slide to oxygen plasma before contacting them.

The PDMS mold was then used to UV imprint the initial pattern onto a drop of NOA61 resin dripped on top of a glass slide by just slightly pressing the mold onto the liquid resin and exposing to UV light (365 nm) from a Hg vapor flood lamp (Spectroline SB-100P) at a distance of about 10 cm for 20 min. After removing the PDMS mold, Cr (5 nm)\Ag (37 nm)\Au (7 nm) films were electron-beam evaporated onto the replicated NOA61 gratings.

The final gratings were functionalized with a thin film of thiolated polyethylene oxide (M_w 2000). The molecule used (mPEO) contained a non-reactive methoxy-group at one end and a thiol group (cysteine) for the gold-polymer bond at the other end. The functionalization procedure consisted of three simple steps. At first the substrates were cleaned in a basic peroxide solution (5:1:1 double distilled H_2O, 30% H_2O_2 and 25% NH_4OH) and then they were immersed in a mPEO derivative 1 mM aqueous solution for 24 hours. After incubation, substrates were extracted and rinsed with bi-distilled

water in order to remove physisorbed molecules from the surface and dried under vacuum (10^{-7} Atm) for 1 hour. This procedure gave a mPEO film about 5 nm thick. AFM and reflectivity measurements were made to assure that the functionalization procedure preserves the grating from damage.

3.4.2 Development of HOI Solgel based Photoresist for LIL

The following paragraph will outline the application of laser interference lithography (LIL) to create periodic features on a photosensitive hybrid organic inorganic (HOI) sol–gel material based on 3-glycidoxypropyltrimethoxysilane (GPTMS)[52]. This work is aimed at better understanding the potentialities of Hybrid Organic Inorganic sol-gel systems which are challenging materials since they are able to join some of the glass properties with their lithographic processability. They are becoming a key topic due to the low cost and ease of fabrication process, good optical and mechanical properties and the outstanding potentiality to be directly patterned by several technologies. The organically modified precursors used for the synthesis can contain polymerizable groups in their structure, such as double bonds and epoxy rings. This peculiarity has been already exploited for direct patterning of sol-gel films in a "one step" process by different lithographic techniques (such as UV, X-Ray and Electron Beam lithography) [53–55] and could have great benefits for cost effective mass production.

HOI materials can be used in combination with LIL for the realization of large area 1D and 2D periodic structures materials [48], [56], which find applications in many important photonic and optical devices such as light trapping systems for Photovoltaics[57], Distributed Feedback (DFB) lasers[58], photonic crystals[59], optical data storage[60] and plasmonic crystal for biosensing[61]. Therefore, the combination of LIL with suitable sol-gel photosensitive materials and with EBL for mix and match lithographic processes can introduce interesting advantages in several application fields. The presence of inorganic network significantly improves many important properties compared to the polymers, such as rigidity, environmental and chemical resistance and dimensional stability of the patterned features. Recently, HOI sol-gel systems have been employed[58], [62–65] in laser based lithographic techniques, anyway the more investigated HOI sol-gel materials are the acrylic ones, frequently mixed with titanium[62], [64] or zirconium oxides[58], [65].

3.4.2.1 Material details

The current system is very similar to a previous one which has been extensively investigated as a photo-structurable material by means of different lithographic techniques[55], [66]. However, the synthesis protocol has been here modified to further improve the film optical quality. The solution has been prepared starting from 3-glycidoxypropyltrimethoxysilane (GPTMS), one of the main sol-gel precursors used to synthesize epoxy based HOI materials. GPTMS possesses an organic chain ending with an epoxy ring: the presence of this functionality, linked to the inorganic network, enables this system to be a photosensitive material.

A metal alkoxide, germanium tetraethoxyde (TEOG), has been reacted together with GPTMS, and proper synthesis conditions have been selected to preserve the

photopolymerizable epoxy groups inside the final film structure, in spite of the presence of this Lewis acid. GPTMS has been hydrolysed with a 0,5% molar concentration of HCl (1N) for 1h at room temperature. TEOG has been added to the solution with a molar ratio GPTMS:TEOG= 80:20 and the sol has been left to react under reflux for 1h30. The final sol concentration has been set between 60÷150g/l (SiO_2+GeO_2). The solution has been filtered by a microporous membrane (0.2 μm Millipore).

3.4.2.2 Material deposition technique

HOI films, with desired thickness, have been deposited by spin coating technique on silicon wafers (100) and all the samples have been thermal treated on a hot plate at 80°C for 15 min in order to remove the residual solvent (pre-baking). As can be seen in Fig. 3.18, a wide interval of thicknesses can be obtained, ranging from some microns to few hundred of nm. This gives the possibility to fit the requirements of a great number of applications.

To promote the cationic polymerization of epoxy groups under UV/laser exposure, a commercial photo-initiator has been added to the solution with a molar concentration of 1% with respect to GPTMS. 4-(Phenylthiophenyl)diphenylsulfoniumtriflate (DPST, Aldrich) belongs to the photoacid generator (PAG) class and has the main absorption peak around 300 nm. The UV-Visible absorption spectrum of this compound, dissolved in methanol, is depicted in Fig. 3.19 and its chemical structure is shown in the inset.

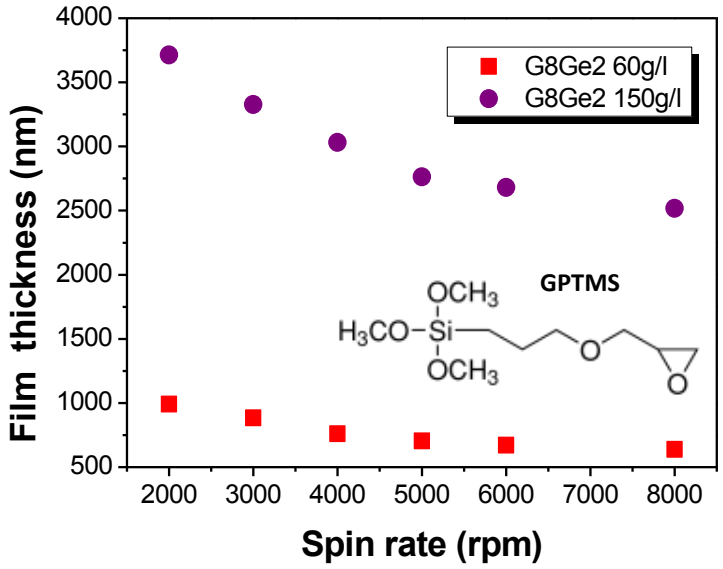

Fig. 3.18: Film thickness in function of spin rate. The inset shows the chemical structure of GPTMS, the main precursor of the HOI sol-gel system.

3.4.2.3 LIL exposures

Different sinusoidal gratings have been realized by means of Lloyd's mirror LIL exposures. A post-exposure bake at 60°C has been applied to all samples for 60'' and grating structures have been obtained dissolving the unexposed regions by means of a diluted NaOH solution (NaOH: H_2O= 1:100) for 5-15'', and then rinsing in water before drying with nitrogen.

3.4.2.4 Material characterization

To realize good quality periodic structures by LIL technique, the main issue is the correct transfer of intensity pattern into the photosensitive material. The response to UV light of a similar GPTMS based sol-gel system has been previously investigated using a common XeHg lamp, with emission of lines in a broad spectral range (280-400nm)[54], [66]. Nonetheless, it is of the primary importance to explore which are the effects of exposure with the IL UV laser line on the hybrid film.

In order to fit the laser wavelength, the right cationic photo-initiator has to be selected. DPST presents an absorption peak centered at 300 nm. Fig. 3.19 shows that the laser line falls in a region where the initiator still absorbs enough.

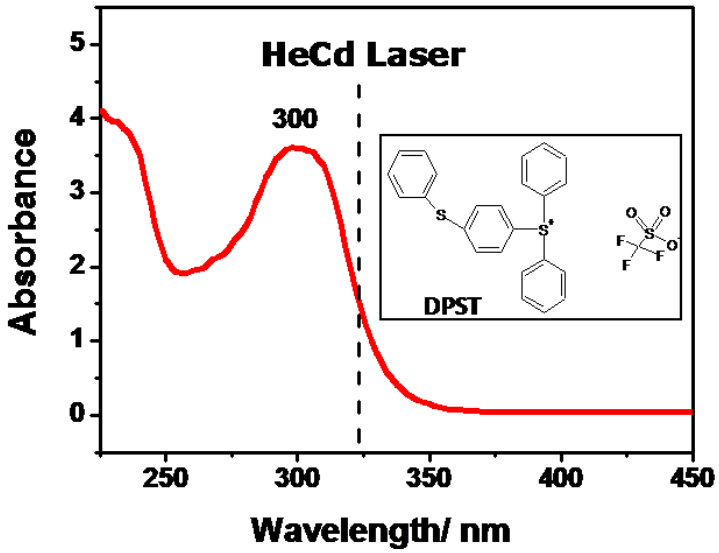

Fig. 3.19: UV-Vis absorption spectrum of DPST in methanol. The dash line indicates the emission of the HeCd laser used for LIL exposures. In the inset, the chemical structure of DPST is reported.

The evolution of the HOI structure as a function of the UV exposure dose has been evaluated on planar films by FTIR spectroscopy (Fig. 3.20). Infrared absorption spectra have been recorded in the range of 400−4500 cm^{-1} by a Fourier Transform Infrared spectrometer (Jasco FT-IR-620), with a resolution of ±4 cm^{-1}. Laser exposures have been carried out with an intensity of about 550μW/cm^2 on the sample surface, and the doses reported in Fig. 3.20 correspond to irradiation time of 10, 15 and 60 min, respectively.

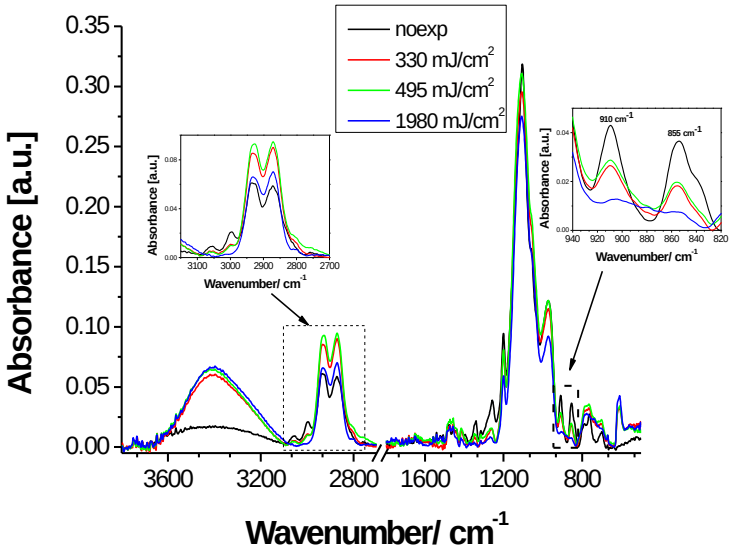

Fig. 3.20: FTIR absorption spectrum of hybrid sol-gel film exposed to increasing dose. In the insets, the characteristic absorption bands of the epoxy group are reported.

The FT-IR spectra show how the laser irradiation of the samples reduces the signals around 3060-3000 cm^{-1} and 910 cm^{-1}, characteristic of the epoxy rings[55]. The decreasing of these absorption peaks indicates that the ring opening reaction has been initiated, and the photo-polymerization process seems to occur in a similar fashion to the exposure with an high pressure XeHg lamp. The organic cross-linking induced by the UV laser exposure leads to an hardening of the structure and decreases the solubility of the exposed areas in organic or basic solvents (negative tone behavior). Even if the epoxy signals completely disappear only at the highest dose, the formation of the three-dimensional network reaches a sufficient degree of polymerization just after 10 min of irradiation, becoming insoluble in diluted NaOH. Notice that an important difference can be noted respect to the use of other light sources such as X-rays and UV[53], [54]: the exposure with the HeCd laser does not produce any degradation of the film structure also after 1h, as evidenced by the absence of the peak at 1725 cm^{-1}[54], [55]. This indicates a better efficiency of laser polymerization of epoxy rings, without unwanted secondary effects. In fact, the appearance of the absorption band around 1725 cm^{-1} can be explained by the formation of C=O bonds, probably due to the breaking of the etheric group in the propylic chain of GPTMS.

3.4.2.5 Gratings morphologic characterizations

The optimization of exposure dose plays an essential role in the quality of the final structures, but the morphology of the sinusoidal gratings has been influenced by several other experimental conditions. The development step is a key point in the pattern generation and many parameters, such as the pre- and post- exposure thermal treatments (time, temperature) and the solvent/time used to remove unexposed areas has to be carefully selected to obtain good relief profiles.

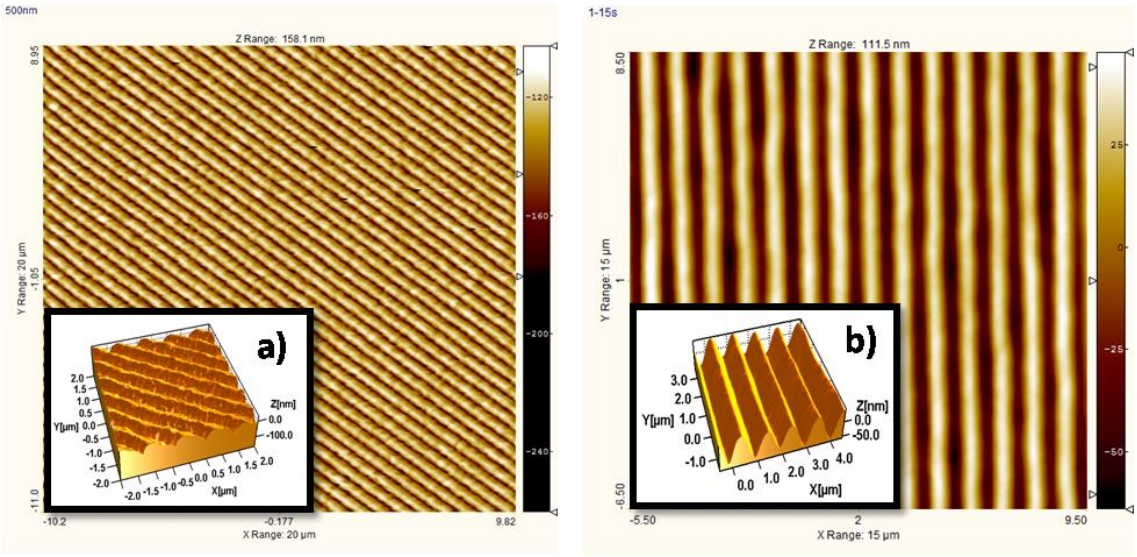

Fig. 3.21: AFM images of diffraction gratings with periods of 500 nm, field size 20x20µm^2 (a) and 15x15µm^2 (b). In the inset the 3D images of zoomed scans of the patterns are shown.

Exposure time has been set around 10 min (laser intensity of 550µW/cm^2) and it has been optimized according to the grating periodicity. The dose has been adjusted to minimize the proximity effect for small pitch grating, applying shorter exposure time. The dark fringes are not completely dark and a higher irradiation time has been verified to decrease the depth of the sinusoidal profile. The height of the structures reaches a maximum at 10s, after that time the developer probably starts to etch also the exposed areas and a profile roughness appears.

Fig. 3.21 shows the AFM images of the gratings with two different periods, 500 nm and 1 µm. The patterns look homogenous and the sinusoidal relief is uniform. Anyway, the small pitch grating has a lower modulation depth (around 40 nm) than 1µm structures (100 nm) and an evident Line Edge Roughness (LER). The same remarks can be made observing the SEM images, reported in Fig. 3.22. The line irregularity of the small pitch grating (650 nm period) appears clearly respect to the 1 µm modulation pattern.

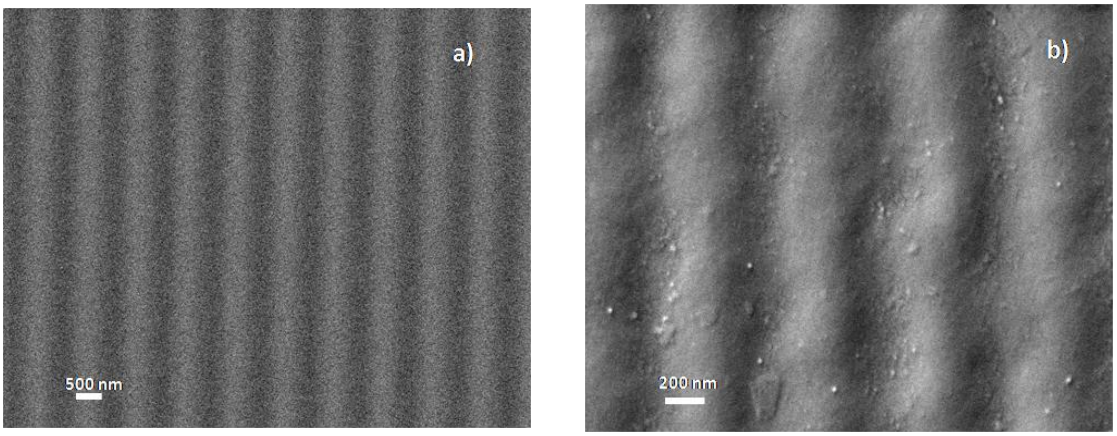

Fig. 3.22: SEM images of modulation patterns with periods of 1 µm (a) and 650 nm (b) fabricated by LIL.

Summarizing, the generation of profiles with controlled sinusoidal features on hybrid sol gel materials can be exploited in the realization of plasmonic crystals for sensing applications[61], by depositing a metallic coating directly on the hybrid gratings. The advantage of using HOI sol-gel materials in the realization of plasmonic crystals is the control of both optical and geometrical parameters (period and amplitude) in order to match the optimal coupling condition for surface plasmon polariton (SPP) propagation. This technique allows to realize plasmonic crystals in a wider range of materials, HOI or polymeric other than photosensitive ones, whose optical and functional properties are tunable according to the specific device needs.

4 Absorption profile modulation by means of 1D digital plasmonic gratings

4.1 Introduction

The peculiar optical properties of metallic nanostructures are more and more employed in the optoelectronic field. The science of Plasmonics is now giving the attractive chance to tailor the natural characteristics of bulk materials by controlling, enhancing and adapting the local EM fields, e.g. by exciting SPP resonances[5] or by using metal Nano Particles (NP)[35]. In particular, if a dielectric next to plasmonic nanostructures is used as optical absorber such structures could allow a strong enhancement of optical absorption [67], thus representing an extraordinary perspective for, efficiency improvement of semiconductor devices such as solar cells or photodetectors.

As stated in par. 2.3, a great effort have been devoted to study a way to exploit the high scattering cross section of metal nanoparticles and their light trapping properties in Si solar cells [68–71]. In some recent works, researchers have considered also the use of periodic plasmonic nanostructures. They have demonstrated their effectiveness in applications to thin film solar cells [72], [73].

In this context, we want to describe our latest results in analyzing the different mechanisms of transmission of the light through an 1D subwavelength metal grating placed at a vacuum/silicon interface[74]. The aim of the work is to show that by using periodic metallic nanostructures it is possible to modulate the absorption profile in an underlying bulk Silicon substrate. Furthermore, a proper optimization of such structures allows us to try an experimental integration in more complicated devices as silicon bulk solar cells.

The numerical and analytical optical simulations that we have performed are based on the Finite Elements Method and modal analysis. We focus on the optical response of a digital Gold grating on a semi-infinite Silicon substrate to a normally impinging 1000nm-monochromatic wave, varying systematically both thickness (h) and period (d) of the grating. Different geometric configurations can change dramatically the absorption profile, concentrating the EM fields in close proximity of the metallic nanostructures or simply reducing the absorption extinction depth. By analyzing the set of possible working optical regimes, SPPs and cavity-mode resonances appear to be effectively exploitable to enhance NIR-light absorption in different shallower regions of the underlying Silicon.

4.2 Finite Elements model setup

The study presented hereafter has been applied to a simplified model based on vacuum/Gold/Silicon interfaces where Gold was chosen because of its low dissipation in the NIR compared to other metals and because of its well defined plasmonic properties. For symmetry reasons we limit the simulation of the gold periodic structure to one period, setting periodic boundary conditions (see Fig. 4.1). The ratio between slit width and period is kept constant to 0.1. The in-plane asymmetry of the structure

between *x* and *y* axis, determines different optical responses for different polarizations of the incident light. In this work we consider only TM polarized incident light, with magnetic field parallel to the metal stripes, since it is the only polarization that can give rise to SPPs in an 1D metallic grating. The dielectric constants of Gold and Silicon at 1000nm were taken to be[75]

$$\varepsilon_{gold} = -46.4 + 3.5i$$
$$\varepsilon_{silicon} = 12.9 + 3.6 \cdot 10^{-3} i$$

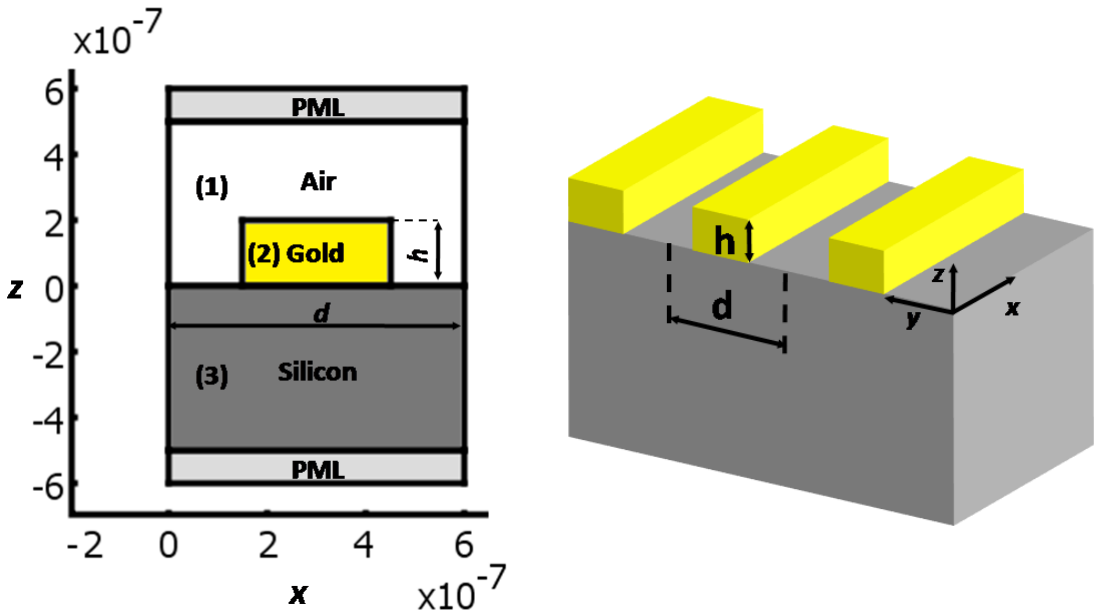

Fig. 4.1: sketch of the model. 1D subwavelength metallic grating placed at a vacuum/silicon interface irradiated by a normally impinging 1000nm-monochromatic wave. For symmetry reasons we limit the Gold periodic structure to one period(periodic boundary conditions). The simulation focuses on the study of the optical response varying systematically both thickness (*h*) and period (*d*) of the grating.

Far fields analysis have been made by the following procedure. We performed a 1D Fourier Transform of the FEM-computed fields along *x* direction at a given depth. In the k_x-space we filtered out the non *z*-propagating modes. Far fields were then obtained transforming back in the real space, taking into account absorption in Silicon. For each geometric configuration (h,d) and within different depths in Silicon, we have calculated the values of transmittance and absorptance. The latter is defined as

$$absorptance_{Si} = \int \frac{1}{2}\,\omega\varepsilon_3^{''}\,|\boldsymbol{E}|^2 dV \qquad 4.1$$

that is a volume integral over the Silicon layer, being ω the angular frequency and $\boldsymbol{E}$ the electric field [76]. We also computed the effective absorption profile of light as a function of depth in Silicon *Q(z)* averaging the local absorption over one period length of the plasmonic array.

4.3 Modal analysis of the 1D digital grating

In order to have an insight into the physics of our system, an analytic approach is necessary beside the purely numerical one given by FEM. A recent rigorous modal analysis of the system has been performed by Sturman et al. [77]. It considers separately the fields in the regions above and below the grating and within the slits (we indicate them with numbers 1, 3, and 2 respectively, see Fig. 4.1). Fields in regions 1 and 3 are expanded in Bloch-Floquet modes while in region 2 they are expanded in the complete set of eigenmodes (propagating, evanescent and anomalous) of the 1D plasmonic crystal given by the alternating metal and dielectric layers. The full field reconstruction is then obtained through field matching at 1-2 and 2-3 interfaces, according to Maxwell's equations. We followed a simplification of this approach[78], [79], which nevertheless catches the main physics and has the advantage of leading to simple analytical expressions for the relevant physical quantities (such as transmittance). It is found neglecting, in region 2, all the evanescent modes and keeping only the propagating ones, neglecting losses. If the slit width is smaller than the vacuum wavelength of the incident radiation, only the fundamental propagating eigenmode is allowed. At the horizontal interfaces Surface Impedance Boundary Conditions are imposed [80]. According to this simplified model, the transmittance of the structure results to be

$$T = \frac{1}{\sqrt{\varepsilon_3}} \frac{\left|\tau_{1,2}\right|^2 \sum_{-\infty}^{+\infty} \cos\theta_i \left|\tau_{2,3,i}^2\right|^2}{\left|1 - \left|\rho_{1,2}\right|\left|\rho_{2,3}\right| e^{i\phi_{tot}}\right|^2} \qquad 4.2$$

where τ and ρ are the single-interface (1-2 and 2-3) magnetic field amplitude transmission and reflection coefficients, θ_i is the i-th diffraction order angle, and ϕ_{tot} is the total phase accumulated by the single propagating waveguide mode travelling back and forth in the slit:

$$\phi_{tot} = \arg(\rho_{1,2}) + \arg(\rho_{2,3}) + 2k_0 N_{eff}\, h \qquad 4.3$$

being k_0 the vacuum wavevector. It has been shown [81] that actually the model fails if $|\varepsilon_m|$ is low and/or the slit width is very small with respect to the wavelength of the incident light, since these situations correspond to high penetration of the fields in the metal and the plasmonic contributions to the fields are relevant. In our case of $|\varepsilon_m|$~46, however the problems arise when the slit width is lower than 10% of the wavelength of incident light. The main deviation from the simple model is found in the propagation constant of the fundamental waveguide propagating mode inside the slits whose effective wavevector results to be higher than the vacuum wavevector. The effect can be taken into account assuming the presence of an effective medium inside the slits with proper refractive index N_{eff}. Following the results found by Sturman et al. [77], we took an effective refractive index

$$N_{eff} = \frac{C}{a} + 1 \qquad 4.4$$

being *a* the slit width, with an optimal constant *C* of about 30nm.

4.4 Optical resonances

The numerical and analytical simulations that comes from equation 4.2 allow to identify the main features of the optical response of the 1D plasmonic grating: the optical resonances rising by the interaction of solar radiation with periodic metallic nanostructures. We can further correlate the characteristics of such resonances with material and geometric parameters of the gratings. Three main optical features play a relevant role: Surface Plasmon Polariton (SPP) resonances, Cavity Mode (CM) resonances and Wood Rayleigh anomalies (WR). Their basic characteristics in relation to the absorption profile modulation in silicon are outlined below and synthesized in Table 6.

4.4.1 Cavity Mode (CM) resonances

These resonances result from the multiple scattering of the single propagating mode inside the slits. The mode is partially reflected and transmitted at the slit ends. When the phase difference ϕ_{tot} between the waves transmitted in the substrate is a multiple of 2π, a peak in transmittance is observed, like in a Fabry-Perot resonator. The interesting fact is that, when this resonance takes place, a great fraction of the incident light is channeled within the slits and is transmitted in the substrate (Fig. 4.2.a). This phenomenon is commonly referred as Extraordinary Optical Transmission (EOT) [77–80], [82–86].

4.4.2 Surface Plasmon Polariton (SPP) resonances

SPPs (see chapter 1) are surface EM waves which propagate at a metal-dielectric interface and are evanescent in the normal direction (Fig. 4.2.b). They are excited in a 1D grating when the in-plane component of the incident p-polarized radiation and that one of the scattered waves sum up to match the SPP momentum, i.e.

$$k_0 \sin\alpha + \mathrm{nG} = k_0 \mathrm{Re}\left(\sqrt{\frac{\varepsilon\varepsilon_m}{\varepsilon+\varepsilon_m}}\right) \text{ and } \mathrm{n} = 1,2 \ldots \qquad 4.5$$

with α incidence angle, $\mathrm{G} = \frac{2\pi}{\mathrm{d}}$ and ε the dielectric constant of the insulator facing the metal surface (vacuum for 1-2 interface, Silicon for 2-3 interface). This kind of resonance is associated to a transmittance extinction and to a high field enhancement in proximity of the grating (hundreds of nm in Silicon) [83].

4.4.3 Wood-Rayleigh anomalies (WR)

Abrupt changes in transmittance as a function of period are observed in configurations for which a diffraction order lies in the plane of the grating (Fig. 4.2.c), i.e. at periods $d_n = n\lambda/N$, being N the refractive index of the dielectric medium[87]. These configurations mark a discontinuity since for $d > d_n$ the *n*-th diffraction order does exist

while for $d < d_n$ it does not. It is generally accepted that the peak in transmission is due to the abrupt redistribution of energy among the allowed orders passing through the $d = d_n$ configurations[88]. WR anomalies are not resonant phenomena but rather are due to pure geometrical reasons and are fully independent of CM and SPPs.

SPP	They are surface EM waves propagating at the horizontal metal dielectric interfaces. Their characteristic is a high EM field concentration within few hundreds of nm from the metal surface.
CM	They are Fabry-Perot like resonances arising within the grating slits. When they are present light is channelled into the main waveguide mode of the slit and transmitted into the substrate.
WR	They appear at particular frequencies at which a diffracted order propagates at grazing incidence with respect to the plane of the grating.

Table 6: optical resonances that could be excited in the geometry sketched in Fig. 4.1.

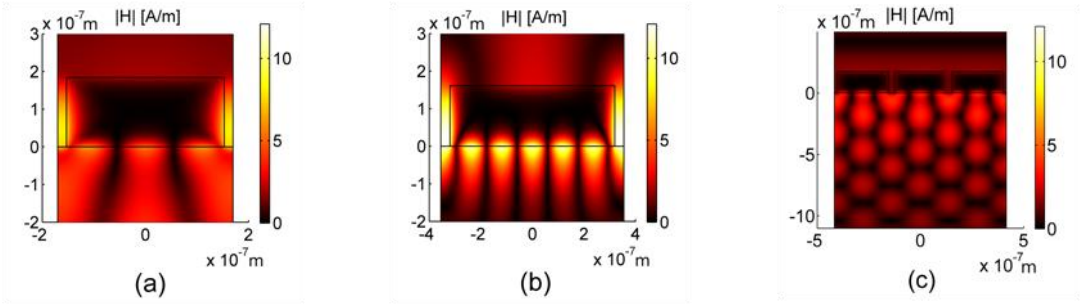

Fig. 4.2: Magnetic field norm enhancements. (a) h = 184nm, d = 340nm: CM resonance; (b) h = 161nm, d = 710nm: coupled SPP-CM pair resonance; (c) h = 175nm, d = 278nm: coupled WR-CM pair resonance.

It is worth noting that CMs are *local* resonances, since they would appear as well in a single illuminated slit without any periodicity[89]. On the other hand SPPs are *global* resonances since they can exist thanks to the coherent periodicity of the structure[4], [5]. As many authors pointed out, however, CMs and SPPs are not independent each other[90]. Actually one should better speak of a hybrid mode which presents both CM and SPP resonant characteristics. The SPP character dominates the transmission properties of the grating as the pitch gets proximate to one of those satisfying eq. 4.3. On the other hand the EOT efficiency is greatly enhanced in presence of a periodic structure [87].

4.5 Simulation Results

In Fig. 4.3 we report the resulting maps of transmittance and of absorption within 300nm in Silicon obtained with FEM. The values are normalized to the case of absorbing Silicon substrate coated with a perfect anti-reflection coating providing unitary transmittance. Resonant (h,d) configurations predicted by the semi-analytical model are reported as well (see caption of Fig. 4.3 for details). The periods chosen for the simulation are smaller than the wavelength of incident light. In the Silicon substrate, however, $\lambda_0/N_{Si} \sim 278\text{nm}$, so that diffractive effects are present.

4.5.1 CM excitation

Looking at the transmittance map (Fig. 4.3.a) we see that CM resonances (black lines) are clearly associated with an enhanced transmission in the (h,d) configurations far from the SPP resonant ones (grey lines) in which the dominant SPP character determines a transmission extinction. In order to facilitate the resonances identification, in this computation we have chosen a slit-to-period ratio of only 10%. Notwithstanding the small opening fraction, the maximum transmittance value obtained for $h = 184nm$, $d = 340nm$ is as high as 0.68, reaching the value of bare Silicon. Considerably larger transmittances can be obtained optimizing the duty cycle (for $h = 184nm$ and $d = 340nm$, a maximum transmittance of 0.94 is obtained with a duty cycle of 31%).

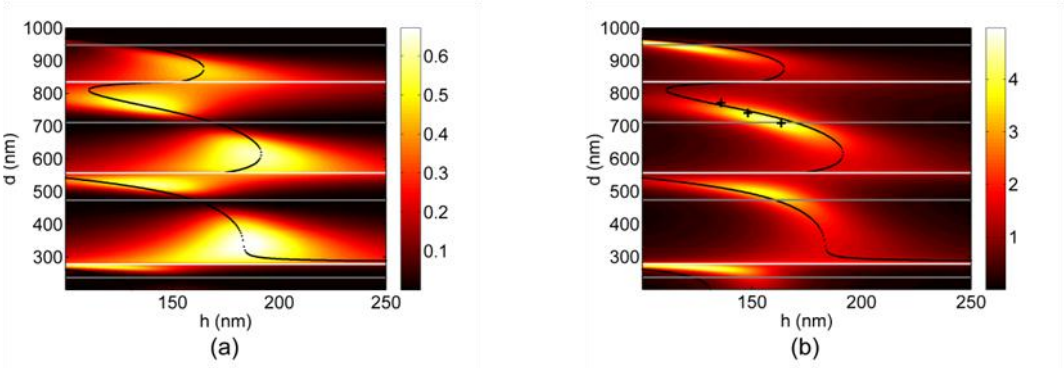

Fig. 4.3: FEM-calculated transmittance (a) and absorption enhancement (b) maps within 300nm in Silicon with respect to perfect AR-coated Silicon. Over-plotted black and grey lines mark respectively CM and SPP resonances according to the analytical model. White lines mark configurations which present a WR anomaly. Black crosses mark configurations whose absorption profile is reported in Fig. 4.4.

4.5.2 Coupled CM-SPP excitation

CMs are also correlated to absorption enhancements. Within 300nm in Silicon (Fig. 4.3.b), the largest enhancements (up to 350%) are obtained when both the conditions for SPP and cavity mode excitation are satisfied at the same time (at the crossing between gray and black lines). In these configurations CM resonances canalize the whole incident power into an SPP mode rather than into a *z*-propagating mode, giving rise to an extraordinary SPP (Fig. 4.2.b). By comparison, in Fig. 4.2.a, notice the typical much weaker field enhancement in a configuration where only CM is excited without SPP resonant coupling. Looking at the absorption profiles (Fig. 4.4) we observe that, in strongly SPP-CM-resonant configurations (black line), most of the enhancement is confined in the metal proximity and decays exponentially within the typical plasmonic decay length of eq.1.31 within about 100nm. The enhancement factor can be up to 30 times in the first 30nm of Silicon. However, far from the grating (Fig. 4.4, inset) the absorption is almost zero in SPP resonances since SPPs typically produce transmission extinctions. On the other hand, strong CM but not SPP resonant configurations (light grey lines) show absorption profiles that are much less confined close to the surface, but are higher in depth due to EOT.

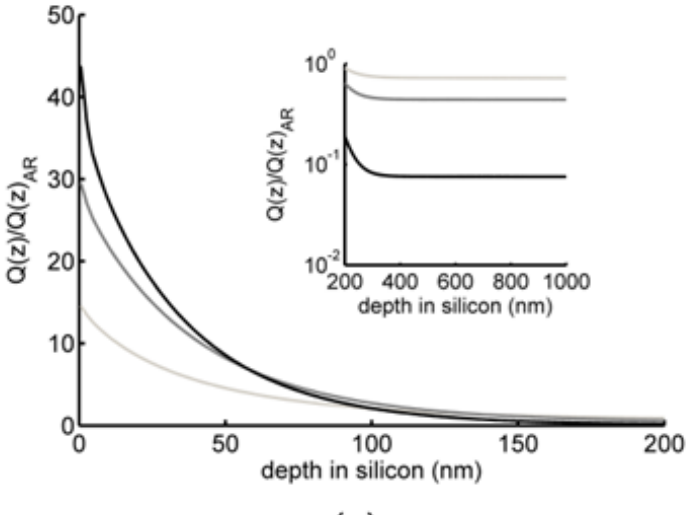

Fig. 4.4: absorption profile enhancement with respect to perfect AR-coated Silicon in configurations marked with crosses in Fig. 4.3: h = 136nm,d = 765nm (light gray); h = 148nm,d= 735 (medium gray); h = 163nm, d = 705nm (black); inset: absorption profiles within 1μm depth.

4.5.3 Coupled CM-WR excitation

Looking at the absorption within a thicker (40μm) Silicon layer (Fig. 4.5.a) we find that the best enhancements are obtained in CM-resonant configurations proximate to WR anomalies, i.e. those shown in Fig. 4.2.c. In these configurations, CM resonance results to efficiently couple to diffracted waves propagating at grazing angles with respect to the grating plane. The mechanism is particularly efficient when only the $n = \pm 1$ diffraction orders are present besides the 0-th one, around configuration identified with a black cross in Fig. 4.5.a ($h = 175nm$, $d = 290nm$). Looking at the absorption profiles (Fig. 4.6), these are clearly the superposition of two exponential decays, relative to the $n = \pm 1$ and $n = 0$ diffraction orders respectively. As can be seen, in high enhancement configurations, the $n = \pm 1$ orders contribute significantly to the whole absorption profile (see dotted lines in Fig. 4.6) which remains higher than that of a perfect AR-coated Silicon up to about 40μm depth.

The strong absorption enhancement in proximity of the grating in presence of SPP resonances is also correlated to an high power dissipation in metal. The maximum absorptance of metal reaches values up to 84% (h = 163nm, d = 765nm) in correspondence of SPP-CM resonant configurations, down to about 14% (h = 175nm, d = 285nm) near CM-WR configurations.

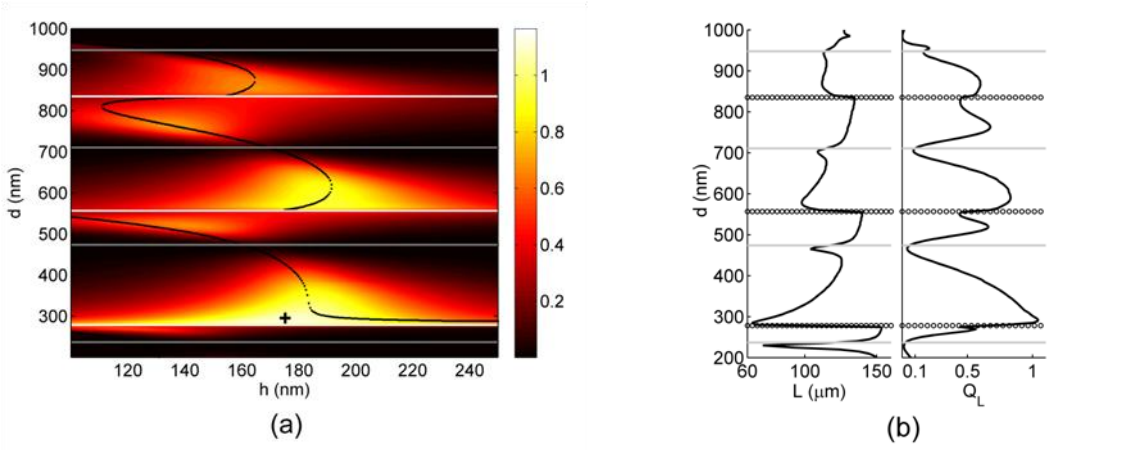

Fig. 4.5: (a) Absorption enhancement within 40μm in Silicon with respect to Silicon treated with perfect AR coating. Over-plotted lines are defined as in Fig. 4.3. (b) Left: Extinction length *(L)* of the absorption profiles calculated in CM-resonant configurations ($h_{CM}(d)$,*d*); right: absorption within *L* with grating normalized to absorption within the same *L* in case of perfect AR-coated Silicon. Grey horizontal lines and circles mark respectively SPP resonant periods and WR anomalies.

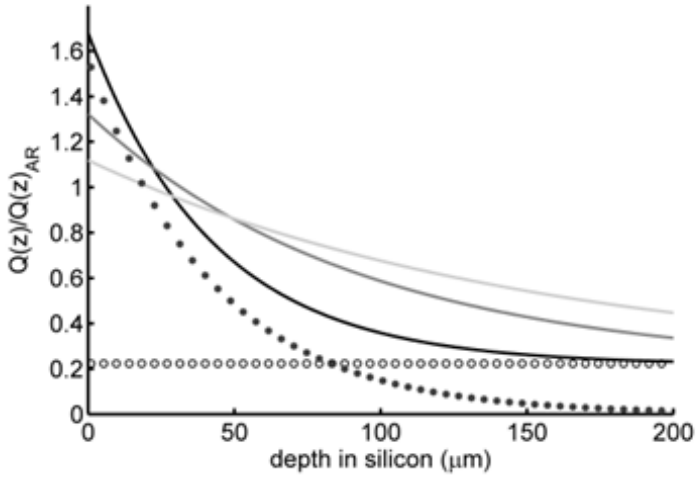

Fig. 4.6: absorption profile enhancement in configurations near the cross in Fig. 4.5: *h* =175nm and *d* respectively 285nm (black), 300nm (medium gray), 320nm (light gray). Black dots and circles represent the contributions to the whole black absorption profile coming from the $n = \pm 1$ and n = 0 diffraction orders respectively.

4.5.4 The absorption profile extinction length (*L*) evaluation

In order to highlight the remodulation of absorption profile achievable with CM-WR coupling, we consider now the locus of CM-resonant configurations, i.e., for every period *d*, we consider the thickness $h_{CM}(d)$ which maximizes the FEM-calculated transmittance. In these configurations we consider an absorption profile extinction length (*L*) taking the depth in Silicon at which a fraction of $(1\text{-}e^{-1})$ ~63.2% of the transmitted power is absorbed. This is the fraction of power absorbed within the typical decay length in presence of an exponential-like absorption profile. We finally calculate the absorption enhancement within *L* ($\equiv Q_L$) integrating *Q(z)* down to depth *L* and

normalizing point by point to the absorption within L with respect to the case of a perfect AR-coated film on Silicon. In Fig. 4.5.b we report L and Q_L as a function of period, being $h = h_{CM}(d)$. It is clearly seen that at CM-resonant configurations just above WR anomalies the extinction length drops while the absorption within L is strongly increased. Although most of the Q_L are lower than 1, it is to be noted that we have an extraordinary absorption for every period at which Q_L exceeds 0.1, i.e. the fraction of period not covered by metal.
As a general comment it clearly appears that the absorption length is always much shorter than the corresponding for pure absorption in Silicon (156μm at 1000nm wavelength) and almost always accompanied by an enhancement of absorption with respect to the normalized open area.

4.5.5 Incidence of the gratings duty cycle

The absorption enhancement can be greatly improved optimizing the duty cycle. In Fig. 4.7 we show the trends of L and Q_L as a function of the duty cycle for the fixed (h,d) configuration h = 145nm, d = 280nm, which is very close to the WR-anomaly (see Fig. 4.5.a). The maximum of absorption is found 1.5 times greater than in AR-coated silicon within L = 80μm for a duty cycle of about 20%. As can be seen, in this configuration most of the power transmitted by the CM in the slit is drained by the n = ± 1 diffracted waves. We note that the extinction length drops at a duty cycle of about 0.7, before reaching the value it has in absence of grating, while Q_L has a local maximum. This is due to a stronger coupling of the CM resonances to the n = ± 1 diffraction orders than to the n = 0.

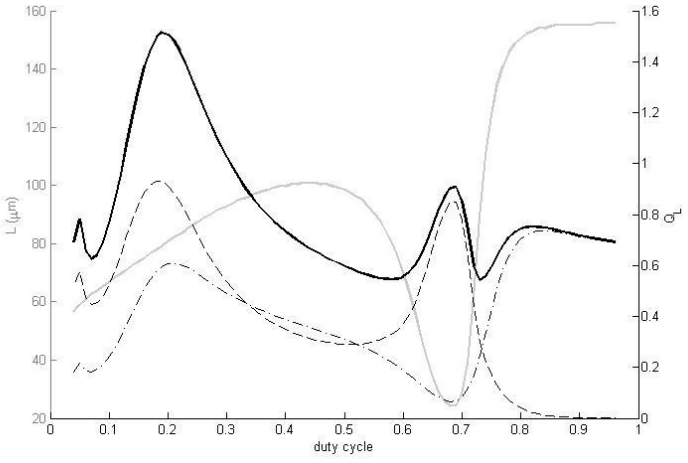

Fig. 4.7: Gray: Extinction length of the absorption profile for different duty cycle values; black: absorption within L normalized to absorption within the same L in case of perfect AR-coated Silicon. Dash-dotted and dashed lines are the contribution to QL from the n = 0 and n = ± 1 diffraction orders respectively. h and d are set to 145nm and 280nm respectively. The set of parameters h = 145, d = 280, duty cycle = 0.2 was found to optimize the absorption enhancement within 40μm (+ 210%).

At this point we can now summarize the simulation work outlined above in this chapter where a study of the optical response of 1D digital plasmonic gratings placed on a semi-infinite absorbing substrate was under investigation. The entire work was based on the

need to clarify the role and the potentialities that the optical resonances of such structures have in remodulating light absorption. Thus, confirming hypothesis, numerical and analytical simulations show that relevant absorption enhancements can be produced in Silicon at different depths, in relation to the type of plasmonic resonance involved. SPPs resonances lead to high field enhancement (up to + 350%) in close proximity to the grating, whereas cavity modes coupled to grazing diffracted waves allow an efficient transmission and spreading of light power into the substrate, leading to an enhanced absorption of long-wavelength radiation in shallower regions of the underlying Silicon (up to + 51.3% within 80μm). The results may be useful to design high efficiency Silicon-based photodetectors devices active in the IR spectral range. Further studies will be addressed to the wavelength response of the gratings in order to obtain absorption enhancement over wide bandwidth with possible applications in solar cells.

5 Digital 1D plasmonic gratings on bulk solar cells

5.1 Introduction to the ORION project

This chapter is focused on the study performed on the integration of 1D digital plasmonic gratings on bulk Silicon solar cells which is part of a more multifaceted European Project aimed at the optimization of materials and technologies involved in concentration Photovoltaic production. The main objectives of the project are to reduce the systems' cost/watt and increase the overall cell efficiency.

The aim of reduction of system cost/watt is achieved by:

- developing an all-plastic system by using recycled plastic compounds;
- developing Si bulk solar cells for automatic assembling technology;
- implementing and industrializing automated high-throughput technologies for cell assembly and optics production.

The increase of system efficiency is pursued by:

- increasing Si cell efficiency by using plasmonic crystal structures;
- developing plastic materials doped with down-converting nanoparticles for modification of the solar spectrum in order to enhance the absorption efficiency of solar cells.

Plasmonic structures are planned to be realized by combination of interference lithography and evaporation technique with the aim to use low-cost techniques that could be used for industrial silicon solar cell production.

Thus the aim of my work is focalized on the investigation of solar cell efficiency enhancement using metallic gratings to remodulate and improve the light absorption of semiconductor layers. In this context, our work has been arranged in a simulation phase which is followed by the nanofabrication process design and development. Finally, the electro-optical characterization of the samples realized is presented.

5.2 Optical simulation

Finite Elements optical simulation of plasmonic crystals were performed in order to investigate their capability of molding and remodulating the optical absorption profile of light in a silicon solar cell in order to increase the optical path length of light in the NIR part of the solar spectrum. Such modeling work is very closely correlated to the propaedeutic one described in Chapter 4 in which a simple layout was simulated (Fig. 5.1). Although, the aim of the first study was to clarify the main optical resonances involved and how they affect the absorption profile of light in the underlying silicon substrate, this second part of simulations is dedicated to optimize both geometrical parameters of the grating (period, thickness, slit width) as well as the dielectric environment in order to maximize the broad range absorption of the AM1.5 solar spectrum within the full thickness of the solar cell.

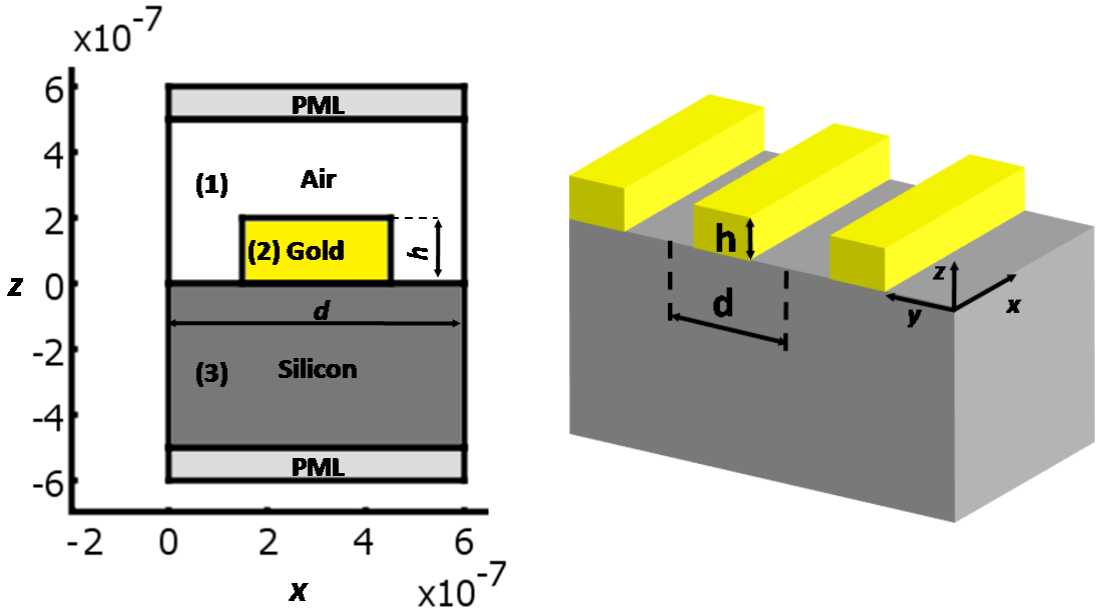

Fig. 5.1: sketch of the first simple model. 1D subwavelength metal grating placed on a vacuum/silicon interface irradiated by a normally impinging 1000nm-monochromatic wave.

Different layouts were considered with respect to the initial one (Fig. 5.2). However, the setup providing best results was found to be a Silver plasmonic grating placed on top of a Si_3N_4 AR coated silicon substrate (Fig. 5.2(right)).

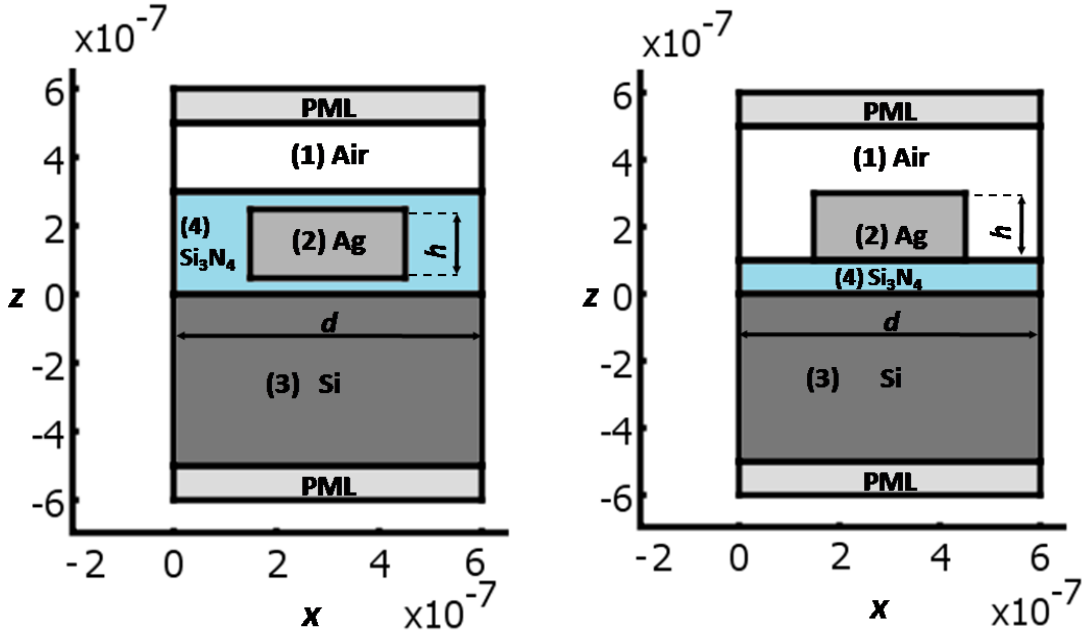

Fig. 5.2: different layout tested.

The optimization of the structure was performed calculating the full spectral response of the structure as a function of the following parameters:

- Grating thickness range: 10÷160nm.
- Grating period range: 200÷800nm.

- Grating duty cycle range: 0.7÷0.9.
- Si_3N_4 coating thickness range: 5÷95nm.
- AM1.5 solar spectrum. Range: 400÷1100nm. Normal illumination.

We considered the absorption within 200 microns in Silicon taking into account a specular reflection at the back contact (i.e. a 400 microns total optical path length in Silicon). The optimal configuration found is the following:

Optimal configuration found

Silver thickness: 100nm

Period: 480nm

Duty cycle: 0.8

Si_3N_4 thickness: 70nm

Broad range Absorption enhancement within 400um in Silicon with respect to bare 70nm-Si_3N_4-coated Silicon (TM polarization): ***+3.6%***

Notice that the enhancement found is relative to the TM polarization of the spectrum. No configuration was found to enhance the TE part of the spectrum with respect to the bare structure.

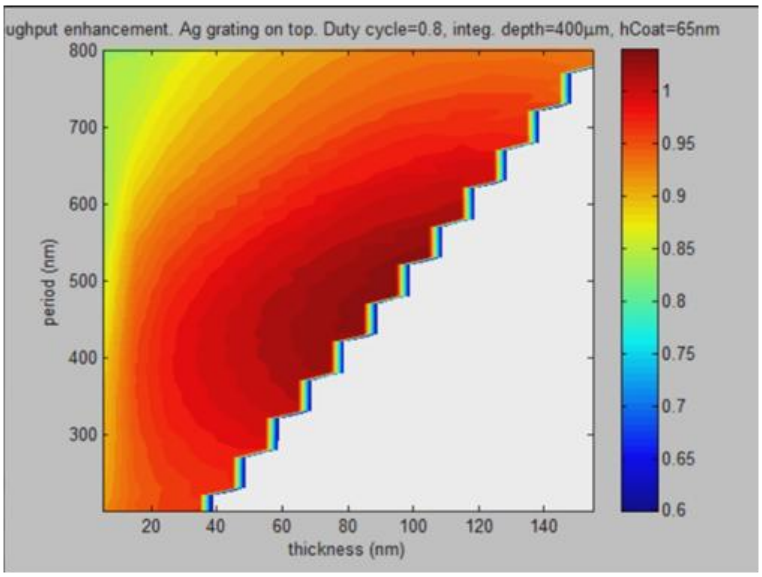

Fig. 5.3: absorptance throughput enhancement map as a function of grating thickness and period. Configurations not realizable were discarded. The Si_3N_4 layer thickness is close to the optimal value of 70nm.

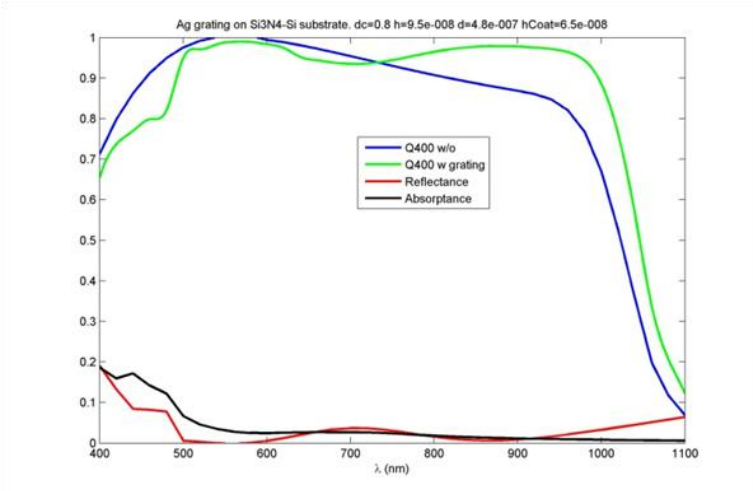

Fig. 5.4: optimal configuration. Green: absorptance within 400 µm in Silicon compared to absence of grating (blue), red: reflectance spectrum, black: metal absorptance spectrum.

Fig. 5.3 shows the Silicon absorptance throughput enhancement map as a function of grating thickness and period. In Fig. 5.4 the spectra relative to the optimal configuration are reported. As can be seen, in such a grating setup a broad absorptance enhancement is found in the NIR spectral range. In the VIS some losses are seen, especially at low wavelengths mainly due to dissipation in metal. However metal dissipation is lower than in case of grating *embedded* in SiO_2 or Si_3N_4. In fact, plasmons are known to dissipate a greater fraction of their energy in metal when the medium adjacent to the metal has high refractive index.

5.3 Nanofabrication of plasmonic crystal on bulk solar cells

5.3.1 Batches of solar cells for plasmonic crystals integration

In order to set up the nanofabrication process of plasmonic crystals on solar cells and to test the effect that the integration of such metallic gratings has on the devices, a special batch of cells has been produced by one of our partner of the project (the MET company). These cells have a square active area of 11x11mm^2 defined by edge isolation and a total area of about 20x20mm^2. They are realized on p-doped (resistivity 1-20 Ohm·cm) CZ Si wafers having a thickness of 525µm.

Compared to standard solar cells, the devices of this batch have two main differences. The surfaces are not textured so that it is possible to compare the simulation results with experimental findings. The other difference consists in a reduced thickness of the metal front grid made up of a 200nm-thick Nickel layer. Both of these two features are aimed at reducing the surface topography making the nanofabrication process on proof devices simpler.

Nevertheless the feasibility of integrating the plasmonic crystal on substrates with high surface topography such as solar grade wafers and even textured MET solar cell with thick front metallization grid has been tested and demonstrated successfully. For this task, 190µm-thick cells have been used; they are textured and have the standard Ni-Cu bilayer front metallization with thickness of several tens of µm.

5.3.2 General description of the flow chart

A fabrication process able to pattern plasmonic crystals over the large surface areas of solar cells has been developed. As described in the section about optical simulations, the optimized grating layout has a pitch of about 500nm and Ag nanostrips with thickness and width of about 100nm. Clearly it is not simple to realize such narrow metal strip-width and the requirement to pattern areas of several cm^2 make this task even more challenging. Furthermore, in order to find application in photovoltaics, the fabrication techniques employed must be up-scalable and must have an high throughput. Therefore, the nanopatterning technique that was used to meet these requirements is Laser Interference Lithography (LIL). This lithography technique is best suited for our application since it is able to pattern periodic features with high uniformity and accuracy over large areas. Moreover, it allows to get really high resolution nanostructures with a single exposure step. This is a great advantage compared with other sophisticated exposure tools with similar resolution which employ the step and repeat procedure to cover similar areas.

The nanofabrication process that was designed for our purposes is schematized in Fig. 5.5. As stated above the aim is to get a Silver nanograting on top of Si_3N_4 coated cell.

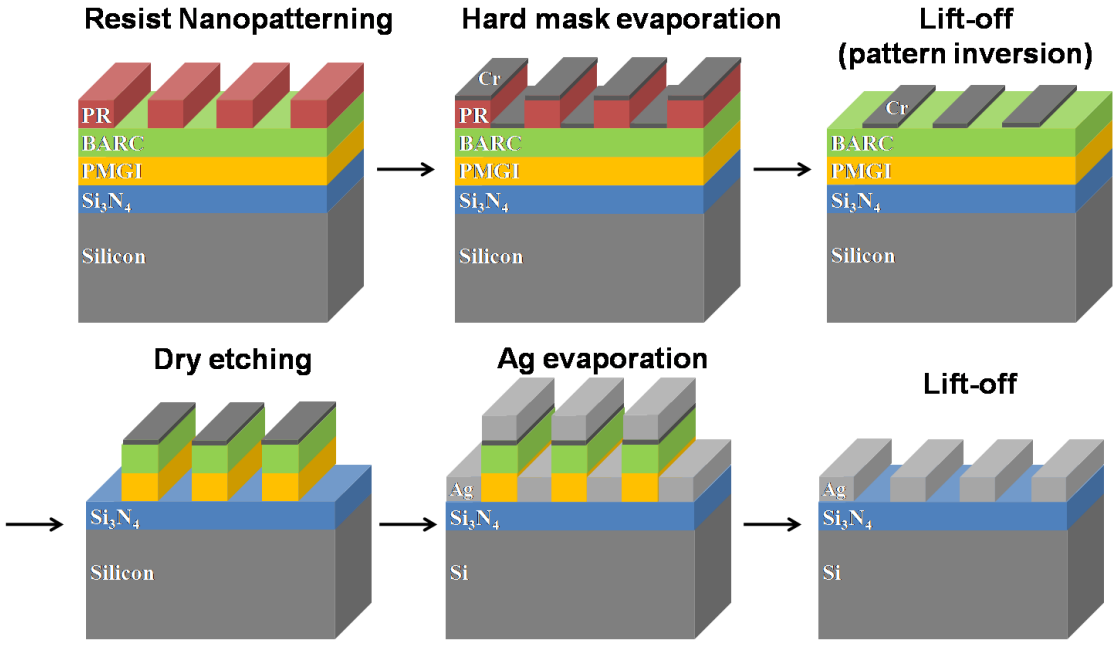

Fig. 5.5: Schematic flow chart designed to fabricate plasmonic Silver gratings on solar cells

We coated the cells with a tri-layer of resists. The topmost is a positive photoresist (PR) which can be exposed with high resolution through a UV laser beam. The central resist layer is a Bottom Anti-Reflection Coating (BARC) employed in optical lithography to avoid vertical standing waves pattern in the top photoresist due to light reflected from the bottom of the sample. Such layer allows to obtain high resolution lithographies, widening the process latitude and reducing the sensibility to substrate topography and variation of resists thickness. The resist layer on the bottom is a lift-off resist (PMGI)

and it is used to realize an undercut for the deposition of Silver nanowires by evaporation and to finally remove the resist pattern.
We experimented that through LIL exposure it is easier to obtain narrow resist wires instead of narrow slits in resist. Considering that we have to realize silver wires with narrow linewidth (duty cycle, or slit-to-period ratio, ~80% suggested by simulations), the narrow top photoresist lines must become the Ag pattern on the surface of the cell. This requires an inversion of the tone of the lithography that we obtain by a first lift off of a thin metal hard mask. After this lift-off step we have a periodic array of metal wires with narrow slits in-between over the two remaining resist layers. Such resists are not photosensitive and are not etched neither by the solution used as developer for the top photoresist nor by the ultrasonic bath used for the first lift off step. So the top metal grating is used as hard mask to transfer the pattern into both the underlying resists through dry etching. Finally Silver is evaporated over this structure. A second lift-off step is performed in a ultrasonic bath of a solution etching the PMGI and releasing the other layers placed in the slits between Silver stripes.

5.3.3 Resist tri-layer

Through the rest of this section we describe in detail every fabrication step. The cells received by MET are cleaned through immersion in IPA and dried blowing nitrogen. Then the resist layers are spin coated over the cells.
The PMGI resist we used is Microchem SF3. The requirement on this resist is that its thickness must be greater than the thickness of the Silver grating (100nm) in order to make the final lift-off possible. On the other hand it have to be not too thick in order to have resist structures with reasonable aspect ratio and to make the fabrication process more stable. SF3, spin coated at 1000RPM for 1', has a thickness of about 130nm after baking in a hot plate for 5' at 200°C.

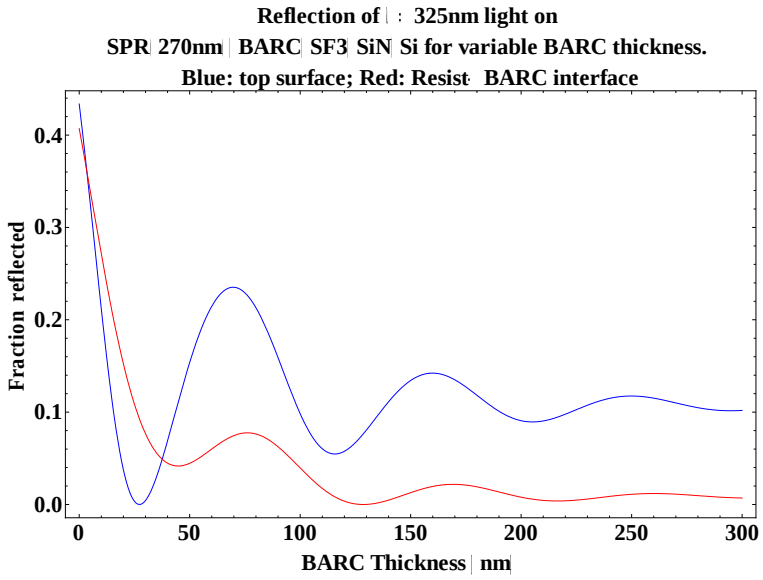

Fig. 5.6: Reflectance of light at 325nm wavelength on the resist trilayer over the Si_3N_4 coated solar cell at photoresist-BARC interface (red) and at the top resist interface (blue)

The Bottom Anti-Reflection Coating is Brewer Science XHRiC-11. We simulated (Fig. 5.6), with a code implementing the transfer matrix method, the reflectance of the resist stack at the photoresist-BARC interface in order to find the BARC thickness which minimizes the reflection of light from the substrate and improves the lithography quality. We found that for a BARC thickness of 230nm the reflection is lower than 1%. Such film can be obtained spinning XHRiC-11 at 1000RPM for 1' and baking in hot plate at 175° for 1'.
Finally the top photoresist is spun over the BARC. We started to use a negative top-photoresist (All Resist AR-N 7520) but it required too long exposure time with our setup. So, to get the designed narrow linewidth, we replaced it with a positive photoresist, Rohm and Haas SPR 1.2 thinned with PGMEA (1:1), that has a thickness of 270nm spinning at 3000RPM for 45'' and baking in hotplate for 1' at 115°C.

5.3.4 LIL exposures

For a fixed value of grating pitch, the line/period photoresist fraction depends only on the exposure dose[91]. By a large over-exposition, the grating linewidth could be decreased or increased, respect to an equal line-slit width, respectively using positive or negative photoresist[92]. In order to obtain a 480nm pitch and 80% duty cycle, we have tested both positive and negative photoresist following the over-exposition method comparing pros and cons of the two strategies. Fig. 5.7 shows our preliminary over-exposure tests on negative (left) and positive photoresist (right).

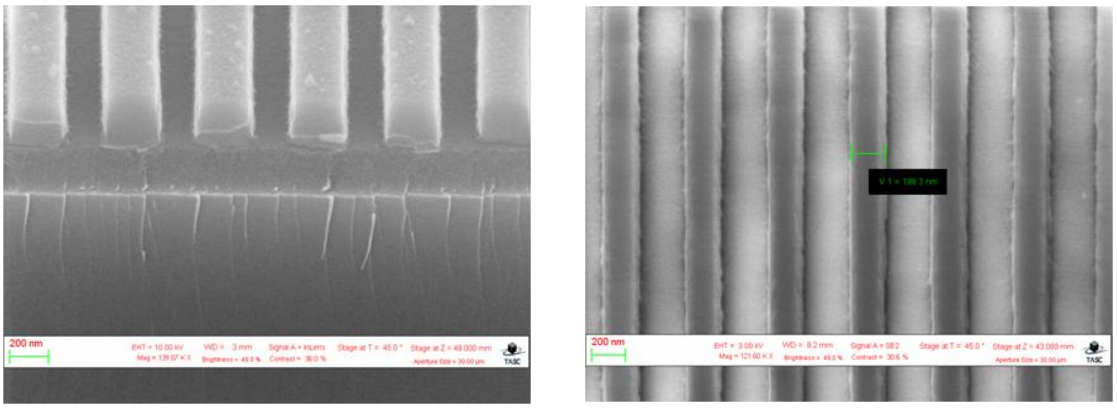

Fig. 5.7: preliminary over-exposure tests on negative (All Resist AR-N 7520, left) and positive photoresist (Rohm and Haas thinned SPR 1.2, right)

Although the use of a negative photoresist would simplify the process avoiding the step of pattern inversion, it required too long exposure time with our setup (up to 2 hours to get narrow slit width). For this reason we focused on positive photoresist and performed the exposure parameters optimization reaching the optimum simulated goal. Fig. 5.8 shows the final results: 100nm-wide lines patterned on flat 1x1 cm^2 solar cells substrates.

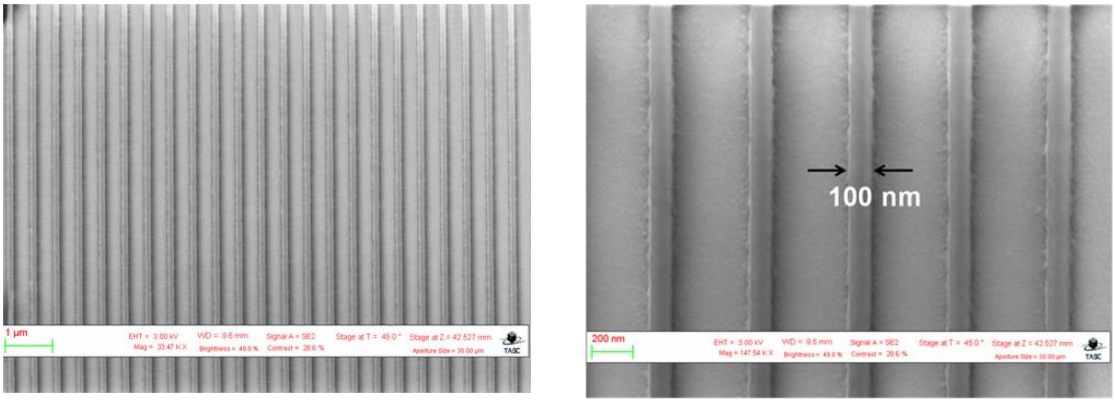

Fig. 5.8: Low magnification (left) and high magnification (right) SEM image of a positive photoresist grating with 100nm linewidth patterned over BARC/PMGI/solar cell

5.3.5 Hard Mask evaporation and lift off

In order to invert the tone of the high resolution resist pattern we deposited a thin metal layer followed by lift off. We evaporated in vacuum 10-15 nm of a hard mask material. In particular we used Chromium, but other metals (such as Nickel) or dielectric hard masks could be used instead. We employed an evaporation setup based on an e-beam accelerated toward a crucible and heating the target material in a chamber at a pressure of about $2 \cdot 10^{-6}$ torr. The evaporation rate is monitored with a quartz balance and set to 0.5-1 Å/s and a feedback loop controls the e-beam power.

The lift off is performed in a ultrasonic bath of acetone for 1'. Acetone dissolves SPR photoresist pattern while it does not etch the BARC and PMGI. The following SEM image (Fig. 5.9) show a Cr hard mask pattern over BARC after this lift off step.

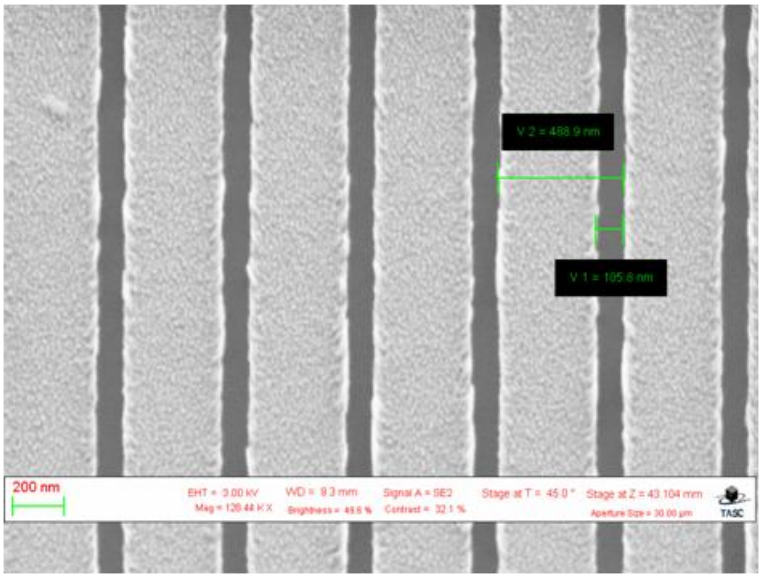

Fig. 5.9: SEM image of a sample after the first lift off step: Cr grating with thickness of 10nm and slit width of about 100nm

5.3.6 Active area definition

In order to avoid that the Silver grating provides a short circuit path between the front metal grid and the base of the cell crossing the trench constituting the edge isolation, an optical lithography step is performed to define the active area patterned with the grating. The lithography mask is a square with 10mm side aligned within the 11mm square defined by edge isolation. We spun over the samples a lift off resist, Microchem LOR 7B (2000RPM 1', bake 180°C 5', 700nm-thick), and an optical photoresist, Shipley S1818 (5000RPM 1', bake 115°C 1', 1.9µm-thick). The apparatus used for UV patterning is a KARL SUSS MJB3 mask aligner (Fig. 5.10). UV light at 365nm is produced by a Hg vapor lamp. The exposure time is 25'' and the resist is developed for 45'' in MF-319 developer. This developer removes the exposed areas of the photoresist and the underlying areas of LOR creating also an undercut under the S1818 pattern. After lithography the trench is covered by resist. The undercut is needed to create a discontinuity (physical and electrical) between the inner active area and the outer area of the Ag layer that will be evaporated to realize the plasmonic crystal.

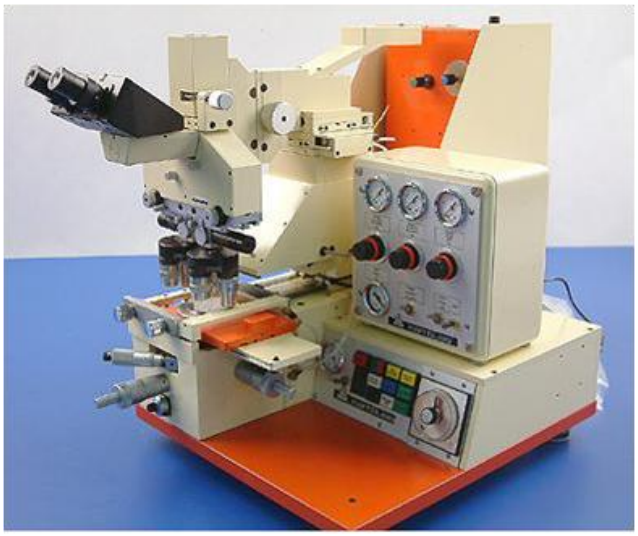

Fig. 5.10: KARL SUSS MJB3 mask aligner

5.3.7 Dry etching

The metal hard mask pattern in the central active area of the cell is transferred into the underlying BARC/PMGI layers through dry etching. The thick S1818 resist layer masks the outer area of the device.

We used a Reactive Ion Etching (RIE) equipment with parallel plate electrodes. We developed two different etching steps with different plasma chemistry to etch BARC and PMGI. In the first step the reactive gas is CF_4 flowing in the chamber at 20 SCCM and creating a pressure of $1.8 \cdot 10^{-1}$mbar. With a RF power applied of 80W, the bias voltage which accelerates the ion in the plasma is 250V. We tuned this RIE process to get good anisotropy and to etch the ~200nm thick BARC layer in 6'.

PMGI is commonly wet etched with optical photoresist developers. We started to use this standard procedure to etch PMGI after dry etching of BARC. Due to the high

resolution of the pattern, this process turned out to be very critical. So we decided to develop another RIE step based on an O_2 plasma to etch PMGI. The O_2 flow in the chamber is 30SCCM, the pressure is regulated at $2.5 \cdot 10^{-1}$mbar and the plasma is applied for 7' at 250V bias voltage. This plasma recipe is characterized by an isotropic behavior and etches also the BARC horizontally. This behavior is desirable because it creates a wide undercut under the metal hard mask which eases the following Silver lift off. The undercut is clearly visible in the SEM images at tilted angles in isolated defects of the grating (Fig. 5.11).

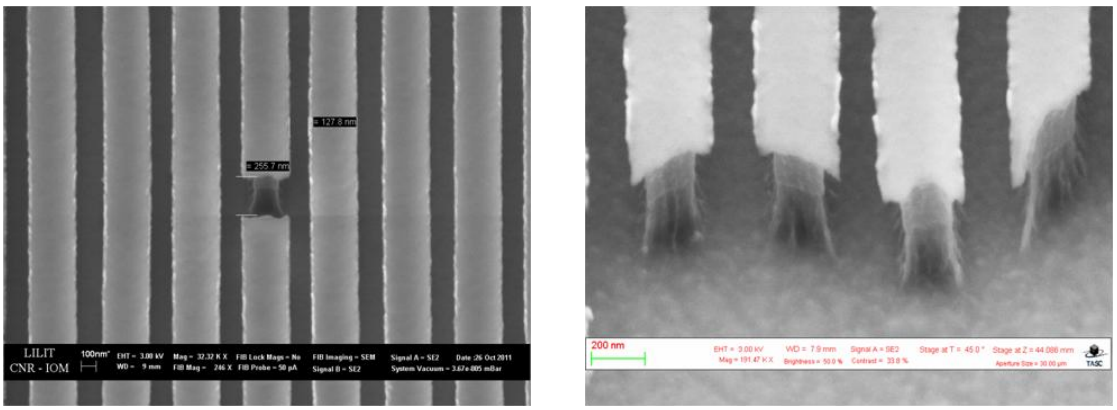

Fig. 5.11: SEM cross section of the nanopattern in isolated defects after the RIE processes

5.3.8 Silver evaporation and lift off

Finally Silver is evaporated through e-gun evaporation in vacuum over a thin metal adhesion layer (3nm of Ti or Cr). The deposition rate is set to 1Å/s and the pressure in chamber is about $2 \cdot 10^{-6}$ torr. The lift off is performed in an ultrasonic bath of a photoresist developer (MF-319) which dissolves SF3. Fig. 5.12 is the image of a sample after Ag evaporation and before the final lift-off step. In Fig. 5.13 there are several images of the final result, a Silver grating with thickness of 100nm over a Si_3N_4-coated Si solar cell. As can be seen the gratings are uniform over large areas and are well defined even over the metallization grid.

The minimum Ag linewidth (maximum duty cycle of the grating) what was realized experimentally on the cells was about 135nm (corresponding to a DC of 72%), next to the optimal value (100nm) suggested by simulations. Nevertheless we are confident that even narrower Ag stripes can be fabricated with a further fine tuning of each step of the process.

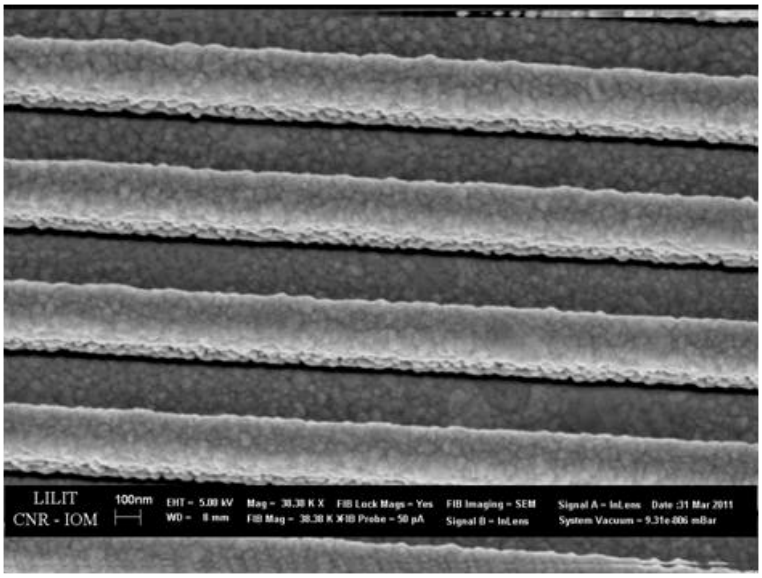

Fig. 5.12: SEM image of a sample after Ag evaporation and before liftoff. It is evident the discontinuity between the Ag layer on the top of the resist pattern and on the substrate.

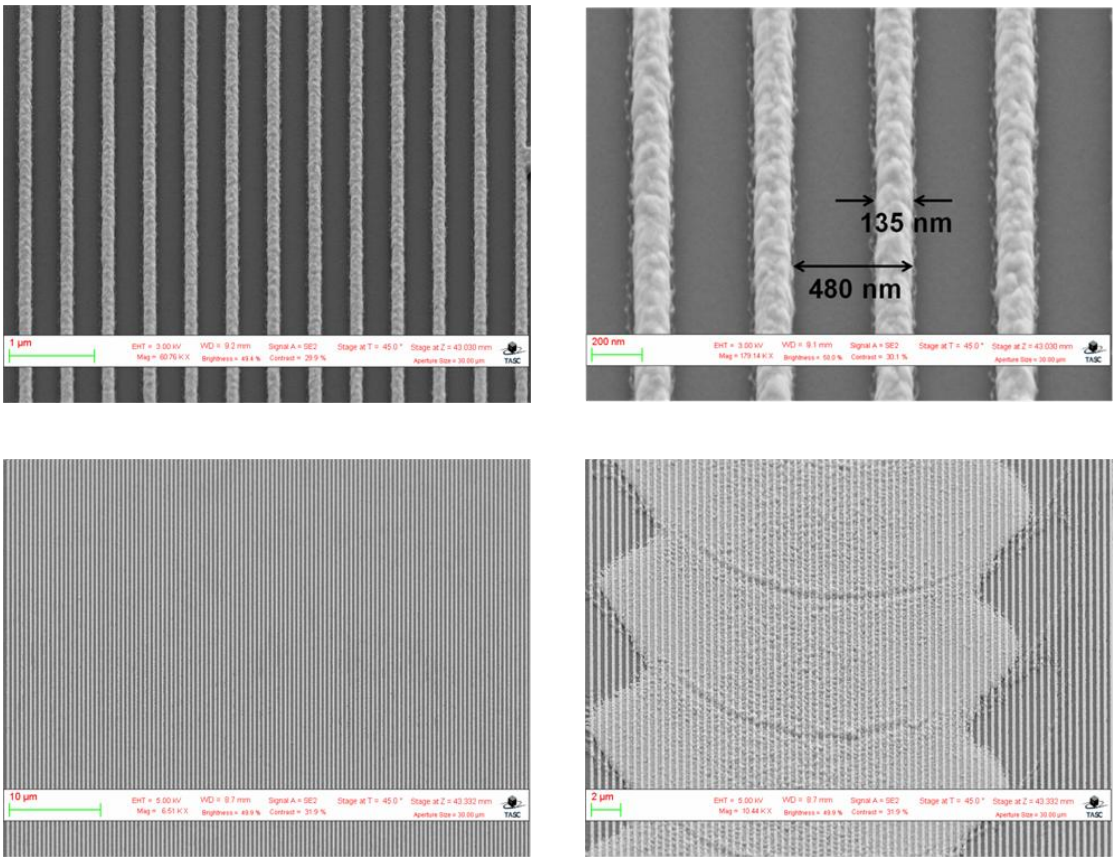

Fig. 5.13: SEM images of plasmonic gratings (480nm period and 135nm strip-width) realized on MET solar cells. The image on the bottom right shows the grating on a metal finger.

Finished cells integrating the crystal have the trench and the outer area of the cell covered by more than 2µm of resist and 100nm of flat Silver on top (Fig. 5.14), which is electrically disconnected from cell electrodes and totally reflecting for radiation incident outside the active area. Thus the active area of these devices is well defined and a value of 100mm^2 can be used to get the current density from the measured current.
The frame patterned with photolithography and delimiting the active area can also be removed with a prolonged treatment (~20') in a ultrasonic bath of a photoresist developer leaving only a nanopatterned square in the active area and the bare Si_3N_4 coated surface outside (like bare reference cells). The drawback is that this process removes the back Aluminum metallization. Thus, an Al film was evaporated to replace the back electrode but different electrical characteristics are expected compared to the original one, making a comparison of cell properties before and after grating integration less reliable for such devices.

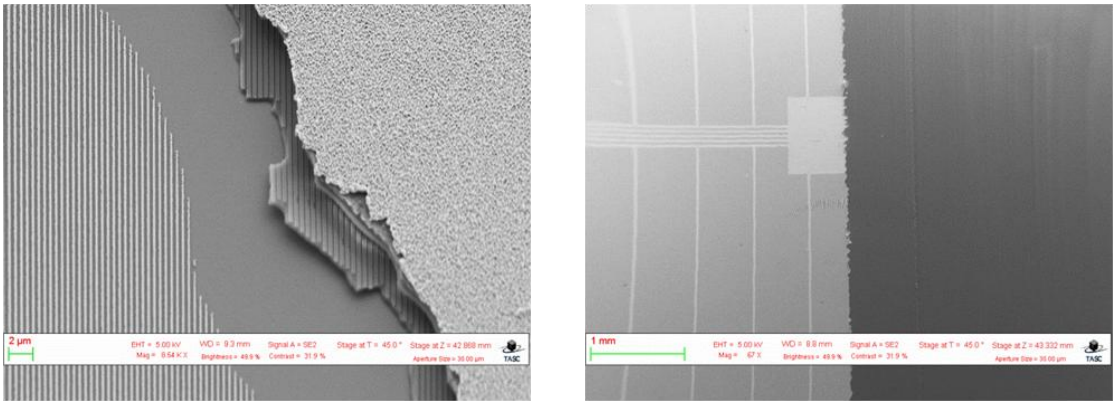

Fig. 5.14: SEM images of the border of the cell active area at high (left) and low (right) magnification.

5.3.9 Gratings on textured solar cells

As already discussed above, we have also tested and demonstrated the feasibility of the overall nanopatterning process using substrates with high surface topography such as solar grade wafers (Fig. 5.15) and even textured solar cell with thick front metallization grid (Fig. 5.16).
Notice that such results could not be obtained with standard nanoimprinting lithography. The noise on the laser intensity distribution pattern caused by the topography is minimized by the planarizing effect of the two bottom resist layers. In particular, it was employed the BARC property to optically decouple the photoresist from the substrate. Nevertheless the roughness and stability in resist linewidth look somewhat worse than the nanopatterns obtained on flat substrates. Fig. 5.17 shows the Silver grating fabricated over textured solar cells. The dry etching steps should be further optimized in order to avoid passivation layer etching.

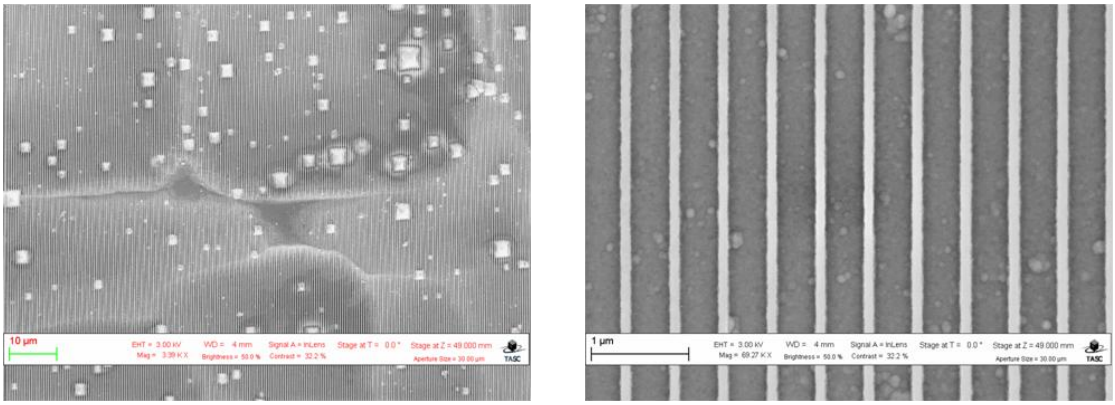

Fig. 5.15: SEM micrographs at low (left) and high (right) magnification of resist periodic nanopatterns on a solar grade wafer

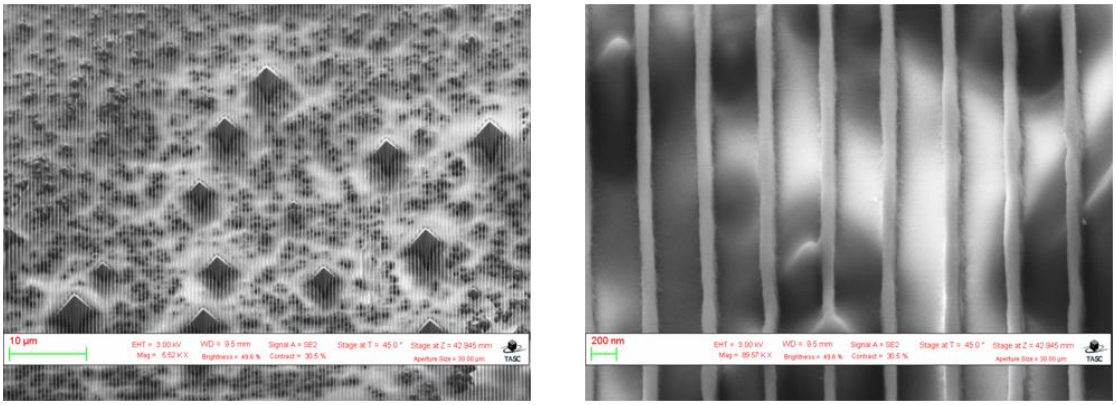

Fig. 5.16: SEM images at low (left) and high (right) magnification of resist gratings patterned by LIL on standard textured MET solar cells

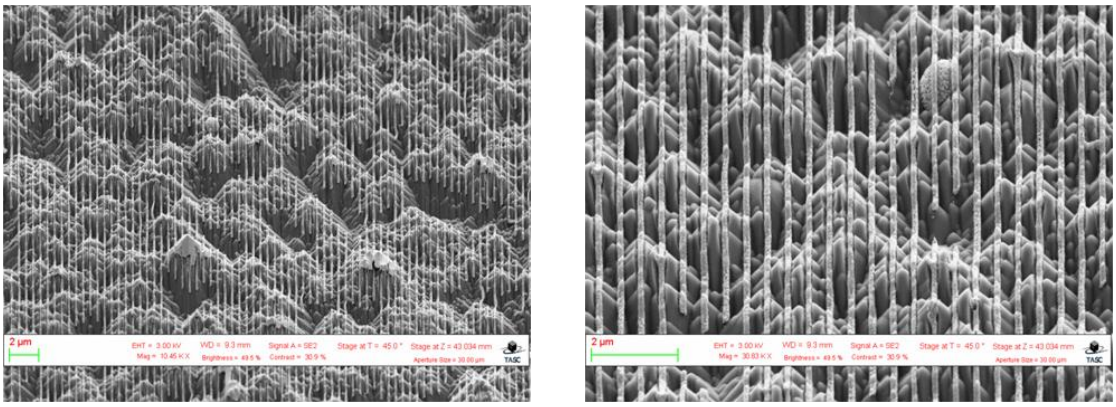

Fig. 5.17: SEM micrographs of a textured MET solar cells with a Ag plasmonic crystal.

5.4 Characterization of solar cells integrating plasmonic crystals

5.4.1 Spectroscopic ellipsometry characterization

Specular Reflectance measurements of patterned solar cell samples were performed by means of a J. A. Wollam Co. VASE Ellipsometer (Fig. 5.18, top left) in the range 400-1100nm of incident wavelength for both TM and TE polarizations. The incidence angle considered were 15°, 30° and 45° with respect to the normal. 15°, in particular, is the minimum incidence angle allowed by the instrument. Focusing probes were used to reduce the illumination spot diameter to 100µm in order to enable illumination of a portion of a patterned solar cell between two finger contacts. Measurements were compared to FEM-simulated specular reflectances. The results are reported in Fig. 5.18. The grating period, thickness and duty cycle that allowed optimal match to the experimental data are respectively 475nm, 90nm and 0.673, in good agreement with the values expected from nanofabrication: 480nm, 100nm and 0.8 respectively.

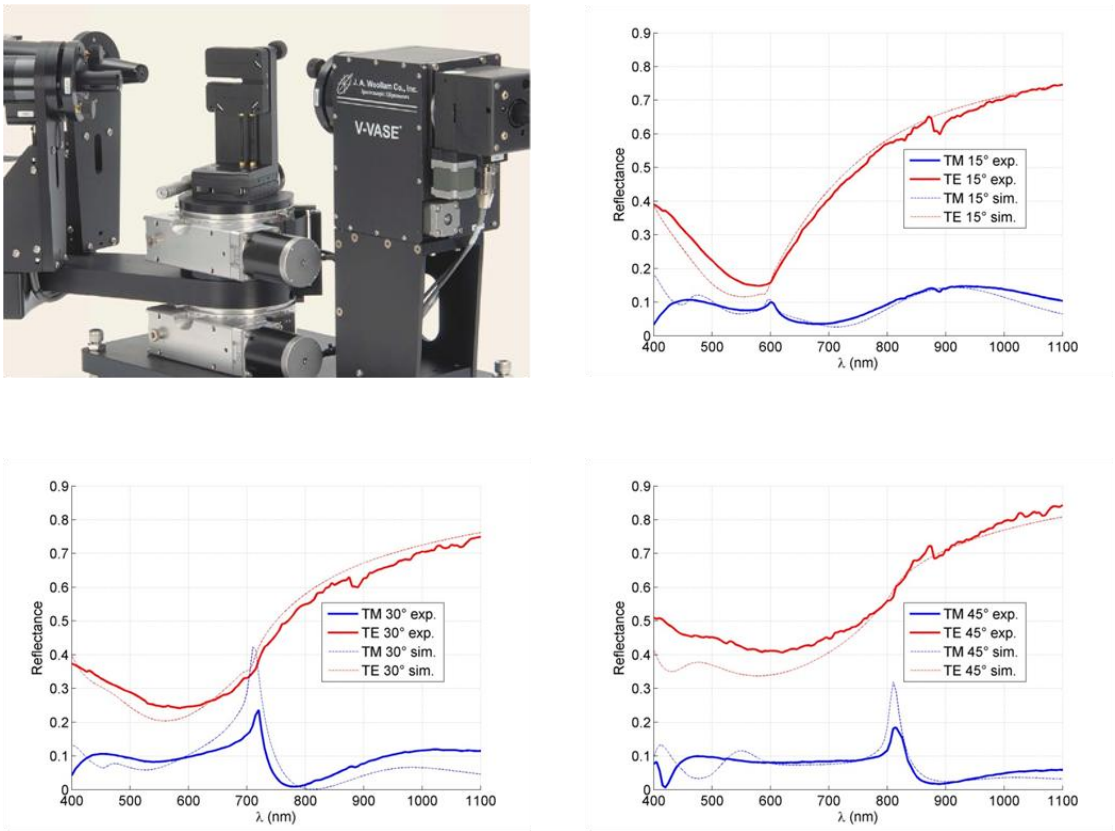

Fig. 5.18: top left: picture of J. A. Wollam Co. VASE Ellipsometer; other quadrants: measured and simulated reflection spectra for both polarizations at different incidence angles (15°, 30°, 45°)

5.4.2 Electro-optical characterization setups

Solar cells integrating plasmonic crystals on the front surface have been characterized measuring both the JV curves under a solar simulator (ABET Technologies, Sun 2000,

Fig. 5.19) and extracting the External Quantum Efficiency (EQE) spectral response in a dedicated setup.
JV characteristics have been measured both in dark condition and under an illumination that reproduces a reference AM1.5G solar spectrum. The main figures of merit have been also extracted: short circuit current density (*Jsc*), open circuit voltage (*Voc*), fill factor (*FF*) and conversion efficiency (η).
The external quantum efficiency, defined as the spectral resolved ratio between the short circuit current I_{sc} and the photocurrent I_{photo} coming from the photon flux incident on the device (see eq. 2.47), is measured by collecting the current generated by the cell at each illumination wavelength and scanning over the entire solar spectrum. This measure can be useful to understand the effect that the integration of the plasmonic grating has on the solar cell absorption characteristic. EQE spectral shape resembles and can be somehow compared to the absorptance spectra simulated, even if an electro-optical conversion factor, linked to the different penetration depth of photons at different energy, modulates the EQE behavior. The setup for the measurement of EQE is assembled in laboratory and its scheme is shown in Fig. 5.20.

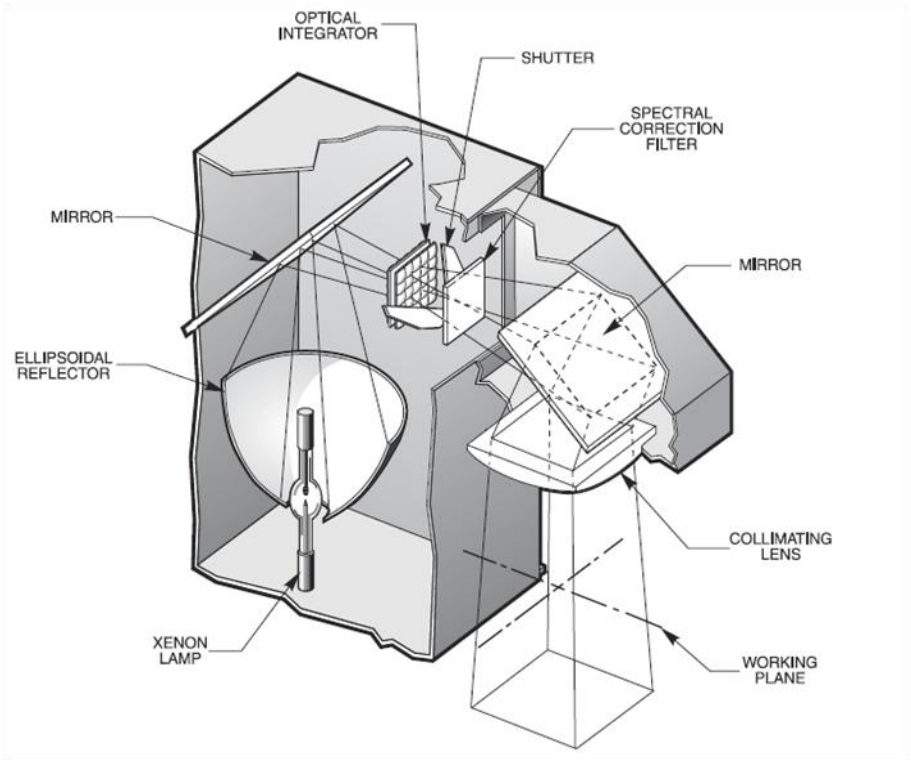

Fig. 5.19: schematic of a solar simulator useful for *JV* solar cell testing.

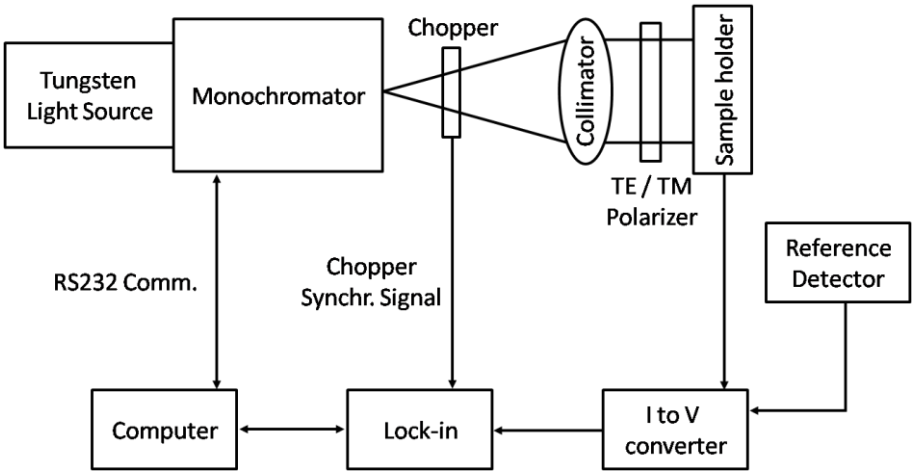

Fig. 5.20: scheme of a setup for the measurement of solar cells EQE[22].

The setup is composed by a 250W tungsten-halogen lamp coupled through an adjustable entrance slit to a Czerny-Turner monochromator with 300 mm of focal length (ACTON, SpectraPro 300i) equipped with a 1200 grooves/mm blazed grating at 500 nm. The monochromatic light is modulated in intensity with a chopper (at a frequency of ~75Hz) and is collimated with a lens. A broadband polarizing filter (Thorlabs WP25L-UB) mounted on a rotational stage is located between the lens and the device if a measure resolved in polarization is desired. First a baseline is acquired, i.e. the intensity of light incident on the device, at each wavelength and polarization, is measured and calculated from the spectral response curve of a calibrated photodiode (Newport, 818-UV, SN. 4518, NIST traceable). Then, the current produced by the cell in, virtually, short circuit condition is converted in a voltage signal through a low noise transimpedance amplifier with a gain of 10^4 V/A and input impedance lower than 1Ω. Such voltage is finally measured by a DSP lock-in amplifier (Stanford Research Systems, SR830) having as reference signal the TTL coming from the chopper controller. The spectrum corresponding to the EQE is calculated comparing the baseline and cell photocurrent. The whole system is synchronized by a software (National Instruments, LabView 7.1) in order to operate a scan along a selected wavelength interval (for this setup within 200 to 1100 nm).

5.4.3 Dark and illuminated current-voltage characteristics

We measured the *J-V* characteristics, in dark and under the sun simulator, of 6 reference flat solar cells as fabricated from our project partner MET belonging to the batch used for plasmonic crystals integration. The relative graphs are reported in Fig. 5.21 and the data are summarized in Table 7.

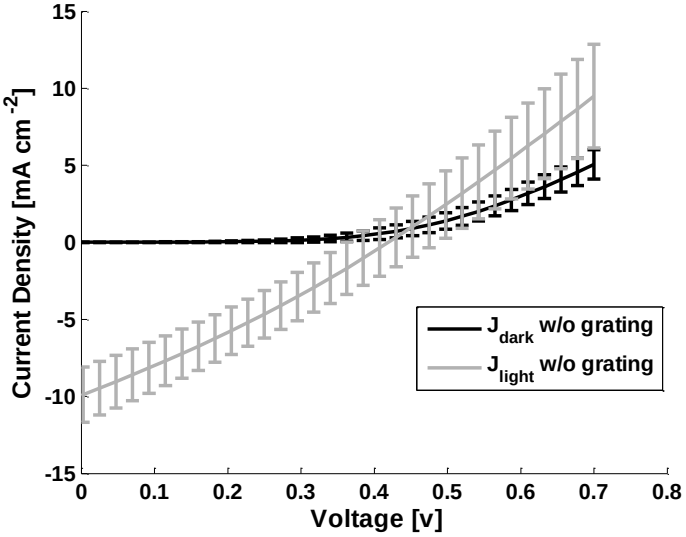

Fig. 5.21: *JV* curves in dark and under sun simulator of solar cells without plasmonic gratings

	η (%)	$\mathbf{J_{sc}}$ (mA/cm^2)	**Voc** (mV)	**FF** (%)
Average	1.15	9.51	421.54	28.66
St. dev.	0.23	1.09	51.66	0.47
max	1.47	11.09	491.86	29.32
min	0.89	7.93	335.95	27.82

Table 7: Characteristics of the batch of MET solar cells used for plasmonic crystal integration

Such cells show a low efficiency linked to the special characteristics of this test batch. The low *Jsc* can be correlated to the lack of surface texturing while the low *FF* can be explained by the high series resistance due the thin front metal grid. Such not optimal characteristics do not constitute a problem because we are interested to prove relative variations for cells with and without plasmonic gratings. For this aim, the reduced standard deviation of these measurements make possible to compare cells integrating the crystals and different reference cells of the same batch.

In order to obtain the current density, we normalized the measured current value to the area of 121mm^2 defined by the edge isolation. In this way we probably underestimate the area of the device which contributes to the photocurrent, because also carriers generated beyond this central square can diffuse toward the electrodes, and thus we probably overestimate the efficiency.

Then we measured the *JV* characteristics of 6 cells integrating the metallic periodic nanostructures, both in dark and under one sun of illumination. The grating on these cells has a thickness of 100nm, pitch of about 480nm and variable Ag linewidth, between 135nm and 200nm. Such curves are reported in Fig. 5.22 as solid lines. We also plotted, as red dashed and dotted lines in these graph, the average characteristics of

cells without grating. The relevant data extracted from *JV* characterizations of cells with plasmonic crystals are summarized in Table 8.

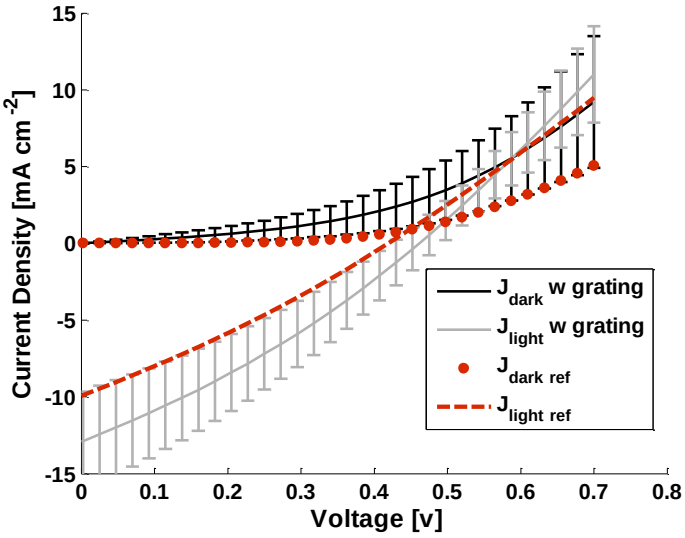

Fig. 5.22: *JV* curves in dark and under sun simulator of solar cells integrating plasmonic crystals (solid lines) and of a reference average cell without grating (red dashed and dot lines)

	η (%)	$\mathbf{J_{sc}}$ (mA/cm^2)	**Voc** (mV)	**FF** (%)
Average	1.82	13.18	457.66	29.58
St. dev.	0.53	2.63	30.75	2.47
max	2.65	18.05	502.28	33.32
min	1.26	10.49	417.33	25.03

Table 8: Characteristics of solar cells integrating plasmonic crystals

As already pointed out before, such cells have a squared active area with side of 10mm defined by photolithography within the edge isolation. Outside this central square of 100mm^2, the surface of the cell is coated with several resist layers and a top 100nm-thick silver film. So the active area is well defined because the absorption of light outside it is negligible.

As can be noted comparing the data of Table 7 and Table 8, there is a significant increase in the average efficiency value for cells integrating the plasmonic grating. This is mainly due to the increased short circuit current density, that is the enhanced photogeneration in the cells provided by the nanostructured front surface.

Also *Voc* and *FF* seem to slightly increase. So the cell series resistance is not affected by the grating fabrication. On the contrary, examining the dark *J-V* curve around the 0 bias voltage (Fig. 5.23), it seems that the shunt resistance and the dark reverse bias saturation current of the cells gets worse after the nanofabrication process.

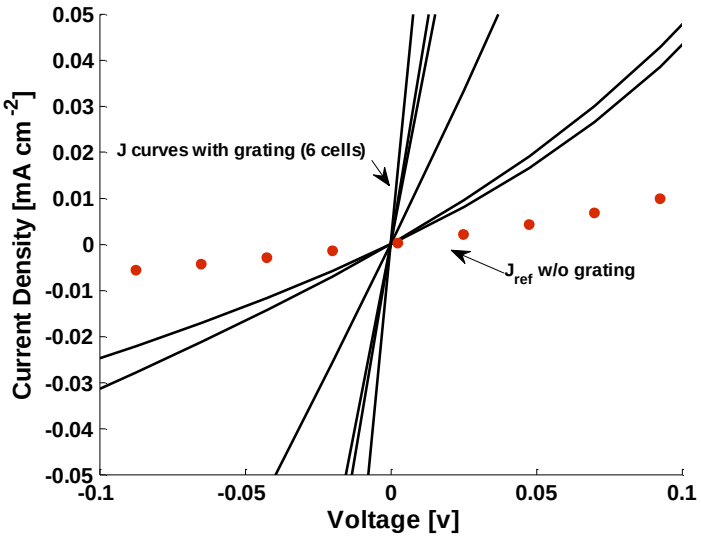

Fig. 5.23: Dark *JV* curves 6 solar cells integrating plasmonic crystals (solid lines) and of a reference cell without grating (red dotted line) around the 0 bias voltage

The electrical characteristic of the cell nanopatterned with the Ag grating over the whole front surface without active area lithographic definition has been also measured (Fig. 5.24). The normalization area used in this case was 121 mm^2, exactly like flat reference cells. The comparison of the J-V spectra in Fig. 5.24 shows that cell with grating has a greater *Jsc*. For this cell we have also measured an efficiency enhancement of 32% compared to the average of flat reference cells.

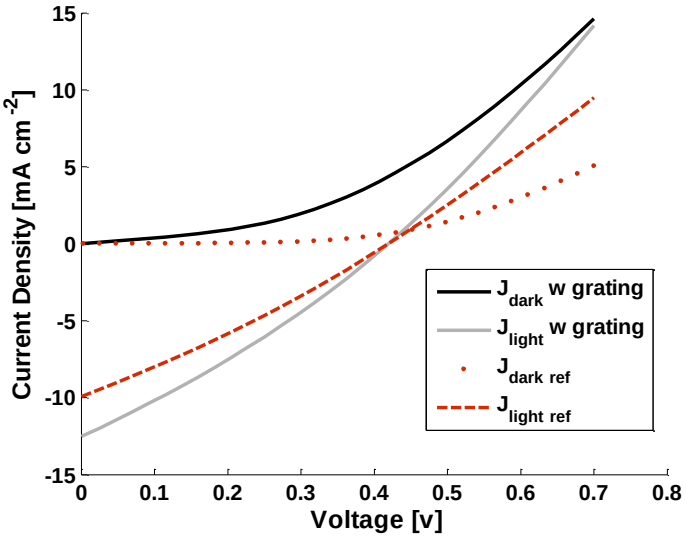

Fig. 5.24: *JV* curves, dark (black) and under sun simulator (grey) of a cell integrating the plasmonic crystal and of a flat average reference cell (red dots and red dashed)

One of the tested solar cells has been also characterized before and after the nanofabrication process. The relative illuminated J-V curves are reported in Fig. 5.25. It shows a significant *Jsc* enhancement on the same device after grating fabrication,

validating the result of Fig. 5.22 which was extracted from comparison of average characteristics of different cells of the same batch with and without plasmonic crystal.

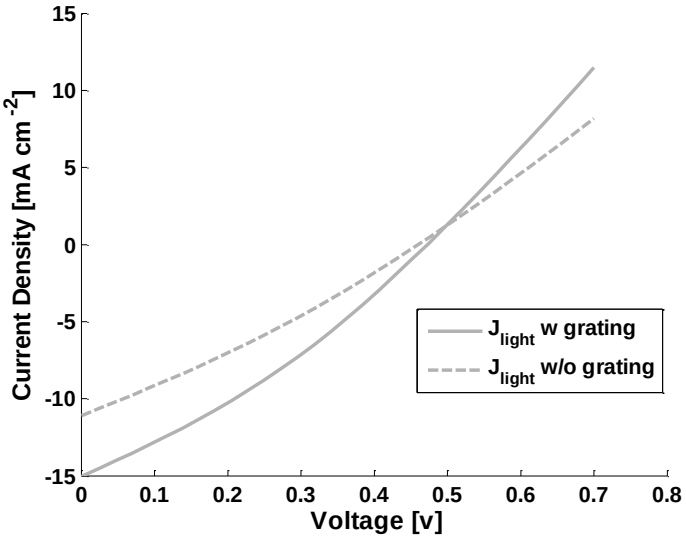

Fig. 5.25: *J-V* curves under sun simulator of one cell before plasmonic crystal integration (red dashed line) and after integration with frame outside active area (blue line)

5.4.4 External Quantum Efficiency

With the aim to understand the reason for the enhanced performance of the flat cells integrating the plasmonic crystals, EQE spectra of the same cells after J-V characterization has been measured. Again, the spectra of reference cells as fabricated from our project partner has been acquired *a priori*. The curves relative to 5 reference cells are reported in Fig. 5.26. Thus, as done for J-V characterizations, we consider reliable the comparison of spectra relative to cells with and without grating belonging to the same batch.

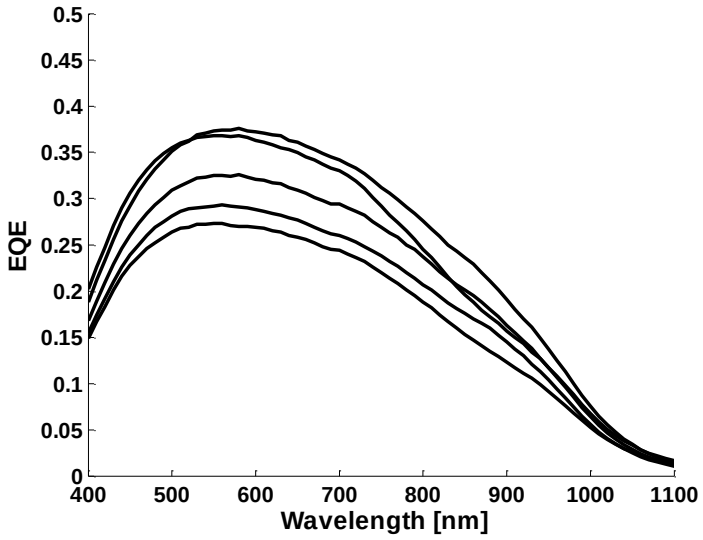

Fig. 5.26: EQE spectra of 5 reference cells without Ag grating

The spectra collected from 6 cells with grating are shown for TM and TE polarization separately in Fig. 5.27. It appears that for TM polarization there is an increase in cells responsivity for wavelengths longer than 500nm while for TE polarization the curves are below the flat reference cell spectrum over a wide bandwidth.

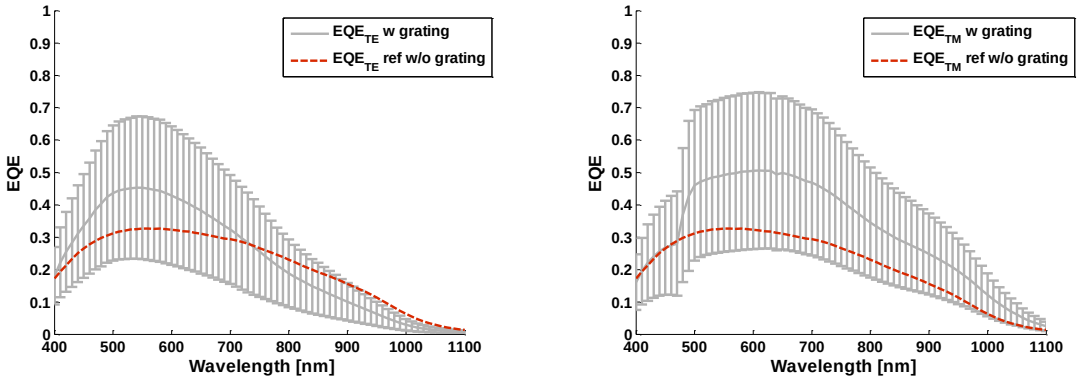

Fig. 5.27: average EQE spectrum resolved in polarization of 6 cells with plasmonic gratings compared to the reference cell. Left: TM polarization; Right: TE polarization.

The graphs of Fig. 5.27 can be correlated to the shape of the absorptance spectra simulated. Fig. 5.28 shows the calculated absorption in a device with a Ag grating with duty cycle of 70%, that best describes the linewidth obtained experimentally. For what concerns the TM polarization, the EQE spectra of cells with gratings show an improved response in the near IR, as expected from simulation. Also the dip in correspondence of $\lambda \sim 480$nm is in good agreement between measurements and simulations. On the contrary, absorptance calculation cannot predict the improved TM response in the broad band between 500 and 800nm.

Also in TE polarization, in the visible some of the cells with gratings show an enhancement in absorption that was not described by EM field simulations. Finally the reduction of light absorption in TE polarization for long wavelength is coherent with what expected.

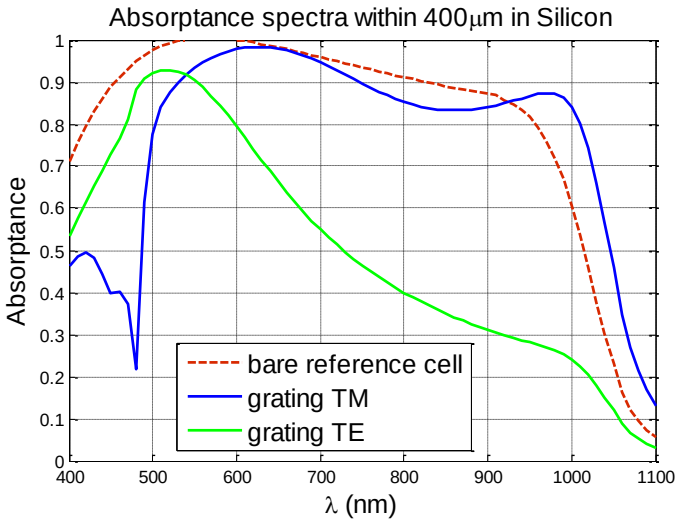

Fig. 5.28: Simulated absorptance spectrum, resolved in polarization, of a solar cell integrating on the front surface a silver digital grating with period=480nm, thickness=100nm, DC =70% (solid lines) and of a flat reference cell (red dashed line)

EQE spectra have been also acquired on a particular cell both before and after grating integration. The polarization resolved EQE spectra for this cell are reported in Fig. 5.29. The curves can be well explained by the simulated absorption spectrum of Fig. 5.28, with an increased IR response for TM polarization and a reduced response for TE polarization compared to the flat cell without grating.

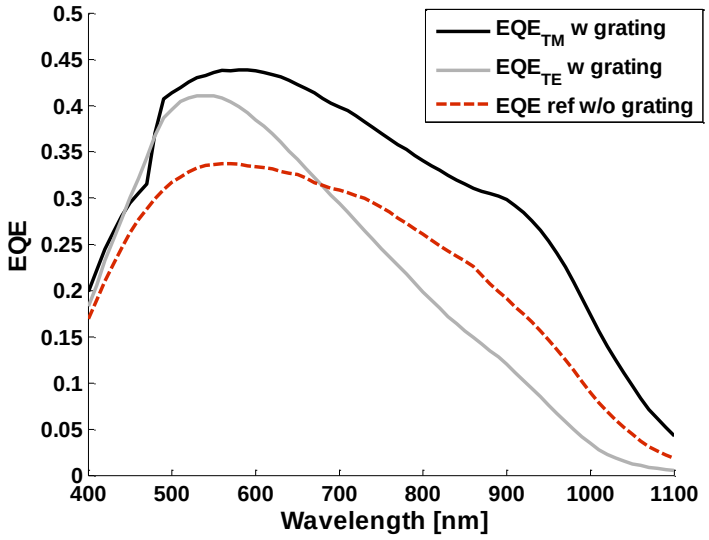

Fig. 5.29: EQE spectrum of a cell before plasmonic crystal integration (red dashed line) and polarization resolved spectra for the same cell after grating integration(TE black line, TM purple line)

This spectral behavior shows the expected TM enhancement of EQE in the IR regime, confirming the original idea that plasmonic crystals can effectively generate a light harvesting enhancement and an increase of the PV quantum efficiency.

Summarizing the results, EM field simulations were performed in order to optimize the optical response of a set of two solar cell models integrating a 1D plasmonic grating with square wave profile.

We found that the maximum absorption enhancement is found for the cell integrating the plasmonic crystal on the top of a flat Si_3N_4-coated surface. The improvement factor in case of normally impinging TM-polarized light in the 400-1100nm wavelength range is 3.6%, corresponding to a grating with 480nm period, 80% duty cycle and 100nm Ag thickness. No configuration was found to enhance the TE part of the spectrum with respect to the bare structure. Thus, we further designed and optimized a nanofabrication process suited for the realization of plasmonic gratings over photovoltaic devices based on LIL, dry etching and metal evaporation in vacuum. Patterns very similar to what indicated by optical simulation have been successfully fabricated. The nanofabrication steps are carried out on finished solar cells, so the grating integration does not require changes in the existing production flow chart. In order to achieve our purpose we have employed a Laser Interference Lithography setup able to pattern high resolution periodic nanostructures with high accuracy and high throughput over large areas. Features with size down to 100nm and different shapes have been successfully patterned over several cm^2, even on substrates characterized by high surface topography.

Current voltage characteristics, in dark and under sun simulator illumination, and polarization resolved (TE - TM) external quantum efficiency curves of reference cells and of cells after the plasmonic crystal integration have been measured.

JV characteristics under the sun simulator light show a significant improvement in conversion efficiency for cells integrating the Ag nanostructures compared to flat reference cells of the same batch. Such improvement is mainly due to the enhancement in short circuit current due to the light trapping effect provided by the plasmonic crystals. The other cell electrical features (Voc and FF) are not significantly affected by the grating nanofabrication process. The EQE spectra of cells with gratings show an enhancement in near infra-red response for TM polarization, as expected from optical simulations, and also an unexpected measured improved absorption in the visible. The latter is a further indication of effectiveness of plasmonic nanostructures in light harvesting.

Conclusions

The investigation of Surface Plasmon Polariton (SPPs), as well as other optical resonances, supported in different solar cell layouts has been investigated. Firstly, an ideal model of solar cell integrating plasmonic crystals has been developed in order to clarify the role and the potentialities that all the optical resonances involved in such structures have in remodulating light absorption. Three main optical features play a relevant role: Surface Plasmon Polariton (SPP) resonances, Cavity Mode (CM) resonances and Wood Rayleigh anomalies (WR). Coupling of these three features was found to be useful to enhance absorption in silicon within different depths, in the NIR part of the spectrum. In particular CM-WR coupling was demonstrated to produce a relevant IR-enhancement, since the grating has both antireflection properties and spreads light at grazing angles, incrementing the optical path length in silicon.

In a further analysis, a global optimization of both geometrical parameters of the grating (period, thickness, slit width) and the dielectric environment has been performed, considering different solar cell layouts, in order to obtain a gain in absorption over the widest bandwidth of solar spectrum. We found that the maximum absorption enhancement is found for the cell integrating the plasmonic crystal on the top of a flat Si_3N_4-coated surface. The improvement factor in case of normally impinging TM-polarized light in the 400-1100nm wavelength range is 3.6%, corresponding to a grating with 480nm period, 80% duty cycle and 100nm Ag thickness. No configuration was found to enhance the TE part of the spectrum with respect to the bare structure.

Following the simulation and optimization results, the design of a nanofabrication process for the integration of metal nanostructures on top of large area c-Si solar cells has been developed. The method of choice to create these highly regular large area structures is the use of Laser Interference Lithography (LIL) in combination with dry etching and metal evaporation in vacuum. A new LIL system, useful for the fabrication of large area plasmonic structures has been designed, constructed and tested. Several processes have been designed and tested and new materials have been also developed (e.g. Hybrid Organic-Inorganic solgel sinusoidal gratings). This nanofabrication setup, is working since the first months of 2010 in our laboratory at IOM-CNR in Trieste. System performances are still growing toward the control of the full set of geometric parameters of the structures that can be fabricated. Fabrication results have been tested by both morphological and optical characterizations.

Finally, solar cells have been tested by electro-optic characterizations. Polarization resolved Specular Reflectance measurements of patterned solar cell samples were performed and results validate the model. Figures of merit, JV as well as External Quantum Efficiency (EQE), of devices integrating plasmonic crystals have been also measured. *JV* characteristics show a significant improvement in conversion efficiency for cells integrating the Ag nanostructures compared to flat reference cells. Such improvement is mainly due to the enhancement in short circuit current due to the light trapping effect provided by the plasmonic crystals. The EQE spectra of cells with gratings show an enhancement in near infra-red response for TM polarization, as

expected from optical simulations, and also an unexpected measured improved absorption in the visible. The latter is a further indication of effectiveness of plasmonic nanostructures in light harvesting.

Ringraziamenti

Un particolare ringraziamento va al Prof. Romanato e a tutti i colleghi di Padova con cui ho condiviso, nel corso di questi anni, i lavori per la realizzazione del LaNN e gli sforzi per sostenerlo. Grazie a Davide per essersi letto la tesi con la “solita” impareggiabile professionalità e Valentina per le ripetizioni di Italiano... Ringrazio il Dott. Massimo Tormen e tutti i colleghi dello IOM che mi hanno nutrito di consigli preziosi e pazientemente sopportato.
Ringrazio tutti i miei maestri, tutti gli amici e i colleghi, che mi hanno sostenuto in questi anni, offrendomi continuamente idee, consigli, sorrisi e senza dubbio affetto. Ringrazio la mia famiglia che mi ha guidato e sostenuto da sempre, ricordandomi il valore positivo della conoscenza e l’importanza dell’impegno del singolo per il bene di tutti. Ringrazio Nadia, la mia colonna, esempio di tenacia, dedizione e passione per il lavoro.
I miei più sinceri ringraziamenti a tutti.

References

[1] *World Energy Outlook*. International Energy Agency, 2011.

[2] *Renewable Energy Data Book*. National Renewable Energy Laboratory, U.S. Department of Energy, 2010.

[3] *Solar Technologies Market Report*. able Energy Laboratory, U.S. Department of Energy, 2010.

[4] H. Raether, *Surface plasmons on smooth and rough surfaces and on gratings*. Springer, 1988.

[5] S. A. Maier, *Plasmonics: Fundamentals and Applications*. Springer, 2007.

[6] A. Sommerfeld, "Ueber die Fortpflanzung elektrodynamischer Wellen längs eines Drahtes," *Annalen der Physik*, vol. 303, no. 2, pp. 233-290, 1899.

[7] J. Zenneck, "Ueber die Fortpflanzung ebener elektromagnetischer Wellen längs einer ebenen Leiterfläche und ihre Beziehung zur drahtlosen Telegraphie," *Annalen der Physik*, vol. 23, no. 10, pp. 846-866, 1907.

[8] R. W. Wood, "On a Remarkable Case of Uneven Distribution of Light in a Diffraction Grating Spectrum," *Proceedings of the Physical Society of London*, vol. 18, no. 1, pp. 269-275, Jun. 1902.

[9] U. FANO, "The Theory of Anomalous Diffraction Gratings and of Quasi-Stationary Waves on Metallic Surfaces (Sommerfeld's Waves)," *Journal of the Optical Society of America*, vol. 31, no. 3, p. 213, Mar. 1941.

[10] R. Ritchie, "Plasma Losses by Fast Electrons in Thin Films," *Physical Review*, vol. 106, no. 5, pp. 874-881, Jun. 1957.

[11] R. Ritchie, E. Arakawa, J. Cowan, and R. Hamm, "Surface-Plasmon Resonance Effect in Grating Diffraction," *Physical Review Letters*, vol. 21, no. 22, pp. 1530-1533, Nov. 1968.

[12] A. Otto, "Excitation of nonradiative surface plasma waves in silver by the method of frustrated total reflection," *Physics*, vol. 216, no. 4, pp. 398-410, 1968.

[13] E. Kretschmann and H. Raether, "Radiative decay of non-radiative surface plasmons excited by light," *Zeitschrift Für Naturforschung Section A A Journal Of Physical Sciences*, vol. 23, no. 12, p. 2135, 1968.

[14] J. J. Cowan and E. T. Arakawa, "Dispersion of surface plasmons in multiple metal and dielectric layers on concave diffraction gratings," *Physica Status Solidi (a)*, vol. 1, no. 4, pp. 695-705, Apr. 1970.

[15] W. L. Barnes, A. Dereux, and T. W. Ebbesen, “Surface plasmon subwavelength optics.,” *Nature*, vol. 424, no. 6950, pp. 824-30, Aug. 2003.

[16] G. Goubau, “Surface Waves and Their Application to Transmission Lines,” *Journal of Applied Physics*, vol. 21, no. 11, p. 1119, 1950.

[17] J. Homola, “Surface plasmon resonance sensors for detection of chemical and biological species.,” *Chemical reviews*, vol. 108, no. 2, pp. 462-93, Feb. 2008.

[18] M. Born and E. Wolf, *Principles of Optics: Electromagnetic Theory of Propagation, Interference and Diffraction of Light*. Pergamon Press, 1975, p. 986.

[19] J. Homola, *Surface Plasmon Resonance Based Sensors*, vol. 4. Berlin, Heidelberg: Springer Berlin Heidelberg, 2006.

[20] H. L. Offerhaus, B. van den Bergen, M. Escalante, F. B. Segerink, J. P. Korterik, and N. F. van Hulst, “Creating focused plasmons by noncollinear phasematching on functional gratings.,” *Nano letters*, vol. 5, no. 11, pp. 2144-8, Nov. 2005.

[21] I. R. Hooper and J. R. Sambles, “Dispersion of surface plasmon polaritons on short-pitch metal gratings,” *Physical Review B*, vol. 65, no. 16, pp. 1-9, 2008.

[22] A. Luque and S. Hegedus, *Handbook of Photovoltaic Science and Engineering*. John Wiley & Sons, Ltd, 2003, p. 1162.

[23] A. E. Becquerel, “Mémoire sur les effets électriques produits sous l’influence des rayons solaires,” *Comptes Rendus des Séances Hebdomadaires*, vol. 9, pp. 561-567, 1839.

[24] R. S. Ohl, “Light-sensitive electric device including silicon,” *US Patent 2443542*, no. 2443542, 1948.

[25] S. Benzer, “Excess-Defect Germanium Contacts,” *Physical Review*, vol. 72, no. 12, pp. 1267-1268, Dec. 1947.

[26] J. I. Pantchechnikoff, “A Large Area Germanium Photocell,” *Review of Scientific Instruments*, vol. 23, no. 3, p. 135, 1952.

[27] D. M. Chapin, C. S. Fuller, and G. L. Pearson, “A New Silicon p-n Junction Photocell for Converting Solar Radiation into Electrical Power,” *Journal of Applied Physics*, vol. 25, no. 5, p. 676, 1954.

[28] D. Reynolds, G. Leies, L. Antes, and R. Marburger, “Photovoltaic Effect in Cadmium Sulfide,” *Physical Review*, vol. 96, no. 2, pp. 533-534, Oct. 1954.

[29] S. M. Sze and K. K. Ng, *Physics of Semiconductor Devices*, vol. 9, no. 5. Wiley, 2007, p. 815.

[30] G. Barbottin and A. Vapaille, *Instabilites in silicon devices –silicon passivation and related instabilities*. 1989.

[31] V. Bearzi, *Manuale di energia solare*. 2009.

[32] D. M. Caughey and R. E. Thomas, "Carrier mobilities in silicon empirically related to doping and field," *Proceedings of the IEEE*, vol. 55, no. 12, pp. 2192-2193, 1967.

[33] J. A. Schuller, E. S. Barnard, W. Cai, Y. C. Jun, J. S. White, and M. L. Brongersma, "Plasmonics for extreme light concentration and manipulation," *Nature materials*, vol. 9, no. 3, pp. 193-204, Mar. 2010.

[34] K. Tvingstedt, N.-K. Persson, O. Inganäs, A. Rahachou, and I. V. Zozoulenko, "Surface plasmon increase absorption in polymer photovoltaic cells," *Applied Physics Letters*, vol. 91, no. 11, p. 113514, 2007.

[35] H. A. Atwater and A. Polman, "Plasmonics for improved photovoltaic devices.," *Nature materials*, vol. 9, no. 3, pp. 205-13, Mar. 2010.

[36] J. Hetterich, G. Bastian, N. A. Gippius, S. G. Tikhodeev, G. von Plessen, and U. Lemmer, "Optimized Design of Plasmonic MSM Photodetector," *IEEE Journal of Quantum Electronics*, vol. 43, no. 10, pp. 855-859, Oct. 2007.

[37] S. O. Kim, H. H. Solak, M. P. Stoykovich, N. J. Ferrier, J. J. De Pablo, and P. F. Nealey, "Epitaxial self-assembly of block copolymers on lithographically defined nanopatterned substrates.," *Nature*, vol. 424, no. 6947, pp. 411-4, Jul. 2003.

[38] J. Y. Cheng, C. A. Ross, E. L. Thomas, H. I. Smith, and G. J. Vancso, "Fabrication of nanostructures with long-range order using block copolymer lithography," *Applied Physics Letters*, vol. 81, no. 19, p. 3657, 2002.

[39] H. I. Smith, "A new approach to high fidelity e-beam and ion-beam lithography based on an in situ global-fiducial grid," *Journal of Vacuum Science & Technology B: Microelectronics and Nanometer Structures*, vol. 9, no. 6, p. 2992, Nov. 1991.

[40] M. L. Schattenburg, "The critical role of metrology in nanotechnology," in *Proceedings of SPIE*, 2002, vol. 4608, pp. 116-124.

[41] J. W. Goodman, *Introduction to Fourier Optics*. McGraw-Hill, 2005, p. 491.

[42] M. E. Walsh, "On the design of interference lithography," 2004.

[43] F. L. Pedrotti and L. S. Pedrotti, *Introduction to optics*, vol. 28. Prentice Hall, 1993, p. 622.

[44] Humphrey Lloyd, "On a New Case of Interference of the Rays of Light," *The Transactions of the Royal Irish Academy*, vol. 17, pp. 171-177, 1831.

[45] P. H. Langenbeck, "Lloyd Interferometer Applied to Flatness Testing," *Applied Optics*, vol. 6, no. 10, p. 1707, Oct. 1967.

[46] A. Sonato et al., “Plasmonic Platforms for Biodetection Devices,” in *2011 International Workshop on Biophotonics*, 2011, pp. 1-3.

[47] G. Zacco et al., “Sinusoidal plasmonic crystals for bio-detection sensors,” *Microelectronic Engineering*, vol. 88, no. 8, pp. 1898-1901, Aug. 2011.

[48] W. Hinsberg, “Deep-ultraviolet interferometric lithography as a tool for assessment of chemically amplified photoresist performance,” *Journal of Vacuum Science & Technology B: Microelectronics and Nanometer Structures*, vol. 16, no. 6, p. 3689, Nov. 1998.

[49] J. Chandezon, M. T. Dupuis, G. Cornet, and D. Maystre, “Multicoated gratings: a differential formalism applicable in the entire optical region,” *Journal of the Optical Society of America*, vol. 72, no. 7, p. 839, Jul. 1982.

[50] D. Malacara, Ed., *Optical Shop Testing*. Hoboken, NJ, USA: John Wiley & Sons, Inc., 2007.

[51] R. Mahakud, O. Prakash, S. K. Dixit, and J. K. Mittal, “Analysis on the laser beam pointing instability induced fringe shift and contrast dilution from different interferometers used for writing fiber Bragg grating,” *Optics Communications*, vol. 282, no. 11, pp. 2204-2211, Jun. 2009.

[52] G. Della Giustina, G. Zacco, E. Zanchetta, M. Gugliemi, F. Romanato, and G. Brusatin, “Interferential lithography of Bragg gratings on hybrid organic–inorganic sol–gel materials,” *Microelectronic Engineering*, vol. 88, no. 8, pp. 1923-1926, Aug. 2011.

[53] P. Falcaro et al., “Fabrication of Advanced Functional Devices Combining Soft Chemistry with X-ray Lithography in One Step,” *Advanced Materials*, vol. 21, no. 48, pp. 4932-4936, Dec. 2009.

[54] G. Della Giustina, G. Brusatin, M. Guglielmi, C. Palazzesi, E. Orsini, and P. Prosposito, “Doubly patternable epoxy based sol–gel structures by UV and soft lithography,” *Solid State Sciences*, vol. 12, no. 11, pp. 1890-1893, Nov. 2010.

[55] G. Brusatin, G. D. Giustina, F. Romanato, and M. Guglielmi, “Design of hybrid sol-gel films for direct x-ray and electron beam nanopatterning.,” *Nanotechnology*, vol. 19, no. 17, p. 175306, Apr. 2008.

[56] S. H. Zaidi, “Multiple-exposure interferometric lithography,” *Journal of Vacuum Science & Technology B: Microelectronics and Nanometer Structures*, vol. 11, no. 3, p. 658, May 1993.

[57] M. Niggemann, M. Riede, A. Gombert, and K. Leo, “Light trapping in organic solar cells,” *physica status solidi (a)*, vol. 205, no. 12, pp. 2862-2874, Dec. 2008.

[58] C. Ye, K. Y. Wong, Y. He, and X. Wang, “Distributed feedback sol-gel zirconia waveguide lasers based on surface relief gratings,” *Optics Express*, vol. 15, no. 3, p. 936, 2007.

[59] M. Miyake, Y.-C. Chen, P. V. Braun, and P. Wiltzius, “Fabrication of Three-Dimensional Photonic Crystals Using Multibeam Interference Lithography and Electrodeposition,” *Advanced Materials*, vol. 21, no. 29, pp. 3012-3015, Aug. 2009.

[60] F. del Monte, O. Martínez, J. A. Rodrigo, M. L. Calvo, and P. Cheben, “A Volume Holographic Sol-Gel Material with Large Enhancement of Dynamic Range by Incorporation of High Refractive Index Species,” *Advanced Materials*, vol. 18, no. 15, pp. 2014-2017, Aug. 2006.

[61] F. Romanato, K. H. Lee, H. K. Kang, G. Ruffato, and C. C. Wong, “Sensitivity enhancement in grating coupled surface plasmon resonance by azimuthal control,” *Optics Express*, vol. 17, no. 14, p. 12145, Jul. 2009.

[62] W. Yu and X. Yuan, “Variable surface profile gratings in sol-gel glass fabricated by holographic interference,” *Optics Express*, vol. 11, no. 16, p. 1925, Aug. 2003.

[63] A. F. Lasagni, D. Yuan, and S. Das, “Layer-by-Layer Interference Lithography of Three-dimensional Microstructures in SU-8,” *Advanced Engineering Materials*, vol. 11, no. 5, pp. 408-411, May 2009.

[64] W. Que, “Preparation and optical properties of patternable TiO2/ormosils hybrid films for photonics applications,” *Chemical Physics Letters*, vol. 369, no. 3-4, pp. 354-360, Feb. 2003.

[65] D. J. Kang, J.-K. Kim, and B.-S. Bae, “Simple fabrication of diffraction gratings by two-beam interference method in highly photosensitive hybrid sol-gel films,” *Optics Express*, vol. 12, no. 17, p. 3947, 2004.

[66] M. GUGLIELMI, G. BRUSATIN, and G. DELLAGIUSTINA, “Hybrid glass-like films through sol–gel techniques,” *Journal of Non-Crystalline Solids*, vol. 353, no. 18-21, pp. 1681-1687, Jun. 2007.

[67] J. S. White et al., “Extraordinary optical absorption through subwavelength slits,” *Optics Letters*, vol. 34, no. 5, p. 686, Feb. 2009.

[68] K. R. Catchpole and A. Polman, “Plasmonic solar cells,” *Optics Express*, vol. 16, no. 26, p. 21793, Dec. 2008.

[69] K. R. Catchpole, “Nanostructures in photovoltaics.,” *Philosophical transactions. Series A, Mathematical, physical, and engineering sciences*, vol. 364, no. 1849, pp. 3493-503, Dec. 2006.

[70] S. Pillai, K. R. Catchpole, T. Trupke, and M. A. Green, “Surface plasmon enhanced silicon solar cells,” *Journal of Applied Physics*, vol. 101, no. 9, p. 093105, 2007.

[71] D. Derkacs, S. H. Lim, P. Matheu, W. Mar, and E. T. Yu, “Improved performance of amorphous silicon solar cells via scattering from surface plasmon

polaritons in nearby metallic nanoparticles," *Applied Physics Letters*, vol. 89, no. 9, p. 093103, 2006.

[72] N. C. Panoiu and R. M. Osgood, Jr., "Enhanced optical absorption for photovoltaics via excitation of waveguide and plasmon-polariton modes," *Optics Letters*, vol. 32, no. 19, p. 2825, 2007.

[73] R. A. Pala, J. White, E. Barnard, J. Liu, and M. L. Brongersma, "Design of Plasmonic Thin-Film Solar Cells with Broadband Absorption Enhancements," *Advanced Materials*, vol. 21, no. 34, pp. 3504-3509, Sep. 2009.

[74] P. Zilio, D. Sammito, G. Zacco, and F. Romanato, "Absorption profile modulation by means of 1D digital plasmonic gratings.," *Optics Express*, vol. 18, no. 19, pp. 19558-19565, 2010.

[75] E. D. Palik, *Handbook of Optical Constants of Solids*, vol. 1, no. 1. Academic Press, 1985, p. 3227.

[76] L. D. Landau, L. P. Pitaevskii, and E. M. Lifshitz, *Electrodynamics of Continuous Media*, vol. 8, no. 14. Pergamon Press, 1984, p. 460.

[77] B. Sturman, E. Podivilov, and M. Gorkunov, "Theory of extraordinary light transmission through arrays of subwavelength slits," *Physical Review B*, vol. 77, no. 7, Feb. 2008.

[78] J. Porto, F. García-Vidal, and J. Pendry, "Transmission Resonances on Metallic Gratings with Very Narrow Slits," *Physical Review Letters*, vol. 83, no. 14, pp. 2845-2848, Oct. 1999.

[79] F. García-Vidal and L. Martín-Moreno, "Transmission and focusing of light in one-dimensional periodically nanostructured metals," *Physical Review B*, vol. 66, no. 15, pp. 1-10, 2002.

[80] D. Crouse, "Numerical Modeling and Electromagnetic Resonant Modes in Complex Grating Structures and Optoelectronic Device Applications," *IEEE Transactions on Electron Devices*, vol. 52, no. 11, pp. 2365-2373, 2005.

[81] R. Gordon, "Light in a subwavelength slit in a metal: Propagation and reflection," *Physical Review B*, vol. 73, no. 15, pp. 8-10, 2006.

[82] F. Medina, F. Mesa, and D. C. Skigin, "Extraordinary Transmission Through Arrays of Slits: A Circuit Theory Model," *IEEE Transactions on Microwave Theory And Techniques*, vol. 58, no. 1, pp. 105-115, 2010.

[83] Q. Cao and P. Lalanne, "Negative role of surface plasmons in the transmission of metallic gratings with very narrow slits.," *Physical Review Letters*, vol. 88, no. 5, p. 057403, 2002.

[84] H. Liu and P. Lalanne, "Microscopic theory of the extraordinary optical transmission.," *Nature*, vol. 452, no. 7188, pp. 728-731, 2008.

[85] T. W. Ebbesen, H. J. Lezec, H. F. Ghaemi, T. Thio, and P. A. Wolff, "Extraordinary optical transmission through sub-wavelength hole arrays," *Nature*, vol. 391, no. 6668, pp. 667-669, 1998.

[86] J. Weiner, "The physics of light transmission through subwavelength apertures and aperture arrays," *Reports on Progress in Physics*, vol. 72, no. 6, p. 064401, 2009.

[87] L. Rayleigh, "On the Dynamical Theory of Gratings," *Proceedings of the Royal Society A Mathematical Physical and Engineering Sciences*, vol. 79, no. 532, pp. 399-416, 1907.

[88] Y. Xie, A. R. Zakharian, J. V. Moloney, and M. Mansuripur, "Transmission of light through periodic arrays of sub-wavelength slits in metallic hosts.," *Optics Express*, vol. 14, no. 14, pp. 6400-6413, 2006.

[89] Y. Takakura, "Optical Resonance in a Narrow Slit in a Thick Metallic Screen," *Physical Review Letters*, vol. 86, no. 24, pp. 5601-5603, 2001.

[90] F. Marquier, J. Greffet, S. Collin, F. Pardo, and J. Pelouard, "Resonant transmission through a metallic film due to coupled modes.," *Optics Express*, vol. 13, no. 1, pp. 70-76, 2005.

[91] H. C. Guo et al., "Large-area metallic photonic crystal fabrication with interference lithography and dry etching," *Applied Physics B*, vol. 81, no. 2-3, pp. 271-275, 2005.

[92] A. Fernandez, J. Decker, S. Herman, D. Phillion, D. Sweeney, and M. Perry, "Methods for fabricating arrays of holes using interference lithography," *Journal of Vacuum Science and Technology B: Microelectronics and Nanometer Structures*, vol. 15, no. 6, p. 2439, 1997.